UNIVERSIDAD NACIONAL AUTÓNOMA
DE MÉXICO

POSGRADO EN CIENCIAS FÍSICAS

Jets structure in Pb–Pb collisions at LHC energies

TESIS

QUE PARA OBTENER EL GRADO DE:

DOCTORA EN CIENCIAS (FÍSICA)

PRESENTA:

ISABEL DOMÍNGUEZ JIMÉNEZ

DIRECTORES DE TESIS:

Dr. Guy Paić

Dr. Eleazar Cuautle Flores

MIEMBRO DE COMITÉ TUTORAL:

Dr. Jesús Guillermo Contreras Nuño

MÉXICO, D.F. 2011

Resumen

El objetivo de este trabajo es estudiar las propiedades de la materia densa utilizando jets en el ambiente de simulación y análisis del experimento ALICE del CERN. Específicamente, nos hemos enfocado a las modificaciones que pueden sufrir los jets en un medio de materia nuclear densa. Con dicho propósito, se simularon eventos de alto p_T en colisiones $p+p$ con PYTHIA , para tomarlos como referencia y eventos simulados utilizando dos modelos de pérdida de energía partónica: PYQUEN y Q-PYTHIA. Después de simular los eventos, se utilizo un algoritmo de cono, implementado en el ambiente de simulación del experimento ALIROOT, para la reconstrucción de los jets. Se estudiaron las modificaciones en la estructura de los jets debido a la pérdida de energía partónica, a través del momento transverso intrínseco k_T y el momento transverso con respecto al eje del jet j_T. También se llevo a cabo un análisis de las variables de forma del evento, seleccionando diferentes topologías y observando las modificaciones en tres de ellas: τ, R y T_{min}. Con este estudio se espera poder entender mejor las propiedades de la materia densa creada en colisiones de $Pb+Pb$ a energías de LHC.

Abstract

The aim of this work is to study the properties of the dense matter via jets in the framework of the ALICE experiment in CERN. Specifically we have concentrated on the aspect of modifications in jet structure in a dense nuclear medium environment. With this purpose, we simulated high-p_T events in $p+p$ collision, with PYTHIA, as a baseline, and subsequently these events were passed through two afterburner models of energy loss: PYQUEN and Q-PYTHIA, to simulate the effect of a dense medium. After events simulation, jets were reconstructed in the framework of the ALICE experiment (ALIROOT) with a jet finding algorithm. Modifications in jet structure due to parton energy loss, like: the intrinsic transverse momentum k_T and the transverse momentum with respect to the jet axis j_T were studied, as well as event shape analysis, identifying different topologies of the events and the modifications in three shape variables: τ, R and T_{min}. This study helps us to understand the properties of a dense medium created in $Pb+Pb$ collisions at LHC energies.

Introducción

En los pasados 100 años la idea de los constituyentes fundamentales de la materia ha evolucionado considerablemente. Se encontró que los átomos estaban constituidos por electrones y núcleos y que estos últimos están formados por protones y neutrones, a los que en general se les llama nucleones. A su vez, estos nucleones se encuentran formados por partículas más pequeñas llamadas quarks y gluones.

Los quarks y antiquarks nunca han sido observados como partículas libres, siempre se encuentran, ya sea, en grupos de tres llamados *bariones* (protones, neutrones, etc...) o de dos llamados *mesones* (piones, kaones, etc.). Sin embargo, se cree que los quarks libres existieron en el universo temprano hasta 40 microsegundos después del Big Bang. De acuerdo a esta teoría, el universo estaba formado por un gas caliente llamado ***Plasma de quarks y gluones*** (QGP). La temperatura de este plasma era aproximadamente 100 000 veces mayor que la temperatura del sol (unos 100 x 10^{10} K); no se sabe si los quarks son verdaderamente elementales, pero si lo son, el plasma en el universo temprano se debió de haber formado directamente del Big Bang y conforme el universo se enfrió los quarks y antiquarks se agruparon en *hadrones* (mesones y bariones). Al hecho de que los quarks siempre han sido observados en estados ligados se le llama *confinamiento*.

La teoría que estudia las interacciones entre los quarks y gluones es la Cromodinámica Cuántica (QCD) y ésta predice una transición de la materia hadrónica al plasma de quarks y gluones libres. La predicción de esta transición de fase ha dado origen a su búsqueda experimental y desde hace casi 20 años se intenta encontrar y estudiar sus propiedades en el laboratorio.

Para producir este nuevo estado de la materia se requiere un sistema denso y a alta temperatura de quarks y gluones y para formarlo, se hacen chocar haces de iones pesados que viajan con una velocidad cercana a la de la luz. El sistema creado en estas colisiones pasa por varias etapas y finalmente se emiten partículas que inciden en los detectores, con ellas se tienen que definir los observables que den indicio de la eventual creación del plasma, es decir, encontrar señales del desconfinamiento. Una de las señales que se ha estudiado es la pérdida de energía que sufren los quarks y gluones al viajar a través del plasma.

Se predice que la pérdida de energía depende de la velocidad con la que las partículas cargadas se muevan dentro del plasma. El efecto es mayor para aquellos quarks y gluones que viajan más rápido. Por otra parte hay muchos indicios, conocidos colectivamente como dualidad partón-hadrón, de que los hadrones con mucho momento provienen de partones que también llevaban mucho momento. Así, que la pérdida de energía, se reflejaría en una disminución, o incluso en la desaparición, de las partículas con momento grande.

La detección experimental de este fenómeno sufre de varias complicaciones. Por un lado, el espectro de momentos cae exponencialmente, por lo que en una colisión dada hay muchísimas más partículas con momentos pequeños que grandes. Por otro lado, la producción de partículas es un proceso cuántico por lo que esta sujeto a fluctuaciones. Además un efecto similar en los espectros de partículas medidas en los detectores podría haber sido causado por otros medios y no solamente por la pérdida de energía que sufren los quarks y gluones al viajar a través del plasma. Así, debido a la gran complejidad del problema no hay una señal que por si misma determine la existencia de la formación de QGP, sino que es la consistencia de muchas señales en diversos tipos de experimentos de las que se deducirá su existencia.

A la fecha se han medido espectros de partículas cargadas producidas en colisiones de iones pesados en experimentos localizados en los aceleradores SPS (Super Proton Synchroton) del CERN (European Organisation for Nuclear Research) y en RHIC (Relativistic Hevy Ion Collider) del BNL (Brookhaven National Laborator). RHIC ha observado una supresión de partículas con mucho momento transversal con respecto a $p+p$. En el LHC (Large Hadron Collider) se espera que la energía de las colisiones sea lo suficientemente grande como para alcanzar el desconfinamiento de los quarks y gluones, formando un plasma de éstos.

En colisiones de iones pesados las observables son comparadas con las observables de colisiones $p+p$, así, la idea de este trabajo es utilizar simulación `Monte-Carlo` de colisiones $p+p$ y $Pb+Pb$ y la reconstrucción de jets en estos eventos, para estudiar señales de desconfinamiento, considerando energías de ALICE [1, 2], uno de los cuatro detectores con los que cuenta el LHC.

Jets con momento transverso grande

Jet se refiere a un grupo de hadrones que se originaron de la fragmentación de colisiones duras de partones. Las partículas del jet están contenidas en un cono de radio $R = \sqrt{(\Delta\eta)^2 + (\Delta\phi)^2}$ y la energía y dirección del jet se esperan sean cercanas a las del partón inicial. Dicho jet moviéndose en un plasma de quark y gluones (esto es, en un medio con alta densidad de carga), pierde energía al interactuar con el medio, esto es, radia partones quienes se llevan parte de la energía original del jet.

En 1982 Bjorken [3] sugirió que los partones que viajan rápido a través del plasma de quarks y gluones pudieran perder grandes cantidades de energía por choques elásticos con los componentes del plasma, dando por resultado la supresión de jets en el medio altamente denso que se forma en los choques de iones pesados. En una serie de artículos teóricos de los años 90 Gyulassy, Plümer y X.N. Wang [4] identificaron la supresión de jets como consecuencia de la pérdida de radiación, y en 1995-1997 Baier , Dokshitzer, Mueller, Peigné y Schiff [5] realizaron un estudio importante sobre la taza de la pérdida de energía como resultado de múltiples interacciones de color del gluón radiado con los componentes coloreados en el plasma. En el límite de un plasma ópticamente grueso, encontraron que la pérdida de energía ΔE de los partones rápidos, aumenta cuadráticamente con la distancia L que recorren antes de escaparse y hadronizarse.

$$\Delta E \approx \frac{\alpha_s}{2}\frac{\mu^2}{\lambda}L^2, \tag{1}$$

donde α_s es la constante de acoplamiento, μ es el apantallamiento de Debye de las cargas de color en el plasma y λ el recorrido libre medio del gluón.

Las predicciones para esta pérdida de energía fueron mejoradas por Gyulassy, Levai, Vitev [6] y Wiedemann [7] considerando opacidad finita . Esto conduce a una dependencia importante de la pérdida de energía ΔE del partón rápido y a las desviaciones de la dependencia cuadrática de la longitud de la trayectoria, para valores pequeños de L. Con estos resultados mejorados se puede mantener la esperanza que la pérdida de energía se pueda utilizar como punta de prueba cuantitativa de la densidad y de la evolución temporal del plasmas de quarks y gluones creado en colisiones del iones pesados.

Evidencia experimental

Existen 4 experimentos en RHIC (Relativistiv Heavy Ion Collisions) que han estudiado colisiones $p+p$ y $Au+Au$ a energías del centro de masa de $\sqrt{s_{\mathrm{NN}}} = 62.4$, 130 y 200 GeV los cuales han mostrado evidencias de la pérdida de energía. Se ha encontrado que las partículas con mucho momento trasversal, p_T, son altamente suprimidas en colisiones centrales de $Au+Au$, además la no supresión de estas partículas en colisiones $d+Au$ confirma que la supresión se puede atribuir a la interacción de los partones con el medio denso formado durante la colisión. Esta supresión de partículas se ha estudiado mediante las correlaciones azimutales.

Las correlaciones azimutales entre hadrones se escriben usualmente como:

$$C(\Delta\Phi) = \frac{1}{N_{trigger}} \int d\Delta\eta \frac{dN}{d\Delta\Phi d\Delta\eta} \quad (2)$$

donde $\Delta\Phi$ y $\Delta\eta$ son, respectivamente, el ángulo azimutal y la pseudorapidez entre la partícula con más alto momento y su partícula asociada. La correlación azimutal muestra una estructura de dos picos que es interpretada por STAR [8] como evidencia de jets a nivel partónico. En el caso de colisiones de $Au+Au$ se observa una disminución importante de estos picos en $\Delta\phi = \pm\pi$, lo que es interpretado como una pérdida de energía de los partones al atravesar un medio denso.

Jets en ALICE

El experimento LHC, inicialmente realizó corridas de choques de $p+p$ a $\sqrt{s_{\mathrm{NN}}} = 900$ GeV y 7 TeV. Las colisiones de $Pb+Pb$ se realizaron a una energía de $\sqrt{s_{\mathrm{NN}}} = 2.7$ TeV y posteriormente se realizarán con una energía de $\sqrt{s_{\mathrm{NN}}} = 5.5$ TeV. En este experimento se espera que la energía de la colisión sea lo suficientemente grande para que se lleve a cabo el desconfinamiento de los quarks y gluones, formándose un plasma de estos componentes fundamentales de la materia. El detector ALICE se enfoca en el estudio de las propiedades de este plasma.

Producción mediante técnica Monte Carlo

Anticipándose a la toma de datos, se realizan estudios sobre la física que se espera poder estudiar en ALICE mediante simulación `Monte-Carlo`. La estrategia general para la simulación `Monte-Carlo` de colisiones $Pb+Pb$ consiste en generar procesos duros en colisiones $p+p$ utilizando el generador de eventos PYTHIA 6.2.14 [9], que sería una muestra de jets, esto es, una verdadera señal y mezclarlos con eventos generados en colisiones $Pb+Pb$ utilizando el generados de HIJING v1.36 [10], que sería ruido.

Los generadores de colisiones $p+p$ han sido adaptados para simular modificaciones nucleares en los estados iniciales y finales. Las modificaciones al estado inicial han sido incluidos en las funciones de densidad de los partones dentro del núcleo (PDF's). Las modificaciones en los estados finales de los jets con momento transverso grande producidos en colisiones de iones pesados a energías de LHC, se espera que sean dominadas por la perdida de energía a través de la radiación de gluones, debido a la presencia de un medio denso.

No existe hasta la fecha un solo generador para simular este efecto, sin embargo varias aproximaciones fenomenológicas pueden ayudar a estudiar y entender la pérdida de energía. PYQUEN [11] y Q-PYTHIA [12] como parte del ambiente de simulación del detector ALICE, ALIROOT [13], han sido utilizados para la simulación

y estudio de dichas modificaciones en los estados finales.

Una vez que la simulación de la colisión ha sido realizada incluyendo las modificaciones debido a las presencia de un medio denso, se requiere tener control sobre la producción de eventos en los cuales los jets sean bien identificados. Con este propósito se utiliza un análisis de la forma del evento (Event Shape Analysis ESA) [14, 15] y un algoritmo de cono para la reconstrucción de jets [16].

Así, el trabajo se divide en 3 etapas:

1. Simulación de eventos a energías de LHC incluyendo los modelos de pérdida de energía en el ambiente de simulación de ALICE.
2. Clasificación y reconstrucción de eventos, en base a su topología, utilizando ESA y un algoritmo de cono
3. Estudio las modificaciones en la estructura de los jets debido a la pérdida de energía partónica, a través del momento transverso intrínseco k_T y el momento transverso con respecto al eje del jet j_T, así como también los efectos de un medio nuclear en términos de los factores de supresión R_{AA} en función de p_T y j_T y las variables de forma τ, R y T_{min}

Todo en un ambiente bajo las condiciones del experimento ALICE.

Contents

List of Figures

List of Tables

Chapter 1

Introduction

In the past 100 years the idea of the fundamental constituents of the matter has evolved considerably. It was found that atoms split into electrons and nucleus and that these last are formed by protons and neutrons, which in generally they are called nucleons. These nucleons are formed by small particles called quarks and gluons.

Quarks and antiquarks have never been observed as free particles, they are either in colorless groups of three so-called *baryons* (protons, neutrons, etc.) or two-called *mesons* (pions, kaons, etc.). However, it is believed that free quarks existed in the early universe up to 40 microseconds after of the Big Bang. Following this theory, the universe consisted of a hot gas called ***Quark and gluon plasma*** (QGP). The temperature of this plasma was approximately 100 000 higher than the temperature of the sun (approximately 100 x 10^{10} K), it is not known if the quarks are truly elementary, but if they are, the plasma in the early universe had been formed directly from the Big Bang and as the universe cooled quarks and antiquarks were coalesscing into *hadrons* (baryons and mesons). The fact that quarks has never been observed is called *confinement*.

The theory that studies the interactions between quarks and gluons is quantum chromodynamic and it predicts a transition from color non-conductive to a color conductive hadronic matter plasma of quarks and gluons. The prediction of this phase transition has given rise to its search for 20 years and study of their properties in the laboratory. To produce this new state of matter is required a dense system of high temperature that is reached colliding beams of heavy ions traveling at a speed close to that of the light. The system created in these collisions passes through several stages and finally, emitted particles are detected. In them, we try to find signals of deconfinement. One of the signals that have been studied is the energy loss suffered by quarks and gluons while traveling through the plasma.

It is predicted that the loss of energy depends on the speed with which the charged

particle moves inside the plasma. The effect is bigger for quarks and gluons who travel faster. On the other hand there many indications, known collectively as duality parton-hadron, hadrons with a high momentum come from partons with much momentum too. So, the energy loss reflected in a decrease, or even the disappearance of the particles with large momenta.

Experimental detection of this phenomenon suffers from several complications. The spectrum of momenta falls exponentially with the momentum, so in a collision there are many more particles with small momentum than with larger ones. Furthermore the production of particles is a quantum process so which is subject to fluctuations. Besides, a similar effect on the spectra of particles measured in the detectors could have been caused by other means. So, because of the great complexity of the problem there is not only one signal that by itself determines the formation of QGP, but it is the union of many signals at different experiments that could give evidence of it existence.

Spectra of charged particles produced in heavy ion collision experiments located in the accelerators SPS (Super Proton Synchroton) of CERN (European Organization for Nuclear Research) and RHIC (Relativistic Heavy Ion Collider) of BNL (Brookhaven National Laboratory), has been measured. RHIC has observed a suppression of particles with a lot of transverse momentum with respect to proton - proton. In the experiment LHC at CERN it is expected that the energy of the collision will be sufficient to deconfine quarks and gluons, forming a plasma of these fundamental components of the matter.

In heavy ion collision the observables are compared with the observables measured in $p+p$ collisions, so the idea of this work is to use the `Monte-Carlo` simulation of $p+p$ collisions and reconstruction of jets in these events, to study the signs of desconfinement related to the parton's intrinsic momentum k_T, the transverse momentum with respect to the jet axis j_T and three event shape variables, τ, R and T_{min}, to follow the same analysis in $Pb+Pb$ and compare the two cases. This work was developed considering the energies of the LHC and the environment of the ALICE detector at the LHC.

The first part of this work is a revision of the current status of the search of the QGP. In this chapter is explain how to create such plasma in the laboratory, as well as, signals that are being proposed as a possible indication of formation. Subsequently are some of the experimental results obtained.

In the second section we worked on simulation and reconstruction of jets and their modifications due to parton energy loss. Finally we explore the possibility that j_T, k_T and three event shape variables, τ, R and T_{min}, are used as observable to study the dense system.

Chapter 2

QCD phase diagram and QGP

In quantum chromodynamics (QCD) [17], theory of the strong force, the interactions of hadrons are described in terms of the interaction among the hadronics constituents *quarks and gluons* (referred as partons). One of the key features of the theory that has set it, is the property of asymptotic freedom. This term is used to describe the weakening of effective quark-gluon coupling at short distance.

Based on asymptotic freedom, Collins and Perry [18] suggested that a high temperature or density, matter should be close to ideal gas arguing that in dense matter constituents are almost always close to each other, and therefore, due to the asymptotic freedom, their interaction should be sufficiently weak. This ideal gas was called quark-gluon plasma (QGP).

The QCD phase diagram, at baryonic density equal to zero, is based on lattice QCD [19], but for nonzero baryon density it is necessary to interpolate between low-density hadronic matter, described by low-energy effective theories and high-density quark-gluon plasma described by perturbative QCD. The result of lattice is shown in figure 2.1. Near T_c the energy density in units of T^4 changes dramatically by more than a factor of 10 within a very narrow temperature interval. The critical density of energy ε_c is of the order of 1 GeV/fm^3 and can be reached heating the matter with baryonic density zero to temperature of $T_c \sim 170$ MeV or compress the nuclear cold matter to the baryonic density of $\rho_c \sim$ 3 -10 ρ_0 (where ρ_0 = 0.15 fm^{-3} is the density of nuclear matter in equilibrium at zero temperature) or by combination of both.

2.1. QGP: Theoretical overview

The deconfinement can be explained in terms similar to the shielding of the electric force loads. In vacuum, two electric charges interact through the Coulomb potential,

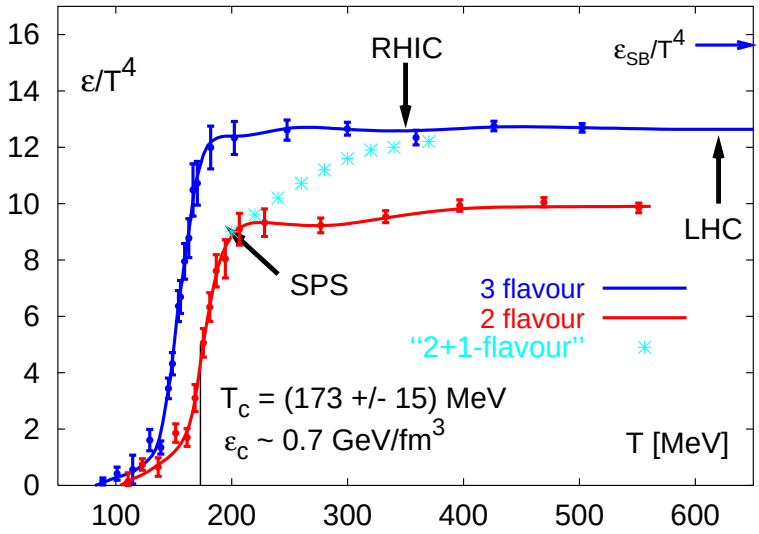

Figure 2.1: Energy density ε as a function of temperature, obtained by numerical evaluation of lattice QCD. ε is divided by T^4 to show the sudden increase, which occurs when the temperature is about 170 MeV (T_c). This behaviour is typical of phase transition [20].

$$V_0(r) = \left(\frac{e_0^2}{r}\right) \tag{2.1}$$

where r denotes the distance between them. In a dense environment of many other charges, the potential becomes screened,

$$V(r) = \left(\frac{e_0^2}{r}\right) \exp(-\mu r) \tag{2.2}$$

where $r_D = \mu^{-1}$ is the Debye screening radius of the medium; it decreases as the charge density of the medium increases. Thus the potential between two test charges a fixed distance apart becomes weaker with increasing density. This occurs because the other charges in the medium partially neutralize the test charges and thereby shorten the range of the interaction.

If a bound state, such as a hydrogen atom, is put into such a medium, the screening radius r_D will for sufficiently high density become less than the binding radius of the atom. The effective force between proton and electron has become so short-ranged that the two can no longer bind. Thus insulating matter, consisting of bound

electric charges, will at sufficiently high density become conducting: it will undergo a *phase transition*, in which charge screening dissolves the binding of the constituents, leading to a plasma of unbound charges as a new state of matter.

The interaction of quarks in QCD is based on their intrinsic color charge, and in a dense medium this charge can be screened in much the same way as an electric charge. Hadrons are color-neutral bound states of colored quarks; hence dilute hadronic matter is a color insulator. At sufficiently high density, however, we expect color screening to set in, so that the potential

$$V_0(r) \sim \sigma r, \tag{2.3}$$

becomes screened

$$V(r) \simeq \sigma r \left[\frac{1-\exp(-\mu r)}{\mu r}\right] \tag{2.4}$$

as above. The color screening mass μ here is also the inverse of the screening radius for color charges. The resulting exponential damping of the binding force will remove all long range effects and in a sufficiently dense medium 'melt' hadrons just as Debye screening dissociated hydrogen atoms. Color screening will thus transform a color insulator into a color conductor, turning hadronic matter into a quark plasma. The transition from insulator to conductor by charge screening is a collective effect, so that we expect a phase transition at the point of plasma formation.

When the atomic matter is transformed from an insulator into a conductor, the effective mass of the conduction electrons is changed. In insulators, the electrons occur with their physical mass; in the conducting phase, however, they acquire a different, *effective* mass, due to the presence of the other conducting electrons, the periodic field of the charged ions and the lattice vibrations. All these effects combine to produce a mean background field quite different from the vacuum. As a result, the insulator-conductor transition is accompanied by a mass shift for the electrons. Similarly, the effective quark mass is expected to change between the confined and the deconfined phase. When confined in hadrons, the basic quarks 'dress' themselves with gluons to acquire an effective constituent quark mass of about 300 MeV (1/3 of the proton or 1/2 of the ρ-meson mass). On the other hand, the basic bare quarks in the QCD Lagrangian are almost massless, so that the mass of the constituent quarks in the confined phase must be generated spontaneously through the confinement interaction. Hence it is likely that when deconfinement occurs, this additional mass is 'lost' and the quarks revert to their intrinsic 'bare' mass

A Lagrangian with massless fermions (limiting case of the light up and down quarks

in the physical Lagrangian) possesses chiral symmetry; this allows a decomposition of the quarks into independent left- and right-handed massless spin one-half states, which for massive fermions become mixed. For massless quarks, confinement must thus lead to spontaneous breaking of chiral symmetry, deconfinement to its restoration. Hence the mass shift transition in QCD is often referred to as chiral symmetry restoration. It can, but does not need to coincide with deconfinement: when the hadrons are dissolved into quark constituents, the liberated and hence now coloured quarks may still interact to form coloured bound states. Thus at low temperature and high density, the quark triplets in nucleons, once deconfined, might choose to recombine into massive coloured quark pairs, similar to Cooper pairs in QED. When the density is increased further, the diquarks would break up into the massless basic quarks. This results in a three-phase picture of strongly interacting matter, with hadronic matter as confined phase, then deconfinement, followed by a phase consisting of massive coloured diquark systems, and finally, after chiral symmetry restoration, a plasma of coloured massless quarks and gluons. Such a three-phase structure would correspond to the succession of insulator, superconductor and conductor in atomic matter.

The transition from hadronic matter to quark-gluon plasma can be illustrated in a simple model. For an ideal gas of massless pions, the pressure as function of the temperature is given by the Stefan-Boltzmann form

$$P_\pi = 3\frac{\pi^2}{90}T^4 \tag{2.5}$$

where the factor 3 accounts for the three charge states of the pion. The corresponding form for an ideal quark-gluon plasma with two flavours and three colours is

$$P_{qg} = \{2\times 8+\frac{7}{8}(3\times 2\times 2\times 2)\}\frac{\pi^2}{90}T^4 - B = 37\frac{\pi^2}{90}T^4 - B. \tag{2.6}$$

In equation 2.6, the first temperature term in the curly brackets accounts for the two spin and eight colour degrees of freedom of the gluons, the second for the three colour, two flavour, two spin and two particle-antiparticle degrees of freedom of the quarks, with 7/8 to obtain the correct statistics. The bag pressure B takes into account the difference between the physical vacuum and the ground state for quarks and gluons in a medium.

This simple model thus leads to a two-phase picture of strongly interacting matter, with a hadronic phase up to

$$T_c = \left(\frac{45}{17\pi^2}\right)^{1/4} B^{1/4} \simeq 0.72\, B^{1/4} \tag{2.7}$$

and a quark gluon plasma above this critical temperature. From hadron spectroscopy, the bag pressure is given by $B^{1/4} \simeq 0.2$ GeV, so that we obtain

$$T_c \simeq 145 \text{ MeV} \tag{2.8}$$

as the deconfinement temperature. This simple estimate is close to the value obtained in lattice QCD.

The energy densities of the two phases of our model are given by

$$\varepsilon_\pi = \frac{\pi^2}{10} T^4 \tag{2.9}$$

and

$$\varepsilon_{qg} = 37\frac{\pi^2}{30} T^4 + B \tag{2.10}$$

From strong interaction thermodynamics, based on QCD as the input dynamics, the Lagrangian is defined

$$\mathscr{L} \;=\; -\frac{1}{4} F^a_{\mu\nu} F^{\mu\nu}_a \;-\; \sum_f \bar{\psi}^f_\alpha (i\gamma^\mu \partial_\mu + m_f - g\gamma^\mu A_\mu)^{\alpha\beta} \psi^f_\beta \;, \tag{2.11}$$

with

$$F^a_{\mu\nu} \;=\; (\partial_\mu A^a_\nu - \partial_\nu A^a_\mu - g\, f^a_{bc} A^b_\mu A^c_\nu) \tag{2.12}$$

Here A^a_μ denotes the gluon field of colour a (a=1,2,...,8) and ψ^f_α the quark field of colour α (α=1,2,3) and flavour f; the input ('bare') quark masses are given by m_f. With the dynamics thus determined, the corresponding thermodynamics is obtained from the partition function, which is most suitably expressed as a functional path integral,

$$Z(T,V) = \int dA\, d\psi\, d\bar{\psi}\, \exp\left(-\int_V d^3x \int_0^{1/T} d\tau\, \mathscr{L}(A,\psi,\bar{\psi})\right) \tag{2.13}$$

since this form involves directly the Lagrangian density defining the theory. The spatial integration in the exponent of equation 2.13 is performed over the entire spatial volume V of the system; in the thermodynamic limit it becomes infinite. The time component x_0 is 'rotated' to become purely imaginary, $\tau = ix_0$, thus turning the Minkowski manifold, on which the fields A and ψ are originally defined, into a Euclidean space. The integration over τ in equation 2.13 runs over a finite slice whose thickness is determined by the temperature of the system.

From $Z(T,V)$, all thermodynamical observables can be calculated in the usual form. Thus

$$\varepsilon = (T^2/V)\left(\frac{\partial \ln Z}{\partial T}\right)_V \tag{2.14}$$

gives the energy density, and

$$P = T\left(\frac{\partial \ln Z}{\partial V}\right)_T \tag{2.15}$$

the pressure. For the study of critical behaviour, long range correlations and multi-particle interactions are of crucial importance; hence perturbation theory cannot be used. The necessary non-perturbative regularization scheme is provided by the lattice formulation of QCD; it leads to a form which can be evaluated numerically by computer simulation. The first variable to consider is the deconfinement measure given by the Polyakov loop

$$L(T) \sim \lim_{r\to\infty} \exp\{-V(r)/T\} \tag{2.16}$$

where $V(r)$ is the potential between a static quark-antiquark pair separated by a distance r. In the limit of large input quark mass, $V(\infty) = \infty$ in the confined phase, so that then $L = 0$. Colour screening, on the other hand, makes $V(r)$ finite at large r, so that in the deconfined phase, L does not vanish. It thus becomes an 'order parameter' like the magnetization in the Ising model; this is zero at high temperatures, but becomes non-zero below the Curie point, when the 'up-down' Z_2 symmetry of the Ising Hamiltonian is spontaneously broken. In the large quark mass limit, QCD reduces to pure $SU(3)$ gauge theory, which is invariant under a global Z_3 symmetry. The Polyakov loop provides a measure of the state of the system under this symmetry: it vanishes for Z_3 symmetric states and becomes finite when Z_3 is spontaneously broken. Hence the critical behaviour of the Ising model (and more generally, Z_N spin systems) as well as that of $SU(N)$ gauge theories is based on the spontaneous symmetry breaking of a global Z_N symmetry.

For finite quark mass m_q, $V(r)$ remains finite for $r \to \infty$, since the 'string' between the two colour charges 'breaks' when the corresponding potential energy becomes equal to the mass M_h of the lowest hadron; beyond this point, it becomes energetically more favourable to produce an additional hadron. Hence now L no longer vanishes in the confined phase, but only becomes exponentially small there,

$$L(T) \sim \exp\{-M_h/T\} \tag{2.17}$$

here M_h is of the order of the ρ-mass, so that $L \sim 10^{-2}$, rather than zero. Deconfinement is thus indeed much like the insulator-conductor transition, for which the order parameter, the conductivity $\sigma(T)$, also does not really vanish for $T > 0$, but with $\sigma(T) \sim \exp\{-\Delta E/T\}$ is only exponentially small, since thermal ionization (with ionization energy ΔE) produces a small number of unbound electrons even in the insulator phase.

Figure 2.2 (left) shows lattice results for $L(T)$ and the corresponding susceptibility $\chi_L(T) \sim \langle L^2 \rangle - \langle L \rangle^2$. The calculations were performed for the case of two flavours of light quarks, using a current quark mass about four times larger than that needed for the physical pion mass. We note that $L(T)$ undergoes the expected sudden increase from a small confinement to a much larger deconfinement value. The sharp peak of $\chi_L(T)$ defines quite well the transition temperature T_c, which we shall shortly specify in physical units.

The next quantity to consider is the effective quark mass; it is measured by the expectation value of the corresponding term in the Lagrangian, $\langle \bar{\psi}\psi \rangle(T)$. In the limit of vanishing current quark mass, the Lagrangian becomes chirally symmetric and $\langle \bar{\psi}\psi \rangle(T)$ the corresponding order parameter. In the confined phase, with effective constituent quark masses $M_q \simeq 0.3$ GeV, this chiral symmetry is spontaneously broken, while in the deconfined phase, at high enough temperature, we expect its restoration. In the real world, with finite pion and hence finite current quark mass, this symmetry is also only approximate, since $\langle \bar{\psi}\psi \rangle(T)$ now never vanishes at finite T.

The behaviour of $\langle \bar{\psi}\psi \rangle(T)$ and the corresponding susceptibility $\chi_m \sim \partial \langle \bar{\psi}\psi \rangle / \partial m_q$ are shown in figure 2.2 (right), calculated for the same case as above in figure 2.2 (left). Here the expected sudden drop of the effective quark mass and the associated sharp peak in the susceptibility. The temperature at which this occurs coincides with that obtained through the deconfinement measure. We therefore conclude that at vanishing baryon number density, quark deconfinement and the shift from constituent to current quark mass coincide.

Next we turn to the behaviour of energy density ε and pressure P at deconfinement. In figure 2.2 (bottom) it is seen that ε/T^4 changes quite abruptly at the above determined critical temperature $T = T_c$, increasing from a low hadronic value to nearly

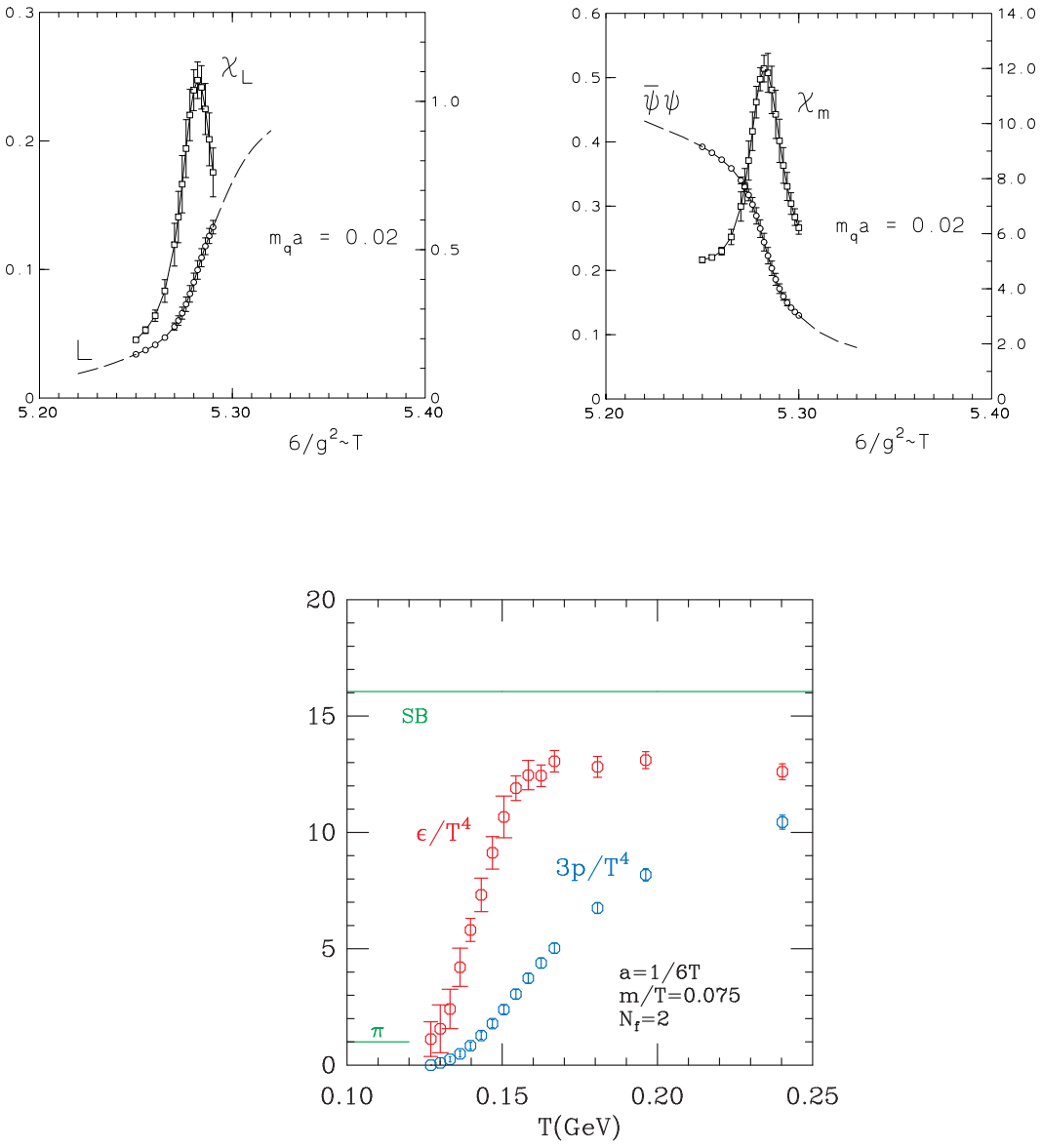

Figure 2.2: The temperature dependence of the Polyakov loop and the associated susceptibility in two-flavour QCD (left) and the temperature dependence of the chiral condensate, the associated susceptibility in two-flavour QCD (right) and the temperature dependence of energy density and pressure in two-flavour QCD (bottom)

that expected for an ideal gas of quarks and gluons. Besides the sudden increase at deconfinement, there are two further points to note. In the region $T_c < T < 2\ T_c$, ε and $3P$ do not yet coincide, as also found in the simple model of the previous section; much of the difference is presumably due to the difference between physical vacuum and QCD in-medium ground state. Furthermore the thermodynamic observables do not quite reach their Stefan-Boltzmann values (marked 'SB' in figure 2.2 bottom) even at very high temperatures. These deviations from ideal gas behaviour can be expressed to a large extent in terms of effective 'thermal' masses $m_{\rm th}$ of quarks and gluons, with $m_{\rm th} \sim gT$.

Finally we turn to the value of the transition temperature. Since QCD (in the limit of massless quarks) does not contain any dimensional parameters, T_c can only be obtained in physical units by expressing it in terms of some other known observable which can also be calculated on the lattice, such as the ρ-mass, the proton mass, or the string tension. In the continuum limit, all different ways should lead to the same result. Within the present accuracy, they define the uncertainty so far still inherent in the lattice evaluation of QCD. Using the ρ-mass to fix the scale leads to $T_c \simeq 0.15\ \mathrm{GeV}$, while the string tension still allows values as large as $T_c \simeq 0.20 \mathrm{GeV}$. This means that energy densities of some 1 - 2 GeV/fm^3 are needed in order to produce a medium of deconfined quarks and gluons [21].

2.2. QGP: Experimental study

The predictions made by QCD have led to the production and study of the quark-gluon plasma in the laboratory. The idea to produce this state of matter experimentally is colliding heavy nuclei with a speed approaching that of light, to increase the energy density in the medium above the energy of deconfinement

When the nuclei travel at a speed close to speed of light, they suffer a Lorentz contraction in the direction of movement so in the center of mass reference frame the collision looks like the collisions of two almost flat nucleons. When the impact parameter of the collision b, *i.e.,* the distance between the centers of the two nuclei, is small, we call the collision $central$ and when is large, $peripheral$. It is expected that central collisions are those that generate higher energy density and therefore are candidates for the formation of QGP.

When two nucleons hits, each nucleon may scatter several times and the liberated partons from different nucleon-nucleon collisions rescatter with others before hadronization. This features change the particle prediction per participating nucleon but the rescattering process leads to a state of local thermal equilibrium, by redistibuting the energy lost by beam into the statistically most probable configurations. This rescattering is the thermodynamics pressure acting against the outside vacuum which cause the expansion of the reaction zone. The expansion cools and

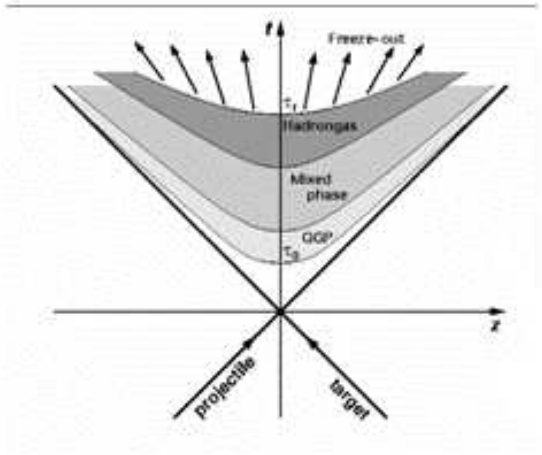

Figure 2.3: *Space-time diagram of longitudinal evolution of the quark-gluon plasma*

dilutes the fireball below the critical energy density of the quark-hadron transition, at which point hadrons are formed from the quarks and gluons (hadronization). Further interactions between these hadrons cease once their average distance exceeds the range of strong interactions, this last phase is called the thermal equilibrium. Finally these hadrons are detected experimentally. Thus, the temporal evolution of the system which is formed by the collision can be separated into 4 stages: a pre-equilibrium, followed by the formation of plasma, then hadronization and finally thermal equilibrium. This process is shown in the space-time diagram in Figure 2.3.

To estimate the energy density, Bjorken [22] modeled the expansion process assuming that the finally observed hadrons have emerged from an initial interaction volume in free flow *i.e.,* without any collective motion. The resulting initial energy density in an $Au+Au$ collision is

$$\varepsilon_0 = \frac{p_0}{\pi R_A^2 \tau_0} (\frac{dN_h}{dy})_{y=0}^{AA} \tag{2.18}$$

where p_0 denotes the average (local) energy of the emitted secondaries and (dN_h/dy) their multiplicity. The initial interaction volume is determined by the transverse size R_A and the longitudinal extension as obtained from the formalization time τ_0, which is generally taken to be about 1 fm.

For $Au+Au$ collisions

$$(\frac{dN_h}{dy})^{AA}_{y=0} = A^{0.48} ln \frac{\sqrt{s}}{2m} \tag{2.19}$$

then, the initial density is

$$\varepsilon_0 = \frac{p_0}{4} A^{0.48} ln \frac{\sqrt{s}}{2m} [\mathrm{GeV}/fm^3] \tag{2.20}$$

If the particles produced are pions $p_0 = 0.5$ GeV. ε_0 for different experiments are shown in table 2.1.

Machine	Start	Type	Beam	$\sqrt{s}$ [GeV/A]	ε_0^{AB} [GeV/fm^3]
BNL-AGS	1986	Fixed Target	^{28}Si	5	0.7
CERN-SPS	1986	Fixed Target	$^{16}O, ^{32}S$	19	1.6
BNL-AGS	1992	Fixed Target	^{197}Au	5	1.5
CERN-SPS	1994	Fixed Target	^{208}Pb	17	3.7
BNL-RHIC	2000	Collider	^{197}Au	200	7.6
CERN-LHC	2010	Collider	^{208}Pb	2760	12.8

Table 2.1: Experimental facilities for high energy nuclear collisions

The experimental investigation of the quark-gluon plasma requires selection of appropriate signals related to its formation. A problem present in the study of this new state of matter is that the size and lifetime is very short, just few fermis of diameter and 5 to 10 fm/c of duration, so it is impossible to detect it directly macroscopically. Besides, plasma signals compete with the signals emitted by the hadron gas and can be modified by that stage. Despite this, large number of ideas to identify and study their formation have been proposed

Kinematics probes

The basic concept behind these is the determination of energy density ε, pressure P and the entropy s as a function of temperature T and baryonic chemical potential μ_B. Some observations related to these quantities are average transverse momentum $\langle p_T \rangle$ and the distribution of particles or energy as a function of pseudorapidity dN/dη and dE/dη respectively. In these cases you want to see that the system reached

thermodynamic equilibrium and attempts to extract parameters of its equation of state.

Also interferometric correlations between particles identities are of interest to study the size of the system created. For example $\pi\pi$ and KK provide information of the space-time dynamics of nuclear collisions. Studying correlation between two particles at different points in space phase, it is possible to obtain information on size, time life and the flow of plasma until hadronization.

Electromagnetics probes

The most direct signals are those produced by the *direct photons*, that is, the photons that are not produced by the decay of hadrons after thermal equilibrium. Since photons do not feel any strong interaction, because they have no color charge, they escape the medium without interacting with it. These photons are emitted through the expansion of plasma and its production is expected to be principally in the initial hot and dense states. Unfortunately, direct photons are rare, and the photons produced after thermal equilibrium are many. However, it is predicted that the spectrum of direct photons is much harder than the photons coming from decays so, their presence could be measured.

Deconfinement probes

Strangeness was one of the first proposed signatures of the deconfined phase. The mass of strange quarks and antiquarks is of the same magnitude as the temperature T_c other hadrons are expected to disolve into quarks. The dominant mechanism for cooking up strangeness in quark-gluon deconfined matter was found to be the gluon-fusion reaction $gg \longrightarrow s\overline{s}$. The strange particles decay into lighter quarks, thus, strageness-carrying hadrons decay by weak interactions that occur, in general, on a time scale that is extremely long compared with nuclear-collision times. This make it relatively easy to detect the strange particle through the tracks left by their decay products.

Other particles formed in the plasma are hadrons with charm quarks *c*. Since the charm quark is about ten times heavier than the strange quark, pairs of charm quarks can be formed only during the very early stages of the collision, as the nuclei begin to penetrate each other. At this early stage the colliding particles have the energy to overcome the high energy threshold. If the QGP phase is formed, these charmed quark have less chance of forming charmonium states, because the gluons present within the plasma hinder their binding, or/and break the bound states.

Matsui and Satz suggested that due to the high gluonic density resulting from color deconfinement, it is posible to produce a potential interactions screening between

pairs of quarks c y $\overline{c}$ produced during the initial collisions of the nuclei, preventing the formation of states ($c\overline{c}$) J/ψ, ψ', χ_c. However, these quarks c, can find other quarks to form different hadrons with open charm ($\overline{c}q$ and $c\overline{q}$). This leads to the suppression in the production of bound states weakly bounded , $\psi\,'$ and χ_c and strongly bound J/ψ [23].

Parton energy loss

One more of the existing proposals to detect the creation of quark-gluon plasma is parton energy loss. In 1982 Bjorken [3] suggested that partons traveling with high speed in the quark-gluon plasma, could lose large amounts of energy by elastic collisions with plasma components. Gyulassy, Plümer and X.N. Wang [4] identified loss of radiation due to the jet suppression incorporating Landau-Pomeranchuk-Migdal interface effect. Subsequently Baier, Dokshitzer, Mueller, Peigné and Schiff [5] studied radiative parton energy loss where multiple parton scattering was modeled by a screened Coulomb potential. The predictions for this energy loss were improved by Gyulassy, Levai, Vitev [6] and Wiedemann [7] considering finite opacity.

A simple estimation can be given by the thermal averaged energy transfer $v_e l \simeq q_T^2/2\omega$ of the jet parton to a thermal parton with energy ω, q_T being the transverse momentum transfer of the elastic scattering. The resulting energy loss

$$\frac{dE_{el}}{dx} = C_2 \frac{3\pi\alpha_s^2}{2} T^2 ln \frac{3ET}{2\mu^2} \tag{2.21}$$

is sensitive to the temperature of the thermal medium but is small compared to radiative energy loss. Here μ is the Debay screening mass and C_2 is the Casimir factor of the parton.

The radiative parton energy loss in the plasm of size L is estimated as

$$\frac{dE_{rad}}{dx} = C_2 \frac{\alpha_s \mu^2}{4} \frac{L}{\lambda} ln \frac{3E}{\mu L} \tag{2.22}$$

where λ is the gluon's mean free-path in the medium. Using this result one can estimate the total energy loss for a parton with initial energy $E = 40$ GeV to be about $\Delta E \simeq 10$ GeV after it propagates a distance $L = 6$ fm in a medium with $\mu = 0.5$ GeV and $\lambda = 1$ fm.

This leads to a significant dependence of energy loss ΔE of the fast parton. With these results improvements can maintain hope that the loss of energy can serve as quantitative test of the density and temporal evolution of the quark-gluon plasma created in heavy ions collisions.

Chapter 3

Experimental programs

Dedicated programs to create and study the QGP phase have started in early eighties with collisions of heavy-ions at relativistic energies. The search and study of QGP started first with the Au beam at 1 A.GeV at the Bevalac in Berkeley. The next milestone came with the acceleration of Au beam at 11.7 AGeV at the BNL-AGS and Pb beam at 158 A.GeV at the CERN-SPS. First hints of the formation of a new state of matter has been obtained from the SPS data [24]. The Relativistic Heavy Ion Collider (RHIC) started becoming operational in the year 2000 with $Au+Au$ collisions at $\sqrt{s_{\rm NN}} = 130$ GeV and soon after to top $Au+Au$ energies of $\sqrt{s_{\rm NN}} = 200$ GeV [25]. The RHIC experiments bring out highest quality data from $p+p$, $d+Au$, $Cu+Cu$ and $Au+Au$ at various energies, strong evidence for the production of extreme hot and dense matter has been seen. RHIC results, in combination with the ones from AGS and SPS , have enhanced our understandings of the QCD matter at different temperatures and densities. In October 1990 was proposed the Large Hadron Collider (LHC), emphasized the idea of providing $p+p$ collisions as well as heavy-ions [26].

3.1. Relativistic Heavy Ion Collider

The Relativistic Heavy Ion Collider (RHIC) was built to create and investigate strongly interacting matter. There are four heavy-ion experiments at RHIC which have studied $Au+Au$ collisions at three center-of-mass energies: $\sqrt{s_{\rm NN}} = 62.4$, 130 and 200 GeV, the experiments are: BRAHMS (Broad Range Hadron Magnetic Spectrometers Experiment at RHIC), PHOBOS, PHENIX (Pioneering High Energy Nuclear Interaction Experiment) and STAR (Solenoidal Tracker at RHIC).

The results from the four RHIC experiments demonstrated the capability to reach extreme conditions during the early stages of nucleus-nucleus collisions, forming matter that exhibits heretofore unobserved behavior. In particular, evidence for jet energy loss has been reported: the suppression in the nuclear modification factor

for central $Au+Au$ events $R_{\rm AA}$, away-side correlations in central $Au+Au$ collisions compared to $p+p$ collisions

Figure 3.1 and figure 3.2 show the most significant high p_T measurements made at RHIC. Both figures incorporate measurements of $p+p$, $d+Au$ and centrality selected $Au+Au$ collisions at $\sqrt{s_{\rm NN}} = 200$ GeV, where $p+p$ and $d+Au$ systems providing benchmarks for phenomena seen in the more complex $Au+Au$ collisions.

Figure 3.1 shows the nuclear modification factor, $R_{\rm AB}$, defined as the ratio of the inclusive momentum spectrum of charged hadrons yields in A+B (either $Au+Au$ or $d+Au$) events to a $p+p$ reference spectrum, scaled to account for the nuclear geometry effects via $< N_{bin} >$. The calculated mean number of binary nucleon-nucleon collisions contributing to each A+B centrality bin:

$$R_{\rm AB} = \frac{dN_{AB}/d\eta d^2p_T}{T_{AB}d\sigma_{NN}/d\eta d^2p_T}. \tag{3.1}$$

where the overlap integral $T_{AB} =< N_{bin} > /\sigma^{pp}_{inelastic}$.

High-p_T hadrons in central $Au+Au$ collisions are suppressed by a factor ~ 5 relative to naive (binary scaling) expectations. Conventional nuclear effects, such as nuclear shadowing of the parton distribution functions and initial state multiple scattering, cannot account for the suppression. Furthermore, the suppression is not seen in $d+Au$ but is unique to $Au+Au$ collisions, proving experimentally that it results not from nuclear effects in the initial state (such as gluon saturation), but rather from the final state interaction of hard scattered partons or their fragmentation products in the dense medium generated in $Au+Au$ collisions [27, 28, 29, 8].

This dominant final state interaction in $Au+Au$ is presumably superimposed on a variety of interesting initial-state effects revealed by the $d+Au$. The enhancement seen in figure 3.1 in $R_{\rm dAu}$ for moderate p_T and mid-rapidity, known as the Cronin effect [32], is generally attributed [33, 34, 35] to the influence of multiple parton scattering through cold nuclear matter *prior to* the hard scattering that produces the observed high-p_T hadron.

Figure 3.2 shows STAR measurements of correlations between high p_T hadrons. The top panel shows the azimuthal distribution of hadrons with p_T>2 GeV/c relative to a trigger hadron with $p_T^{\rm trig}$ >4 GeV/c. A hadron pair drawn from a single jet will generate an enhanced correlation at $\Delta\phi \approx 0$, as observed for $p+p$, $d+Au$ and $Au+Au$. A hadron pair drawn from back-to-back dijets will generate an enhanced correlation at $\Delta\phi \approx \pi$, as observed for $p+p$ and for $d+Au$ with somewhat broader width than the near-side correlation peak. However, the back-to-back dihadron correlation is absent in central $Au+Au$ collisions, while for peripheral $Au+Au$ collisions the corre-

lation appears quite similar to that seen in $p+p$ and $d+Au$. If the correlation is indeed the result of jet fragmentation, the suppression is again due to the final state interaction of hard-scattered partons or their fragmentation products in the dense medium generated in $Au+Au$ collisions [8]. In this environment, the hard hadrons we do see (and hence, the near-side correlation peak) would arise preferentially from partons scattered outward from the surface region of the collision zone, while the away-side partons must burrow through significant lengths of dense matter.

A more differential probe of partonic energy loss is the measurement of high p_T dihadron correlations relative to the reaction plane orientation. The bottom panel of figure 3.2 shows a study from STAR of the high p_T dihadron correlation from 20-60% centrality $Au+Au$ collisions, with the trigger hadron situated in the azimuthal quadrants centered either in the reaction plane ('in-plane') or orthogonal to it ('out-of-plane') [31]. The same-side dihadron correlation in both cases is similar to that in $p+p$ collisions. In contrast, the suppression of the back-to-back correlation depends strongly on the relative angle between the trigger hadron and the reaction plane. This systematic dependence is consistent with the picture of partonic energy loss: the path length in medium for a dijet oriented out of the reaction plane is longer than in the reaction plane, leading to correspondingly larger energy loss. The dependence of parton energy loss on path length is predicted linear. The orientation dependence of the energy loss should be further affected by different rates of matter expansion in-plane *vs.* out-of-plane.

While large effects of energy loss in dense matter have been observed, precision data in a larger p_T range are needed to fully explore this phenomena and their connection to properties of the dense matter. The region $2 < p_T < 6$ GeV/c has significant contributions from non-perturbative processes other than vacuum fragmentation of partons, perhaps revealing novel hadronization mechanisms. Most studies to date of azimuthal anisotropies and correlations of jets have by necessity been constrained to this region, with only the inclusive spectra extending to the range where hard scattering is expected to dominate the inclusive yield. High statistics data sets for much higher p_T hadrons are needed to fully exploit azimuthal asymmetries and correlations as measurements of partonic energy loss. Dihadron measurements probing the details of the fragmentation process may be sensitive to the energy density, in addition to the gluon density that is probed with the present measurements.

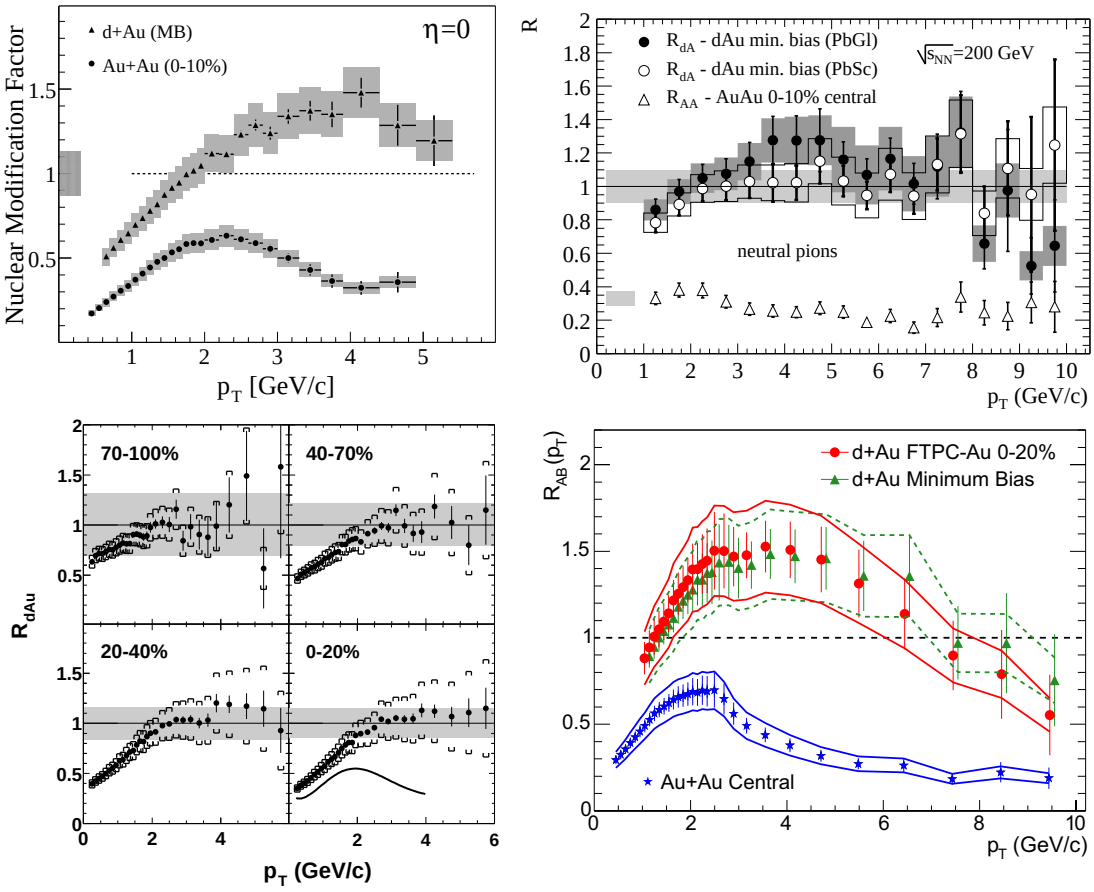

Figure 3.1: Binary-scaled ratio R_{AB} of charged hadron and π_0 inclusive yields from $\sqrt{s_{\mathrm{NN}}} = 200$ GeV $Au+Au$ and $d+Au$ relative to that from $p+p$ collisions, from BRAHMS [27] (upper left), PHENIX [28] (upper right), PHOBOS [29] (lower left) and STAR [8] (lower right). The PHOBOS data points in the lower left frame are for $d+Au$, while the solid curve represents PHOBOS central (0-6%) $Au+Au$ data. The shaded horizontal bands around unity represent the systematic uncertainties in the binary scaling corrections.

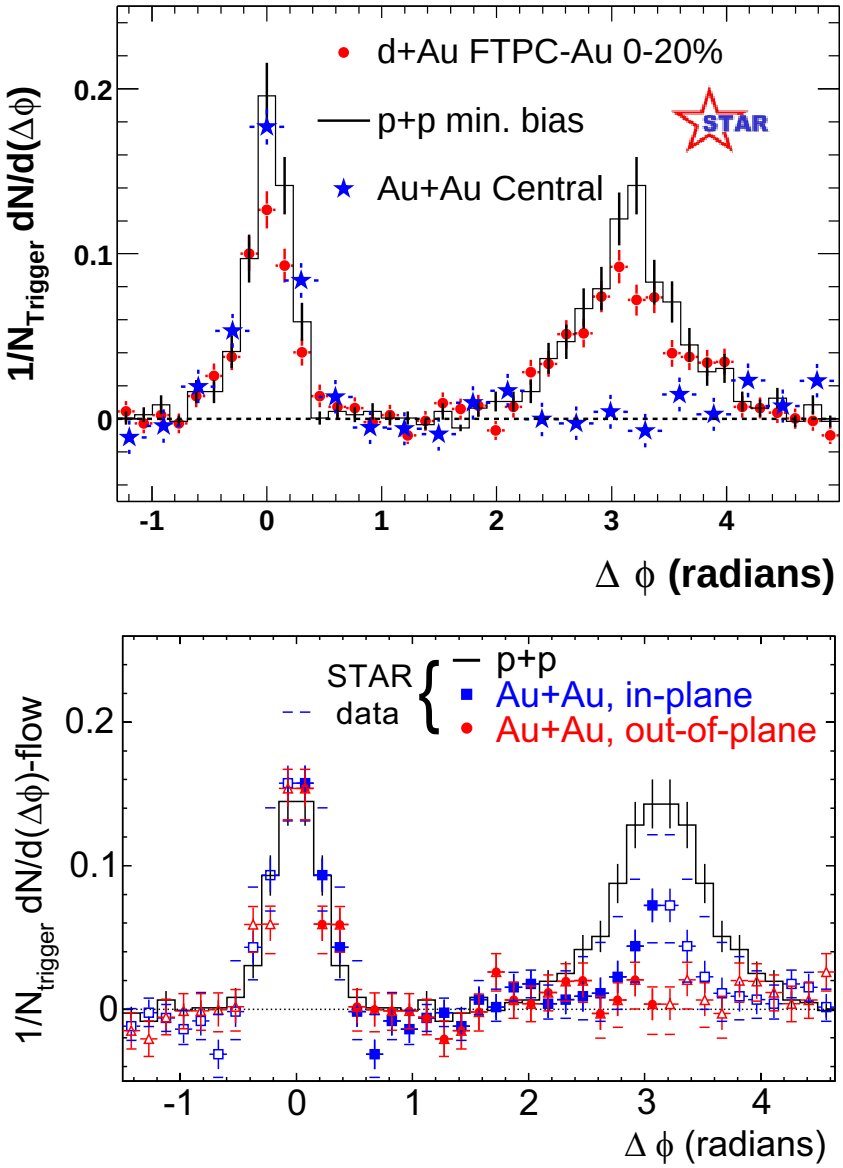

Figure 3.2: Dihadron azimuthal correlations at high p_T. Top panel shows correlations for $p+p$, central $d+Au$ and central $Au+Au$ collisions (background subtracted) from STAR [8, 30]. Bottom panel shows the background-subtracted high p_T dihadron correlation for different orientations of the trigger hadron relative to the $Au+Au$ reaction plane [31].

3.2. Large Hadron Collider

The Large Hadron Collider (LHC) is designed to deliver colliding $p+p$ beams at center-of-mass energies of 14 TeV and $Pb+Pb$ beams at $\sqrt{s_{\mathrm{NN}}} = 5.5$ TeV. The $p+p$ collisions offer the possibility of discovering the Higgs Boson, the missing link in the standard model and the aim of the heavy-ion physics program is to study QGP.

In the CERN accelerator complex (see figure 3.3), the ions pass into the Low Energy Ion Ring (LEIR), then proceed to the PS, the SPS and finally to the LHC.

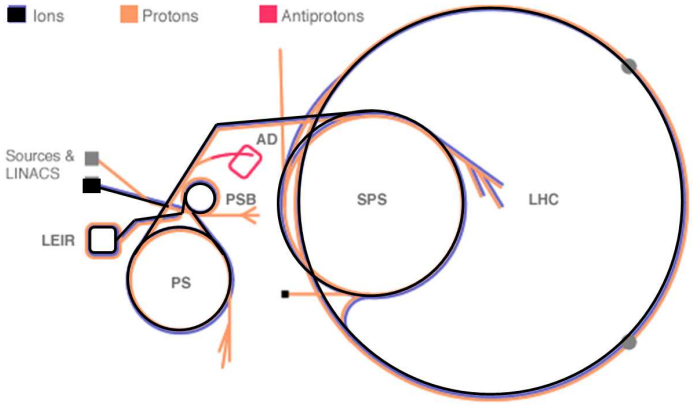

Figure 3.3: The CERN accelerator complex. The ions pass through the LEIR, then to the PS, the SPS and finally to the LHC.

The typical expected yearly running times of LHC are of the order of 10^7 seconds for $p+p$ collisions and 10^6 seconds for heavier systems. Table 3.2 gives the center-of-mass energy and expected luminosity at LHC for some typical collision systems. Due to the limited rate capability of the ALICE detector, the luminosity for $p+p$ collisions will be limited to a maximum of $10^{31}\mathrm{cm}^{-2}\mathrm{s}^{-1}$.

A comparison of some of the basic parameters measured at the SPS and RHIC with expected values for the LHC are given in table 3.2. The table lists the pseudorapidity density of charged particles ($\mathrm{dN}_{ch}/d\eta$), formation time of QGP (τ_0), the energy density (ε) for τ_0 = 1, the initial temperature in terms of the critical temperature (T_{c}), QGP life time (τ_{QGP}) and the freezeout time (τ_f) for the top center-of-mass energies ($\sqrt{s_{\mathrm{NN}}}$) of these accelerators. At the LHC, with the increase of beam energy to about 28 times more compared to that of RHIC, the number of charged particles from the produced fireball increase by more than three times, the formation time of the QGP decreases significantly, the matter becomes much hotter, denser and long lived. All these conditions are conducive to opening up new physics domain at the LHC.

System	$\sqrt{s_{\mathrm{NN}}}$(TeV)	L_0(cm^{-2}s^{-1})	σ_{geom}(b)
$p+p$	14.0	10^{34}	0.1
$Pb+Pb$	5.5	10^{27}	7.7
$p+Pb$	8.8	10^{29}	1.9
$Ar+Ar$	6.3	10^{29}	2.7

Table 3.1: Luminosities expected for different collision systems with different center-of-mass energies [36].

Condition	SPS	RHIC	LHC
$\sqrt{s_{\mathrm{NN}}}$ (GeV)	17.3	200	5500
dN_{ch}/dη	450	600	$1200-4000$
τ_0 (fm/c)	$\sim$1	$\sim$0.2	$\sim$0.1
ε(GeV/fm^3)	2.5	4-5	10-40
T/T_{c}	1.1	1.9	$3-4$
τ_{QGP} (fm/c)	$\sim$1	$2-4$	$>$4
τ_f (fm/c)	$\sim$10	$\sim$20	$\sim$30

Table 3.2: Conditions created in central heavy-ion collisions at the top energies of SPS , RHIC and projections for LHC.

The ALICE (A Large Ion Collider Experiment) experiment at the LHC is designed specifically for heavy-ion physics [1, 2]. The other two major experiments, ATLAS and CMS, also have heavy ion programs [37, 38]. Both of these experiments will focus more on jets, photons and muon channels.

3.2.1. The ALICE experiment

ALICE (A Large Ion Collider Experiment) shown in figure 3.4, is a general-purpose heavy-ion detector focuses on QCD, the strong-interaction sector of the Standard Model. It is designed to address the physics of strongly interacting matter and the quark-gluon plasma at extreme values of energy density and temperature in nucleus-nucleus collisions. Besides running with Pb ions, the physics program includes collisions with lighter ions, lower energy running and dedicated proton-nucleus runs. ALICE will also take data with proton beams at the top LHC energy to collect reference data for the heavy-ion programme and to address several QCD top-

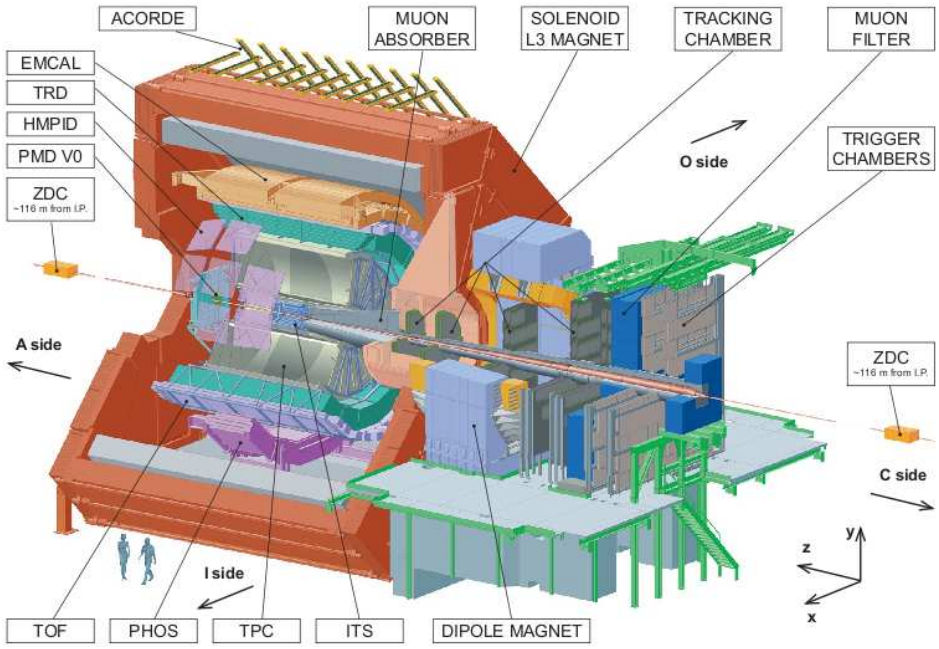

Figure 3.4: Longitudinal view of the ALICE detector.

ics for which ALICE is complementary to the other LHC detectors [39, 40, 41]. The ALICE detector has been built by a collaboration including currently over 1000 physicists and engineers from 105 institutes in 30 countries. Its overall dimensions are 16 x 16 x 26 m^3 with a total weight of approximately 10 000 t. The experiment consists of 18 different detector systems each with its own specific technology choice and design constraints, driven both by the physics requirements and the experimental conditions expected at LHC. The most stringent design constraint is to cope with the extreme particle multiplicity anticipated in central $Pb+Pb$ collisions. The different subsystems were optimized to provide high-momentum resolution as well as excellent Particle Identification (PID) over a broad range in momentum, up to the highest multiplicities predicted for LHC. This will allow for comprehensive studies of hadrons, electrons, muons, and photons produced in the collision of heavy nuclei.

The detector setup can be broadly described by three groups of detectors: the forward detectors, the muon spectrometer and the central barrel.

The forward detectors

The ALICE experiment is equipped with a set of forward detectors, such as the a Forward Multiplicity Detector (FMD), Photon Multiplicity Detector (PMD), Zero Degree

Calorimeters (ZDC), and detectors for trigger and timing (V0, T0). The FMD, consisting of several rings of silicon detectors, covers a very large range in pseudo-rapidity (-3.4 $< \eta <$ -1.7 and 1.7 $< \eta <$ 5.0). The main function of FMD is to provide charged-particle multiplicity information. The V0 detector consists of two arrays (each array with 32 segments) of scintillator counters, called V0A and V0C, which are installed on both sides of the ALICE interaction point. With a time resolution of about 600ps the detector provides minimum-bias triggers for in $p+p$ and $Pb+Pb$ collisions. V0 detector helps in monitoring of the beam luminosity and reducing the beam-gas contributions.

The T0 detector consists of two arrays of Čerenkov counters (12 counters per array) and has an excellent time resolution (about 50ps). The main purpose of T0 detector is to provide start time (T0) for the TOF detector. T0 detector also measures the vertex position and performs several trigger related functions.The Photon Multiplicity Detector (PMD) measures the multiplicity and spatial distribution of photons event-by-event in the region 2.3 $< \eta <$ 3.7. It consists of two planes of gas proportional counters with cellular honeycomb structure, preceded by two lead converter plates of 3 radiation lengths each. Two sets of two compact calorimeters each will be used to measure and trigger on the impact parameter of the collision (Zero Degree Calorimeter ZDC). They are made of tungsten (neutron calorimeters, ZN) and brass (proton calorimeters, ZP) with embedded quartz fibres, and located on both sides in the machine tunnel, about 116m from the interaction region. In addition, two small electromagnetic calorimeters (ZEM) are installed on one side, 7 m from the vertex, to improve the centrality selection.

The muon spectrometer

The forward muon arm is primarily designed to measure the production of heavy quarkonia ($J/\psi, \psi', \Upsilon, \Upsilon', \Upsilon''$) via their decay in the $\mu^+\mu^-$ channel. The spectrometer acceptance covers the pseudorapidity interval $2 \leq \eta \leq 4$ and the resonances can be detected down to zero transverse momentum. The invariant mass resolution is of the order of 70 MeV in the J/ψ region. The spectrometer consists of a front absorber ($\sim 10\lambda_{int}$) which absorbs hadrons and photons from the interaction vertex, a large dipole magnet, a highly granular tracking system and a trigger system placed behind a passive muon filter wall.

The central barrel

The central barrel consists of the Inner Tracking System (ITS), Time Projection Chamber (TPC), Transition Radiation Detector (TRD), the Time of Flight (TOF) detector and the electromagnetic calorimeter. The design goal is to have low material budget and low magnetic field (B$\leq$ 0.5 T) in order to be sensitive to low-p_T particles.

The ITS consists of six layers of silicon detectors. The two innermost layers consist of silicon pixel detectors (which covers up to the $|\eta| < 1.98$), followed by two layers of silicon drift detectors and the last two outer layers are of silicon strip detectors. The ITS is designed to handle the high particle density expected in $Pb+Pb$ collisions. The main uses of ITS will be to (i) determine the primary vertex of the collision, (ii) localize the secondary vertices for decays of hyperons and D and B mesons, (iii) track and identify particles with momentum below 200 MeV/c, (iv) improve the tracking in the central barrel and (v) provide minimum bias and high multiplicity triggers.

The TPC is the main tracking detector of ALICE. It is cylindrical in shape. The active volume has an inner radius of 85 cm, an outer radius of 250 cm, and an overall length along the beam direction of 500 cm. With this the coverage of TPC becomes $|\eta| <$ 0.9. The TPC is made of a large cylindrical field cage, filled with 90 m^3 of Ne/CO_2/N_2 (90/10/5), in which the primary electrons are transported over a distance of up to 2.5 m on either side of the central electrode to the end plates. Multi-wire proportional chambers with cathode pad readout are mounted into 18 trapezoidal sectors at each end plate. The TPC is the primary device for obtaining charged-particle momentum measurements and particle identification. It also provides an independent measure of primary vertex. The combination of ITS and a large Time Projection Chamber (TPC) provides powerful tracking with excellent momentum resolutions (about 2% to 5%) from 100 MeV/c to 100 GeV/c.

The central barrel is equipped with a Transition Radiation Detector (TRD) for electron identification above 1 GeV/c, where the pion rejection capability from TPC is no longer sufficient. The TRD, in combination with other central barrel detectors, will provide sufficient electron identification to measure the production of light and heavy vector meson resonances and the dilepton continuum produced in $p+p$ and $Pb+Pb$ collisions. It consists of 540 individual readout detector modules arranged in 18 super modules. Each module consists of a radiator of 4.8 cm thicknes, a multiwire proportional readout chamber along with frontend elctronics. The gas mixture in the readout chamber is Xe/CO_2 (85%/15%). The particle identification of hadrons in the intermediate momentum range (to about 4 GeV/c depending on the particle species) is improved significantly with the inclusion of a Time-Of-Flight (TOF) system.

The TOF system consists of Multi-gap Resistive-Plate Chambers (MRPC). The key aspect of these chambers is that the electric field is high and uniform over the whole sensitive gaseous volume of the detector. Ionization produced by traversing charged particle starts a gas avalanche process which eventually generates the observed signals on the pick-up electrodes. The intrinsic time resolution of 40ps has been achieved with an efficiency of close to 100%.

The central arm includes a High-Momentum Particle Identification Detector (HMPID) for the identification of hadrons at $p_T > 1$ GeV/c. The detector is based on proximity-focusing Ring Imaging Cherenkov (RICH) counters and consists of seven modules of

about 1.5 x 1.5 m^2 each, mounted in an independent support cradle. The coverage of HMPID is limited (-0.6 $< \eta <$ 0.6 with 1.2°$< \phi <$ 58.8°.

The measurements of low p_T direct photons and high-p_T π^0 are performed by a single arm high resolution photon (electromagnetic) spectrometer (PHOS), consisting of lead-tungstate ($PbWO_4$) crystals. The major requirements of the PHOS include the ability to identify photons, discriminate direct photons from decay photons and perform momentum measurements over a wide dynamic range with high energy and spatial measurements. PHOS covers approximately a quarter of a unit of pseudorapidity -0.12 $< \eta <$ 0.12, and 100°in azimuthal angle. The total area is $\sim 8m^2$. Recently, an electromagnetic calorimeter (EMCAL), which will be located inside the L3 magnet, has been included in the ALICE detector, improving the capability for measurement of high energy jets.

3.3. Heavy-Ion physics with ALICE

The heavy-ion program is focused in the study of hot and dense medium can be studied by many observables. In ALICE this probes are subdivided into three classes: soft probes (with the typical momenta $p_T < 2$ GeV/c), heavy-flavor probes (*i.e.,* using the particles having *c* and *b* quarks) and high-p_T probes (in the momentum range above $p_T > 20$ GeV/c).

3.3.1. Soft Probes

ALICE will measure the charged-particle multiplicity and the charged-particle pseudorapidity distribution over almost 8 units of η by means of Forward Multiplicity Detector (FMD) and the innermost layers of ITS. The way the initial energy is redistributed over the particles in the final state is strictly linked with such an important thermodynamical quantity as the energy density ε reached in the early phase of the collision.

Furthermore, the multiplicity information allows one to constrain the hadroproduction models. Thus, in the phenomenological approach, the measured pseudorapidity density $dN_{ch}/d\eta$ is expressed as the sum of a term proportional to the number of participants N_{part} (soft component) and the number of binary collisions N_{coll} (hard component). Measuring $dN_{ch}/d\eta$ as a function of N_{part}, one can estimate the relative number of particles produced in hard and soft scatterings.

Resonances with lifetimes comparable to that of the QGP phase (such as $\rho^0, K^*(892)^0$, $\phi(1020)$) may change their properties (mass, width) when they are produced in the dense medium. Detection of $K^*(892)^0$ and $\phi(1020)$ is especially important because of the expected overall strangeness enhancement in heavy-ion collisions.
The ALICE detector will be able to register these resonances with sufficient statistics and with mass resolution of the order of a few MeV.

3.3.2. Heavy flavor probes

When traversing the dense matter created in nucleus-nucleus collisions, the initially-produced hard partons lose energy mainly on account of medium-induced gluon radiation. The heavy quarks at intermediate p_T will lose less energy as compared with the light quarks at the same momenta due to the 'dead-cone' effect [5,6]. The ratio of the nuclear modification factor for D (and B) mesons to the one for the normal hadrons is thus suggested to be sensitive to the mass dependence of in-medium parton energy loss. The D mesons needed for these studies will be topologically reconstructed in central ALICE detectors, whereas B mesons can be detected in semi-leptonic decay channels.

Precise detection of the open charm (open beauty) is also needed for the normalization of the quarkonia production. In nucleus-nucleus collisions, quarkonium suppression is expected to occur due to the Debye screening in the deconfined matter. Increase of the energy density reached in the collisions leads to break up of first the ψ' and χ_c, and finally the J/ψ . Such a suppression pattern was already observed at SPS. However, at higher energies (RHIC, LHC) the situation becomes more complicated, because the charmonia can be regenerated in the hot medium by recombination.

ALICE will be able to measure the charmonia and bottomnia production both at mid-rapidity (in di-electron channels) and at forward rapidities (in di-muon channels). The statistics of registered $\Upsilon's$ is expected to be enough for the suppression studies. In this case, due to much higher mass, the influence of the regeneration will be negligible.

3.3.3. High-p_T probes

High-p_T partons produced in the initial stage of a nucleus–nucleus collision are expected to undergo multiple interactions inside the collision region prior to hadronisation. Hereby, the energy of the partons is reduced through collisional energy loss and medium-induced gluon radiation, the latter being the dominant mechanism in a QGP. This so-called jet quenching has been suggested to behave very differently in cold nuclear matter and in QGP, and has been postulated as a tool to probe the properties of this new state of matter. This is the main motivation for studying jets as well as high-p_T particle spectra and particle correlations in heavy-ion collisions.

As compared to jet physics at RHIC, there are two fundamentally new features in central $Pb+Pb$ collisions at the LHC: The multi-jet production per event is not restricted to the minijet region $E_T < 2$ GeV but extends to about 20 GeV and jet rates are high at energies at which jets can be distinguished from the background energy of the underlying event. Hence, event-by-event reconstruction of jets with reason-

able energy resolution will be possible.

ALICE will study the whole spectrum of jet production ranging from minijets, $E_T > 2$ GeV, to high-E_T jets of several hundred GeV. Experimental considerations delineate four distinct energy regions, which are discussed here for the 10% most central $Pb+Pb$ collisions at $\sqrt{s_{\rm NN}} = 5.5$ TeV. In the region $E_T < 20$ GeV several jets overlap in one event within the ALICE acceptance. This means that jet identification in the traditional sense is not possible and their presence is revealed via studies of particle correlations. For $20 < E_T < 100$ GeV the jet rate > 1 Hz is high enough so that, even with a read-out rate limited by the TPC to 20–40 Hz, an event sample of $\mathcal{O}(10^4)$ jets can be collected in one effective month of running (10^6 s). For $E_T > 100$ GeV triggering will be necessary to collect jet enriched data. Considering that for a fragmentation function analysis of the order of 10^4 jet events are needed, the statistics limit is reached at about 250 GeV.

Figure 3.5 and table 3.3.3 show the expected average LHC $Pb+Pb$ luminosity of 5×10^{26} cm^{-2}s^{-1}, the number of jets produced per effective month of running (10^6 s) within the fiducial region $|\eta| < 0.5$ for charged jet reconstructed using ALICEcentral barrel tracking (ITS+TPC) and $|\eta| < 0.3$, $83^\circ < \varphi < 157^\circ$ for jet reconstruction with central barrel tracking and Electromagnetic Calorimetry (EMCal). Rates in minimum bias collisions are compared to those in the 10% most central collisions. The latter have been obtained by scaling with the average number of binary collisions for impact parameter $b < 5$ fm.

In the low-E_T-jet region, jet-structure modifications will be studied with inclusive spectra of identified particles and particle correlations, as shown by the RHIC experiments. These studies require excellent low-p_T and PID capabilities and ALICE will extend them with the electromagnetic calorimeter (EMCAL). The EMCAL will increase the selection efficiency and further reduce the bias on the jet fragmentation. Furthermore, it will add a jet trigger which is needed to increase the statistics at high E_T. The low- and high-transverse-momentum tracking capabilities combined with electromagnetic calorimetry represent an ideal tool for jet-structure modification studies at the LHC over a wide kinematic region of jet and associated-particle momenta.

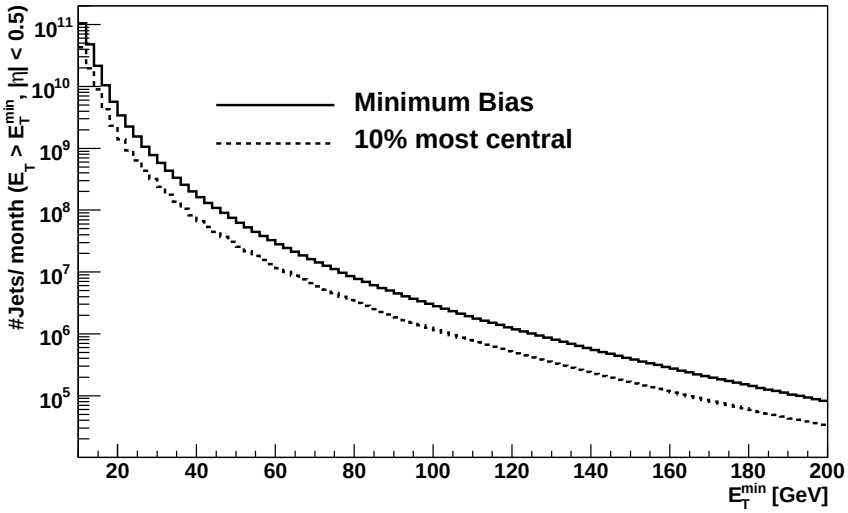

Figure 3.5: Number of jets with $E_T > E_T^{\min}$ and $|\eta| < 0.5$ produced in $Pb+Pb$ collisions at $\sqrt{s_{\mathrm{NN}}} = 5.5\,\mathrm{TeV}$ in one effective month of running (10^6 s). The minimum bias rate (solid line) is compared to the rate in the 10% most central collisions (dashed line).

$E_T^{\min}[\mathrm{GeV}]$	TPC fiducial region	EMCal fiducial region
20	2.0×10^9	2.4×10^8
50	4.8×10^7	5.8×10^6
100	2.6×10^6	3.1×10^5
150	4.0×10^5	4.8×10^4
200	1.0×10^5	1.2×10^4
250	2.5×10^4	3.0×10^3

Table 3.3: Number of jets with $E_T > E_T^{\min}$ produced in one month of $Pb+Pb$ running within the central barrel ($|\eta| < 0.5$) and within the EMCAL acceptance ($|\eta| < 0.3$ and $83^\circ < \varphi < 157^\circ$). The acceptance limits assume that a cone size of $R_{\mathrm{c}} = 0.4$ is used for jet reconstruction.

Chapter 4

Framework of the ALICE detector: AliROOT

In high energy physics, a framework is a set of software tools that enables data processing. The role of the framework is shown in figure 4.1.

The primary interactions are simulated via event generators, and the resulting kinematic tree is then used in the transport package. An event generator produces set of "particles" with their momenta. The set of particles, where one maintains the production history (in form of mother-daughter relationship and production vertex), forms the kinematic tree. The transport package transports the particles through the set of detectors, and produces hits, *i.e.,* energy deposition at a given point. The hits contain also information ("track labels") about the particles that have generated them.

At the next step, the detector response is taken into account, and the hits are transformed into digits. As mentioned previously, the hits are closely related to the tracks that generated them. The transition from hits/tracks to digits/detectors is marked on the picture as "disintegrated response", the tracks are "disintegrated" and only the labels carry the `Monte-Carlo` information.

There are two types of digits: "summable digits", where one uses low thresholds and the result is additive, and "digits", where the real thresholds are used, and the result is similar to what one would get in the real data taking. In some sense the "summable digits" are precursors of the "digits". The noise simulation is activated when "digits" are produced.

The summable digits are used for the so-called "event merging", where a signal event is embedded in a signal-free underlying event. This technique is widely used in heavy-ion physics and allows reusing the underlying events with substantial economy of computing resources. Optionally, it is possible to perform the conversion digits to raw data which is used to estimate the expected data size, to evaluate the high level trigger algorithms and to carry on the so called computing data challenges. The reconstruction and the HLT algorithms can both work with digits and with raw

data.

After the creation of digits, the reconstruction and analysis chains can be activated to evaluate the software and the detector performance, and to study some particular signatures. The reconstruction takes as input digits or raw data, real or simulated [13].

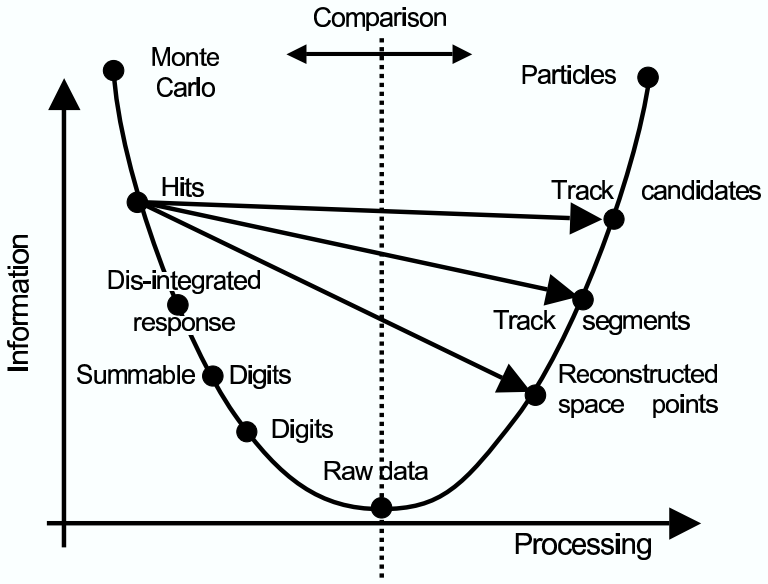

Figure 4.1: Data processing framework.

4.1. Simulation framework

The simulation framework covers the simulation of primary collisions and generation of the emerging particles, the transport of particles through the detector, the simulation of energy depositions (hits) in the detector components, their response in form of so called summable digits, the generation of digits from summable digits with the optional merging of underlying events and the creation of raw data.

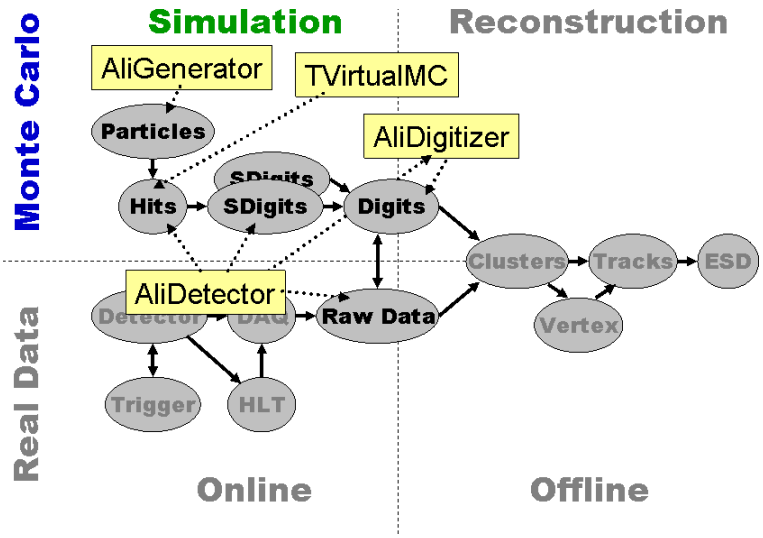

Figure 4.2: Simulation framework.

Generation of Particles

Different generators can be used to produce particles emerging from the collision. The class `AliGenerator` is the base class defining the virtual interface to the generator programs.

Virtual Monte Carlo

A class derived from `TVirtualMC` performs the simulation of particles traversing the detector components. The `Virtual Monte-Carlo` also provides an interface to construct the geometry of detectors. The geometrical modeller `TGeo` does the task of the geometry description. The concrete implementation of the `Virtual Monte-Carlo` application `TVirtualMCApplication` is `AliMC`. The `Monte-Carlo` used in ALICE are GEANT.3.21 [42].

Modules and Detectors

A class derived from `AliModule` describes each module of the ALICE detector. Classes for active modules (*i.e.,* detectors) are not derived directly from `AliModule` but from its subclass `AliDetector`. These base classes define the interface to the simulation framework via a set of virtual methods.

Configuration File (Config.C)

The configuration file is a C++ macro that is processed before the simulation starts. It creates and configures the `Monte-Carlo` object, the generator object, the magnetic field map and the detector modules.

Detector Geometry

The `Virtual Monte-Carlo` application creates and initializes the geometry of the detector modules by calling the virtual functions `CreateMaterials`, `CreateGeometry`, `Init` and `BuildGeometry`.

Vertexes and Particles

In case the simulated event is intended to be merged with an underlying event, the primary vertex is taken from the file containing the underlying event by using the vertex generator `AliVertexGenFile`. Otherwise, the primary vertex is generated according to the generator settings. Then the particles emerging from the collision are generated and put on the stack (an instance of `AliStack`). The `Monte-Carlo` object performs the transport of particles through the detector. The external decayer `AliDecayerPythia` usually handles the decay of particles.

Hits and Track References

The `Monte-Carlo` simulates the transport of a particle step by step. After each step the virtual method `StepManager` of the module in which the particle currently is located is called. In this `StepManager` method, calling `AddHit` creates the hits in the detector. Optionally also track references (location and momentum of simulated particles at selected places) can be created by calling `AddTackReference`. `AddHit` has to be implemented by each detector whereas `AddTackReference` is already implemented in `AliModule`. The detector class manages the container and the branch for the hits and for the (summable) digits via a set of so-called loaders. The relevant data members and methods are `fHits`, `fDigits`, `ResetHits`, `ResetSDigits`, `ResetDigits`, `MakeBranch` and `SetTreeAddress`. For each detector methods like `PreTrack`, `PostTrack`, `FinishPrimary`, `FinishEvent` and `FinishRun` are called during the simulation when the conditions indicated by the method names are fulfilled.

Summable Digits

Calling the virtual method `Hits2SDigits` of a detector creates summable digits. This method loops over all events, creates the summable digits from hits and stores them in the digits files.

Digitization and Merging

Dedicated classes derived from `AliDigitizer` are used for the conversion of summable digits into digits. Since `AliDigitizer` is a `TTask`, this conversion is done for the current event by the `Exec` method. Inside this method the summable digits of all input streams have to be added, combined with noise, converted to digital values taking into account possible thresholds, and stored in the digits container. An object of type `AliRunDigitizer` manages the input streams (more than one in case of merging) as well as the output stream. The methods `GetNinputs`, `GetInputFolderName` and `GetOutputFolderName` return the relevant information. The run digitizer is accessible inside the digitizer via the protected data member `fManager`. If the flag `fRegionOfInterest` is set, only detector parts where summable digits from the signal event are present should be digitized. When `Monte-Carlo` labels are assigned to digits, the stream-dependent offset given by the method `GetMask` is added to the label of the summable digit. The detector specific digitizer object is created in the virtual method `CreateDigitizer` of the concrete detector class. The run digitizer object is used to construct the detector digitizer. The `Init` method of each digitizer is called before the loop over the events is started. A direct conversion from hits directly to digits can be implemented in the method `Hits2Digits` of a detector. The loop over the events takes place inside the method. Of course merging is not supported in this case.

4.1.1. Parametrized generation

The event generation based on parametrization can be used to produce signal-free final states. It avoids the dependences on a specific model, and is efficient and flexible. It can be used to study the track reconstruction efficiency as a function of the initial multiplicity and occupation.

In many cases, the expected transverse momentum and rapidity distributions of particles are known. In other cases, the effect of variations in these distributions must be investigated. In both situations, it is appropriate to use generators that produce primary particles and their decays sampling from parametrized spectra. To meet the different physics requirements in a modular way, the parametrizations are stored in independent function libraries wrapped into classes that can be plugged into the generator.

It is customary in heavy-ion event generation to superimpose different signals on an event in order to tune the reconstruction algorithms. This is possible in ALIROOT the so-called `cocktail generator`. This creates events from user-defined particle cocktails by choosing as ingredients a list of particle generators.

Several event generators are available via the ROOT class [43] that implements the

generic generator interface, TGenerator. By means of implementations of this abstract base class, we wrap `Fortran Monte-Carlo` codes like PYTHIA [9] and HIJING [10] that are thus accessible from the ALIROOT classes. In particular the interface to PYTHIA includes the use of nuclear structure functions of LHAPDF.

PYTHIA 6

PYTHIA is used for simulation of $p+p$ interactions and for generation of jets in case of event merging. For more details see section 5

HIJING

HIJING (Heavy-Ion Jet Interaction Generator) combines a QCD-inspired model of jet production using the Lund model for jet fragmentation. Hard or semi-hard parton scatterings with transverse momenta of a few GeV are expected to dominate high-energy heavy-ion collisions. The HIJING model has been developed with special emphasis on the role of mini jets in $p+p$, $p+A$ and $Au+Au$ reactions at collider energies.

4.1.2. Reconstruction Framework

The global ALICE coordinate is a right-handed coordinate system with the z-axis coinciding with the beam-pipe axis pointing away from the muon arm, the y-axis going upward, and its origin defined by the intersection point of the z-axis and the central membrane-plane of TPC

We briefly summarize the main conceptual terms of the reconstruction framework (see also section 3.2):

- **Digit:** This is a digitized signal (ADC count) obtained by a sensitive pad of a detector at a certain time.
- **Cluster:** This is a set of adjacent (in space and/or in time) digits that were presumably generated by the same particle crossing the sensitive element of a detector.
- **Space point (reconstructed):** This is the estimation of the position where a particle crossed the sensitive element of a detector (often, this is done by calculating the centre of gravity of the 'cluster').
- **Track (reconstructed):** This is a set of five parameters (such as the curvature and the angles with respect to the coordinate axes) of the particle's trajectory together with the corresponding covariance matrix estimated at a given point in space.

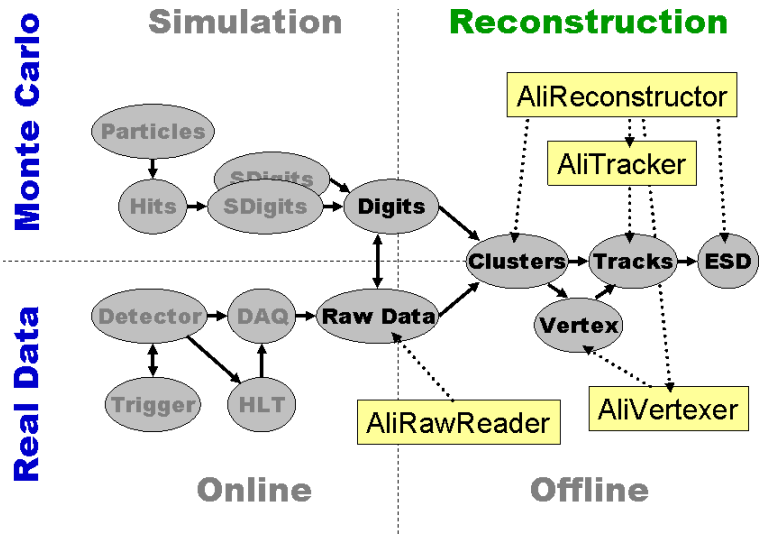

Figure 4.3: Reconstruction framework.

If the input data is provided in format of ROOT trees, either the loaders or directly the trees are used to access the digits. In case of raw data input, the digits are accessed via a raw reader. If a galice.root file exists, the run loader will be retrieved from it. Otherwise the run loader and the headers will be created from the raw data. The reconstruction cannot work if there is no galice.root file and no raw data input.

The clusters (rec. points) are considered intermediate output and are stored in ROOT trees handled by the loaders. The final output of the reconstruction is a tree with objects of type `AliESD` stored in the file `AliESDs.root`. This Event Summary Data (ESD) contains lists of reconstructed tracks/particles and global event properties.

The first step of the reconstruction is the so-called ”local reconstruction”. It is executed for each detector separately and without exchanging information with other detectors. Usually the clusterization is done in this step.

The reconstruction of the primary-vertex position in ALICEis done using the information provided by the silicon pixel detectors, which constitute the two innermost layers of the ITS.

The combined track reconstruction tries to accumulate the information from different detectors in order to optimize the track reconstruction performance. The result of this is stored in the combined track objects. This is achieved by using just integer indexes pointing to the specific track objects, which on the other hand makes it possible to retrieve the full information if needed. The list of combined tracks can

be kept in memory and passed from one reconstruction module to another. The storage of the combined tracks should be done in the standard way.

After the tracks have been reconstructed and stored in the AliESD object, further information is added to the ESD. For each detector the method FillESD of the reconstructor is called. Inside this method e.g. V0s are reconstructed or particles are identified (PID). For the PID, a Bayesian approach is used.

4.1.3. Event summary data

The classes that are needed to process and analyze the ESD are packaged in a standalone library (libESD.so) which can be used independently from the ALIROOT framework. Inside each ESD object, the data is stored in polymorphic containers filled with reconstructed tracks, neutral particles, etc. The main class is AliESD, which contains all the information needed during the physics analysis:

- fields to identify the event, such as event number, run number, time stamp, type of event, trigger type (mask), trigger cluster (mask), version of reconstruction, etc.;
- reconstructed ZDC energies and number of participants;
- primary vertex information: vertex z-position estimated by the T0, primary vertex estimated by the SPD, primary vertex estimated using ESD tracks;
- tracklet multiplicity;
- interaction time estimated by the T0 together with additional time and amplitude information from T0;
- array of ESDtracks;
- arrays of HLT tracks, both from the conformal mapping and from the Hough transform reconstruction;
- array of MUON tracks;
- array of PMD tracks;
- array of TRD ESDtracks (triggered);
- arrays of reconstructed V0 vertexes, cascade decays and kinks;
- array of calorimeter clusters for PHOS/EMCAL; indexes of the information from PHOS and EMCAL detectors in the array above.

4.1.4. Analysis

The analysis of experimental data is the final stage of event processing. The Physics Board coordinates data analysis via the Physics Working Groups (PWGS). At present, the following PWG have started their activity

- PWG0 first physics
- PWG1 detector performance
- PWG2 global event characteristics: particle multiplicity, centrality, energy density, nuclear stopping; soft physics: chemical composition (particle and resonance production, particle ratios and spectra, strangeness enhancement), reaction dynamics (transverse and elliptic flow, HBT correlations, eventbyevent dynamical fluctuations)
- PWG3 heavy flavors: quarkonia, open charm and beauty production
- PWG4 hard probes: jets, direct photons

In the ALICE Computing Model the analysis starts from the Event Summary Data (ESD). These are produced during the reconstruction step and contain all the information for the analysis. The size of the ESD is about one order of magnitude lower than the corresponding raw data. The analysis tasks produce Analysis Object Data (AOD) specific to a given set of physics objectives. Further passes for the specific analysis activity can be performed on the AODS, until the selection parameter or algorithms are changed.

A typical data analysis task usually requires processing of selected sets of events. The selection is based on the event topology and characteristics, and is done by querying the tag database. The tags represent physics quantities which characterize each run and event, and permit fast selection. They are created after the reconstruction and contain also the unique identifier of the ESD file.

The next step of a typical analysis consists of a loop over all the events in the list and calculation of the physics quantities of interest. Usually, for each event, there is a set of embedded loops on the reconstructed entities such as tracks, V^0 candidates, neutral clusters, etc., the main goal of which is to select the signal candidates. Inside each loop a number of criteria (cuts) are applied to reject the background combinations and to select the signal ones. The cuts can be based on geometrical quantities such as impact parameters of the tracks with respect to the primary vertex, distance between the cluster and the closest track, distance of closest approach between the tracks, angle between the momentum vector of the particle combination and the line connecting the production and decay vertexes. They can also be based on

kinematics quantities such as momentum ratios, minimal and maximal transverse momentum, angles in the rest frame of the combination. Particle identification criteria are also among the most common selection criteria.

The optimization of the selection criteria is one of the most important parts of the analysis. The goal is to maximize the signal-to-background ratio in case of search tasks, or another ratio (typically $\mathrm{Signal}/\sqrt{\mathrm{Signal}+\mathrm{Background}}$) in case of measurement of a given property. Usually, this optimization is performed using simulated events where the information from the particle generator is available.

After the optimization of the selection criteria, one has to take into account the combined acceptance of the detector. This is a complex, analysis-specific quantity which depends on the geometrical acceptance, the trigger efficiency, the decays of particles, the reconstruction efficiency, the efficiency of the particle identification and of the selection cuts. The components of the combined acceptance are usually parametrized and their product is used to unfold the experimental distributions or during the simulation of some model parameters.

The last part of the analysis usually involves quite complex mathematical treatments, and sophisticated statistical tools. Here one may include the correction for systematic effects, the estimation of statistical and systematic errors, etc.

The AOD files generated during the scheduled analysis can be used by several subsequent analyses, or by a class of related physics tasks.

The AOD analysis framework implements a set of tools like data readers, converters, cuts, and other utility classes. The design is based on two main requirements: flexibility and common AOD particle interface. This guarantees that several analyses can be done in sequence within the same computing session.

In order to fulfill the first requirement, the analysis is driven by the ‘analysis manager’ class and particular analyses are added to it. It performs the loop over events, which are delivered by an user-specified reader. This design allows the analyses to be ordered appropriately if some of them depend on the results of the others.

The cuts are designed to provide high flexibility and performance. A two-level architecture has been adopted for all the cuts (particle, pair and event). A class representing a cut has a list of ‘base cuts’. Each base cut implements a cut on a single property or performs a logical operation (and, or) on the result of other base cuts.

Chapter 5

Production of high-p_T events

The aim of this work is to study the effects of parton energy loss in a medium under extreme conditions of temperature and density. To achieve that, we simulated high-p_T events in $p+p$ collision, reconstructed jets with a jet finding algorithm and performed event shape analysis. $p+p$ collisions were used as a baseline and the jets energy loss was simulated using two afterburner `Monte-Carlo` models. Finally, modifications in jet structure due to energy loss, were studied.

The PYTHIA program is a standard tool for the generation of high-energy collisions, comprising a coherent set of physics models for the evolution from a few-body hard process to a complex multihadronic final state. It contains a library of hard processes and models for initial and final state parton showers, multiple parton-parton interactions, beam remnants, string fragmentation and particle decays, and it also has a set of utilities and interfaces to external programs. For a complete description of the physics content we refer to the PYTHIA manual [9].

We focus on high-p_T particle production with PYTHIA version 6.2.14 (packaged in ALIROOT) with *tune set A* [44] in $p+p$ mode at $\sqrt{s_{\rm NN}} = 5.5$ TeV. In table 5.1, we report the main list of parameters used for the generation of high-p_T events.

The particle production was done to improve the jets production selecting hard processes in PYTHIA. A calibration sample of a fixed p_T with p_T^{hard} = 50 GeV/c (dashed line in figure 5.1) and, to approach the real spectrum produced in ALICE, events with p_T^{hard} = 30 - 179 GeV/c (solid line in figure 5.1) was produced. The ratio of triggered to generated jets for a fixed interval of p_T^{hard} together with the corresponding hard cross section given by PYTHIA, determine the weight which we apply to every event (or jet event) generated for the particular interval. The weights are show in table 5.2.

Description	Parameter	Value
Process types QCD jets	MSEL	1
	ISUB (11)	$q_i q_j \to q_i q_j$
	ISUB (12)	$q_i \bar{q_i} \to q_k \bar{q_k}$
	ISUB (13)	$q_i \bar{q_i} \to gg$
	ISUB (28)	$q_i g \to q_i g$
	ISUB (53)	$gg \to q_k \bar{q_k}$
	ISUB (68)	$gg \to gg$
	ISUB (96)	semihard QCD $2 \to 2$
Minimum/maximum parton p_T^{hard} [GeV]	CKIN(3)	fPtHardMin
	CKIN(4)	fPtHardMax
		see Table 5.2
Initial/final state radiation on	MSTP(61)	1
	MSTP(71)	1
Intrinsic k_T from Gaussian (zero mean)	MSTP(91)	1
width σ [GeV]	PARP(91)	1
upper cut-off (at 5σ) [GeV]	PARP(93)	5
Cone jet finder (pycell)		
$\lvert\eta\rvert$ of the "detector"	PARU(51)	2
number of cells in η	MSTU(51)	274
number of cells in ϕ	MSTU(52)	432
threshold [GeV]	PARU(58)	0
seed [GeV]	PARU(52)	4
min E_T [GeV]	PARU(53)	5
radius	PARU(54)	1

Table 5.1: PYTHIA 6.2.14 parameter settings for the generation of jets in $p+p$ collisions at $\sqrt{s_{\rm NN}} = 5.5$ TeV

After event generation, jets were first reconstructed, at the final state particle level, with PYCELL routine[1] and subsequently we used a cone jet algorithm and event shape analysis, described in the next section, to study jets.

[1] PYCELL is the internal PYTHIA cone algorithm with $R_{\rm c}$ =1 which uses all simulated particles to reconstruct jets

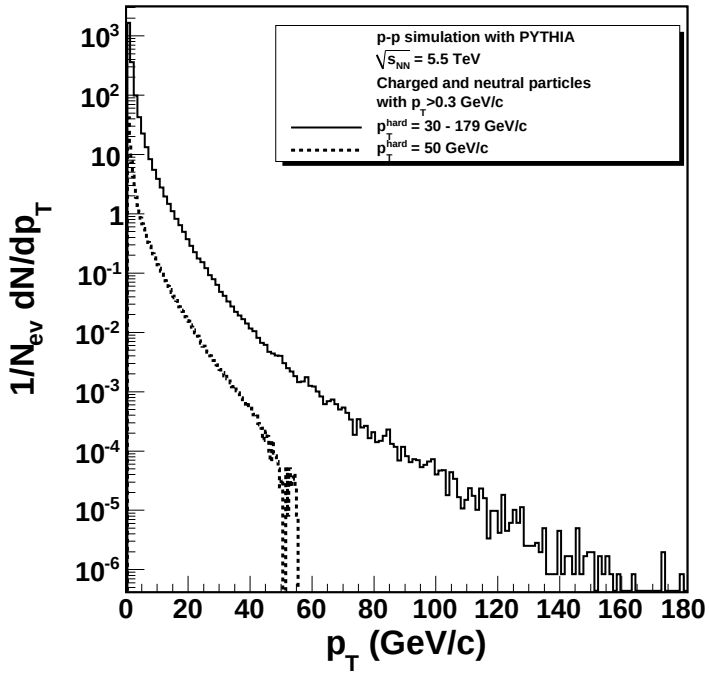

Figure 5.1: p_T distribution for charged and neutral particles produced in $p+p$ collisions at $\sqrt{s_{\rm NN}} = 5.5$ TeV with p_T^{hard} = 50 GeV/c (dashed line) and p_T^{hard} = 30 - 179 GeV/c (solid line) weighted with respect to the values of table 5.2.

Min. p_T^{hard} [GeV/c]	**Max. p_T^{hard}** [GeV/c]	**Weight**
30	35	$7.007 \cdot 10^{-4}$
35	42	$4.521 \cdot 10^{-4}$
42	50	$2.202 \cdot 10^{-4}$
50	60	$1.151 \cdot 10^{-4}$
60	72	$5.155 \cdot 10^{-5}$
72	86	$2.533 \cdot 10^{-5}$
86	104	$1.238 \cdot 10^{-5}$
104	124	$5.131 \cdot 10^{-6}$
124	149	$2.375 \cdot 10^{-6}$
149	179	$1.006 \cdot 10^{-6}$

Table 5.2: Values of the weight for each p_T^{hard}.

Chapter 6

Jet reconstruction

Jets have been studied for many years in the field of high energy physics at e^+e^- and hadron-hadron colliders. The measurement of jets cross sections, has provided useful tests of quantum chromodynamics.

Although the basic hard scattering processes studied in e^+e^- and hadron-hadron collisions are almost the same, the overall event structure is quite different. In the e^+e^- case the initial state is purely electromagnetic and the entire final state can be thought as arising from the short distance interaction of the virtual photon with the quarks. In this sense all of the hadrons in the final state are associated with the hard scattering process. In contrast the overall structure of the hadron-hadron case is more complex. Of the large number of initial state partons, more probably one "active parton" from each incident hadron participates in the hard scattering process. Thus only a fraction of hadrons in the final state are to be associated with the hard scattering process, with the remainder ascribed to the "underlying event." This second contribution corresponds to the soft interactions of the remaining partons in the incident hadrons and, in first approximation, can be treated as uncorrelated with the hard process. The active partons also produce additional radiation in the form of initial state bremsstrahlung that is not present in e^+e^- events. The underlying event plus the initial state radiation produce the characteristic "beam jets" of hadron collisions: particles with small momenta transverse to the beam axis, but possibly large momenta along the beam axis.

Due to the different event structures in the two cases, different jet definitions and algorithms to reconstruct them have been developed. The aim of both however, is to provide a mapping between the observed high-energy hadrons and the initial state energetic partons which were involved in the hard scattering.

In e^+e^- collisions is used a jet definition that associates every final-state hadron uniquely with one of the jets. In hadron-hadron collisions only a small fraction of the final state hadrons are associated with the high-p_T jets, the other particles present in

the event can be thought as associated with the underlying events. To keep the high-p_T jets distinct from the hadronic debris in the underlying events, a cone definition is used, which was inspired by the theoretical definition for jets in e^+e^- collisions.

A jet in this definition is a set of particles whose momentum vectors lie within a certain angular cone. In this kind of definition, one recursively groups sets of particles with "nearby" momenta, as defined by some measure, into larger sets of particles. The initial sets consist of just one particle, the final sets are jets [52].

6.1. The Cone Jet Algorithm

Jet algorithm, start from a list of particles that we take to be hadrons at the experimental level, and partons in a perturbative QCD calculation. The role of the algorithm is to associate clusters of these particles into jets such that the kinematic properties of the jets can be related to the corresponding properties of the energetic partons produced in the hard scattering process. Thus the jet algorithm allows us to study the partons in the hadronic final state.

Differences in the properties of reconstructed jets when going from the parton to the hadron: Each particle i carries a 4-momentum p_i^μ, the algorithm selects a set of particles which are typically emitted close to each other in angle and combines their momenta to form the momentum of a jet. The selection process is called the "jet algorithm" and the momentum addition rule is called the "recombination scheme". This two steps are distinct, for example, use one set of kinematic variables in the jet algorithm to determine the particles in a jet and then construct a separate set of kinematic variables to characterize the jets that have been identified.

For e^+e^- annihilation, one wants to emphasize rotational invariance. Thus the natural variables are energies E and polar angles θ, ϕ. For hadron-hadron collisions, one wants to emphasize invariance under boosts along the beam axis since, in fact, the center of mass frame of the hard scattering is typically moving in the hadron-hadron center of mass frame. Thus the natural variables are transverse momenta p_T or the corresponding transverse energy $E_T \equiv E\sin\theta$, azimuthal angle ϕ and pseudo-rapidity $\eta = -\ln(\tan(\theta/2))$.

Cone algorithms form jets by associating together particles which trajectories *i.e.,* towers whose centers lie within a circle of specific radius R in $\eta \times \phi$ space. This 2-dimensional space is natural in $p\overline{p}$ collisions where the dynamics is spread out in the longitudinal direction. Starting with a trial geometric center (or axis) for a cone in $\eta \times \phi$ space, the energy-weighted is calculated including contributions from all particles within the cone. This new point in $\eta \times \phi$ is then used as the center for a new trial cone. As this calculation is iterated the cone center "flows" until a "stable" solution is found, *i.e.,*, until the centroid of the energy depositions within the cone

is aligned with the geometrical axis of the cone. This leads us to our initial cone algorithm of scalar E_T-weighted centers. The particles are specified by massless 4-vectors $(E^i = |\mathbf{p}^i|, \mathbf{p}^i)$ with angles $\left(\phi^i, \theta^i, \eta^i = -\ln\left(\tan(\theta^i/2)\right)\right)$ given by the direction from the interaction point with unit vector $\hat{\mathbf{p}}^i = \mathbf{p}^i/E^i$. The scalar E_T for each particle is $E_T^i = E^i \sin(\theta^i)$. For a specified geometric center for the cone $\left(\eta^C, \phi^C\right)$ the particles i within the cone satisfy

$$i \subset C \quad : \quad \sqrt{(\eta^i - \eta^C)^2 + (\phi^i - \phi^C)^2} \leq R. \tag{6.1}$$

a "stable" cone satisfies the constraints

$$\eta^C = \frac{\sum_{i\subset C} E_T^i \eta^i}{E_T^C}, \quad \phi^C = \frac{\sum_{i\subset C} E_T^i \phi^i}{E_T^C} \tag{6.2}$$

i.e.,, the geometrical center of the previous equation is identical to the E_T-weighted centroid with

$$E_T^C = \sum_{i\subset C} E_T^i \, . \tag{6.3}$$

Naively we can simply identify these stable cones, and the particles inside, as jets, $J = C$.

To complete the jet finding process we require a recombination scheme. Using the stable cone variables:

$$E_T^J = \sum_{i\subset J=C} E_T^i = E_T^C \, , \tag{6.4}$$

$$\eta^J = \frac{1}{E_T^J} \sum_{i\subset J=C} E_T^i \eta^i \, , \tag{6.5}$$

$$\phi^J = \frac{1}{E_T^J} \sum_{i\subset J=C} E_T^i \phi^i \, . \tag{6.6}$$

In practice, in order to save computing time, the iterative process of searching for the "stable" cones in experimental data starts with those cones centered about the most energetic particles in the event, the so-called "seeds".

Seed-based cone algorithm offer the advantage of being comparatively efficient in CPU time. In a typical application, detector towers are sorted according to descending E_T and only towers passing a seed cut,

$$E_T^{tower} > E_T^{seed} \ , \tag{6.7}$$

are used as starting points for the initial jet cones. This greatly reduces the number of cones that need to be evaluated in the initial stage. The seed threshold E_T^{seed} must be chosen low enough so that variations of E_T^{seed} lead to negligible variations in any observable under consideration.

In each seed cone, The E_T-weighted centroids are calculated for the particles and then the centroids are used as centers for new cones in $\eta \times \phi$ space. This procedure is iterated for each cone until the cone axis coincides with the centroid.

Figure 6.1 shows the flow chart representation of the cone algorithm used at the CDF experiment [53]. The choice of cone radius is based on the amount of jet energy contained within the cone and the radius which gives the best resolution. This optimization differs from experiment to experiment, for example, R_c = 1.0 was originally used at UA1 but smaller cone sizes of R_c = 0.4 and 0.7 have been used at CDF.

6.1.1. Cone Jet Algorithm for Heavy-Ion Collisions

Jet reconstruction in heavy ion collisions is affected by the bulk of soft and semi-hard particles. A cone jet algorithm implemented in the module JETAN of ALIROOT was used. This algorithm is based on a algorithm developed by the UA1collaboration [54] and further developed to account for the heavy-ion background.

The input to the algorithm is an energy grid in (η,ϕ) filled by a combination of transverse energy .

The algorithm consists of the following steps:

1. Initialize the estimated background level per grid cell $\hat{E}_T^{BG}$ to the average over all grid cells.
2. Sort cells in decreasing cell energy, E_T^i.
3. For at least 2 iterations, and until the change in $\hat{E}_T^{BG}$ between most recent successive iterations is smaller than a set threshold
   (a) Clear the jets list
   (b) Flag all cells outside a jet
   (c) Execute the jet-finding loop for each cell, starting with the largest:
      i. If $E_T^i - \hat{E}_T^{BG} > E_T^{seed}$, where E_T^{seed} is a chosen threshold cell energy, and the cell is flagged as not in a jet, treat it as a jet seed candidate:

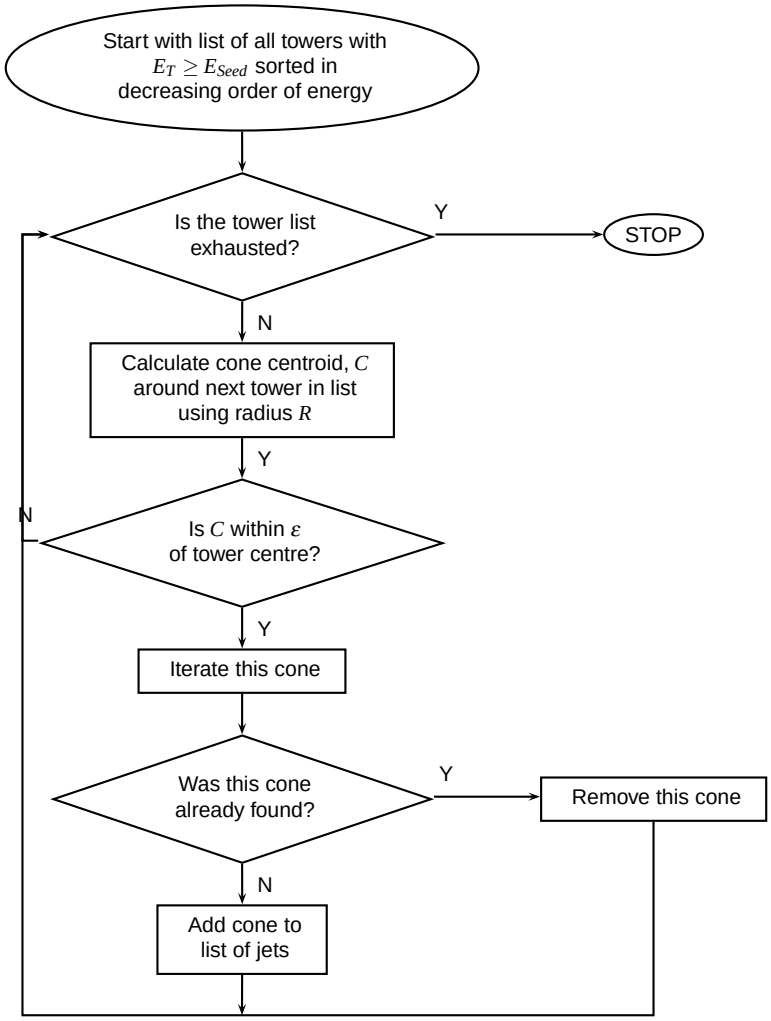

Figure 6.1: Cone jet algorithm used at the Tevatron at Fermilab, from [53]

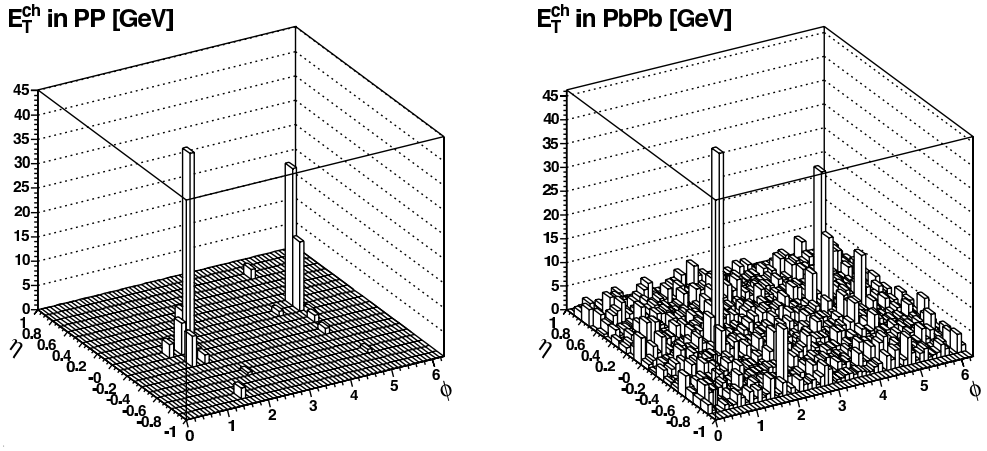

Figure 6.2: Charged jets in the η-ϕ plane for a 100 GeV jet in $p+p$ (left) and for the same jet embedded in a central $Pb+Pb$ event (right). In both cases a particle p_T^{cut} of 0.5 GeV has been applied [55]

A. Set jet centroid (η^C, ϕ^C) to the co-ordinates of the jet seed cell η_i, ϕ_i.

B. Using all cells within $\sqrt{(\eta^i-\eta^C)^2+(\phi^i-\phi^C)^2} < R$ of the initial centroid, calculate the new energy-weighted ($E_T^i - \hat{E}_T^{BG}$) centroid. Set the new energy-weighted centroid to be the new initial centroid. Repeat centroid calculation iterations until the centroid does not shift by more than one cell in subsequent iterations.

C. Store centroid as jet candidate and flag all cells within R of centroid as inside a jet.

(d) Re-calculate the estimated background energy $\hat{E}_T^{BG}$

(e) For each jet candidate, calculate the energy by summing the energies of the cells in the cone and subtracting the background. If the jet energy is greater than E_T^C, the minimum allowed cone energy, a jet is found.

Full event simulation performed within the ALIROOT framework, chose HIJING for the generation of background events, in which PYTHIA events containing jet signals are merged. The mixed event contains all particles of the signal and as well of the background event, both, above a p_T^{cut} and within the central ALICE acceptance of $|\eta| < 0.9$ [16]. The initial tower configuration of the cone finder is illustrated in figure 6.2 for a 100 GeV jet. As the signal sticks out of the background it is possible to do the analysis only with the jet signal, without taking into account the background.

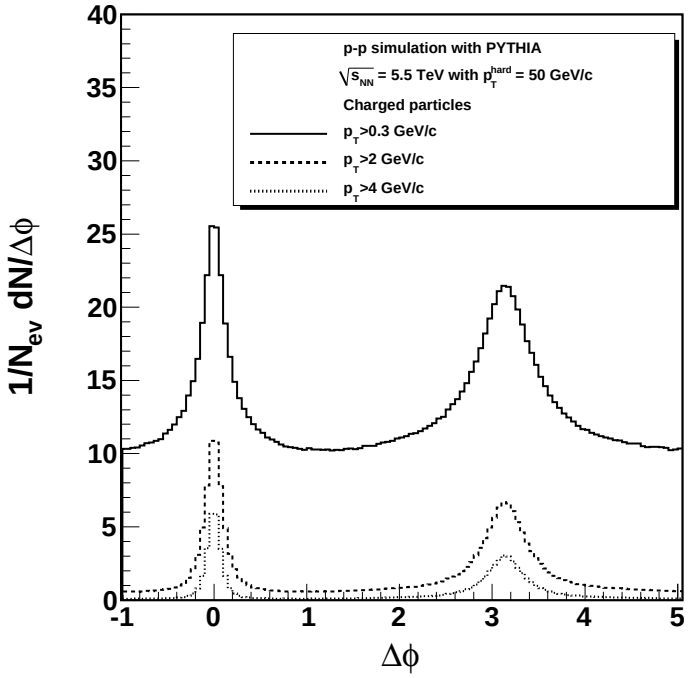

Figure 6.3: Dihadron azimuthal correlation at $\sqrt{s_{\rm NN}} = 5.5$ TeV and p_T^{hard} = 50 GeV/c $p_T^{cut}>$ 0.3 GeV/c (solid line), $p_T^{cut}>$ 2 GeV/c (dashed line) and $p_T^{cut}>$ 4 GeV/c (dotted line)

Choice of the alghorithm parameters

In order to select only hard processes a cut in p_T was done. We choose this cut studying azimuthal correlations between particles.

Two scattered partons propagate nearly back-to-back in azimuth from the collision point and fragment into jet-like spray of final state particles. The back-to-back azimuthal correlations of high p_T hadrons is written as

$$C(\Delta\Phi) = \frac{1}{N_{trigger}} \int d\Delta\eta \frac{dN}{d\Delta\Phi d\Delta\eta} \tag{6.8}$$

where $\Delta\phi$ and $\Delta\eta$ are, respectively, the azimuthal angle and pseudo-rapidity between a trigger and their associated particles.

Figure 6.3 shows the azimuthal correlation between particles with p_T^{hard} = 50 GeV/c . If the transverse momentum $p_T >$ 0.3 GeV/c a huge amount of particles with low

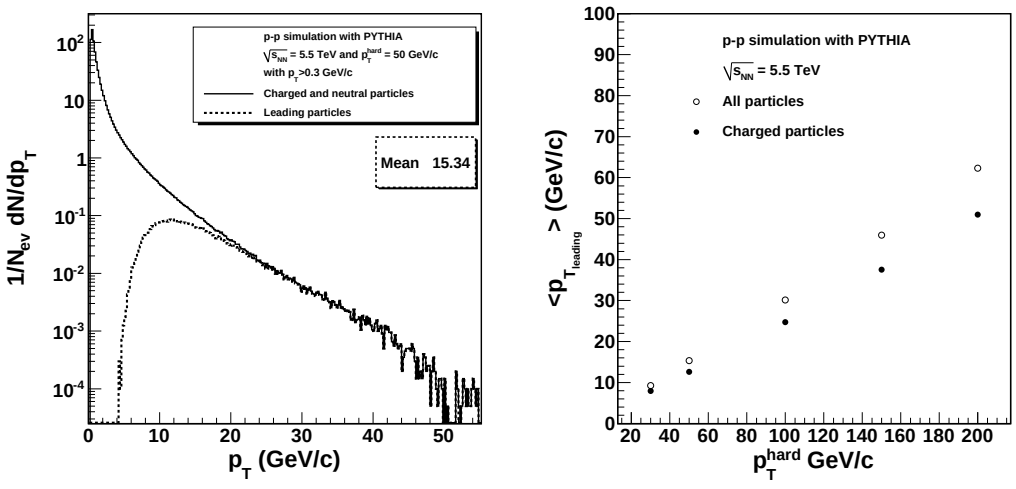

Figure 6.4: p_T distribution for neutral and charged particles produced in $p+p$ collisions at $\sqrt{s_{\rm NN}} = 5.5$ TeV and p_T^{hard} = 50 GeV/c. The solid line shows p_T distribution for all particles per event and the dashed line shows the p_T distribution for leading particles only. The right panel show the mean $p_{T\rm leading}$ per bin for all and charged particles production in $p+p$ collisions at $\sqrt{s_{\rm NN}} = 5.5$ TeV

p_T are present between the the two-peaks (solid line), this particles are considered like background. With a higher p_T^{cut} this background is reduced (dashes and dotted-dashed lines). A p_T^{cut} = 2 GeV/c was chosen for further work.

The seed energy of the threshold is the transverse momentum of the leading (or trigger) particles *i.e.,* the particles with highest momentum in each event. This 'seed energy' depends of the p_T^{hard} used in the simulation of hard processes. For example, figure 6.4 (left) shows the p_T distribution for neutral and charged particles simulated for a p_T^{hard} bin of 50 GeV/c. The mean p_T of leading particles is about $\sim$15 GeV/c (dashed line), the initial interaction in cone jet algorithm will be p_T^{seed} = 15 GeV/c and the same procedure for different bin. Figure 6.4 (right) and table 6.1 show the behaviour of mean $p_T^{leading}$, with increase in p_T^{hard}.

The size of the cones used to identify jets were: $R_{\rm c}$ = 0.4, 0.7 and 1. Other parameters used for jet cone algorithm are shown in table 6.2. Once defined the cone algorithm parameters, jets were reconstructed. Only jets obtained for p_T^{hard} = 50 GeV/c and p_T^{hard} = 30 - 179 GeV/c with charged particles and p_T^{cut} = 2 GeV/c are shown, but the results are the same for all particles and different p_T^{hard}. Studies in jets in the CDF experiment [53], show that almost all the energy of the jet is contained in $R_{\rm c}$ = 0.4, the ideal case is $R_{\rm c}$ =1, where all the particles are inside the cone and $R_{\rm c}$ = 0.7 is a middle case.

p_T^{hard} [GeV/c]	$p_{T_{leading}}$ **All** [GeV/c]	$p_{T_{leading}}$ **Chg** [GeV/c]
30	9.32	7.99
50	15.34	12.69
100	30.37	24.95
150	46.10	37.74
200	61.98	50.84
30-179	12.69	10.52

Table 6.1: Mean $p_{T\text{leading}}$ per bin for all and charged particles production in $p+p$ collisions at $\sqrt{s_{\text{NN}}} = 5.5$ TeV

Description	Value
Minimum seed energy [GeV]	see Table 6.1 0.0
Particle p_T^{cut} [GeV/c]	2
Radii R	0.4, 0.7,1
Maximum iterations	100
Minimum jet energy [GeV]	5.0
Size in ϕ	0.05
Size in η	0.05

Table 6.2: The settings used for cone jet algorithm implemented in the module JETAN of ALIROOT.

Figure 6.5 shows the mean E_T vs R_{c} for jets simulated with p_T^{hard} = 50 GeV/c and p_T^{hard} = 30 - 179 GeV/c . Only small differences are observed when changing the cone radius.

6.2. Events with dijets

Azimuthal correlation between dijets are shown in figures 6.6 for p_T^{hard} = 50 GeV/c (top left), p_T^{hard} = 150 GeV/c (top right) and p_T^{hard} = 30 - 179 GeV/c (bottom). Here the back-to-back azimuthal correlations is written as $\Delta\phi = \Phi_{E_{max}} - \Phi_{E_{min}}$, where max/min are the jets with maximum/minimum energy in the same event. We can see that there exist fake jets reconstructed close to the jet with maximum energy, these jets disappear when the energy of the jets increases since the jets are more collimated (top), but this fakes jets are more numerous when the cone size is small. For R_{c} = 0.4 there are fakes jets reconstructed at $\Delta\phi$ = 0.5 and $\Delta\phi$ = 5.5 due to part of the energy of the jet is not inside the cone. These fakes jets are less when the cone size is

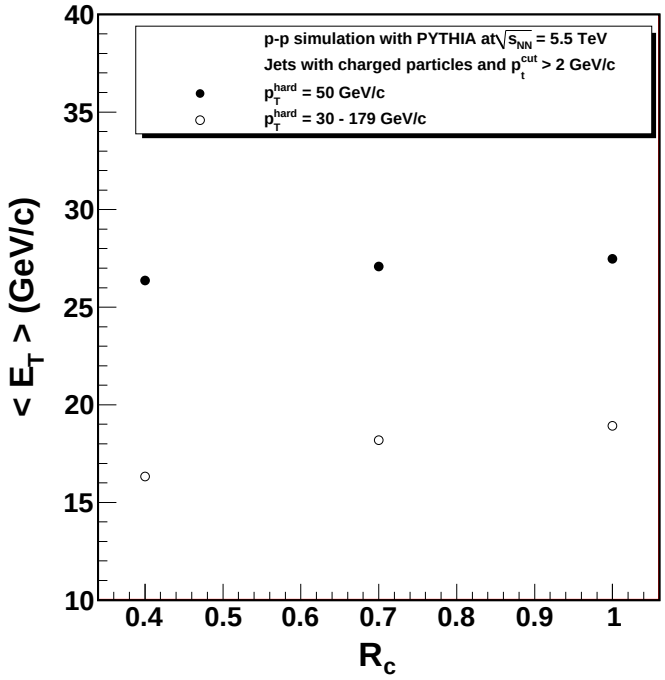

Figure 6.5: E_T jets vs R_c for charged particles with $p_T^{cut} > 2$ GeV/c, p_T^{hard} = 50 GeV/c (solid circles) and p_T^{hard} = 30 - 179 GeV/c (open circles).

increasing to an ideal case with R_c = 1. This effect is bigger in the spectrum with all the p_T^{hard} bins together (bottom).

One way to select only real dijets that are opposite in azimuthal angle and with small difference in energy, is defining an interval in $\Delta\phi$ of 2.8 $rad < \Delta\phi <$ 3.4 rad and $E_{T,max} - E_{T,min}/E_{T,max} <$ 0.3 for dijets with all particles and $E_{T,max} - E_{T_{min}}/E_{T,max} <$ 0.8 for dijets with charged particles, where max/min are the jets with maximum/minimum energy in the same event.

Another way to select real jets is using event shape analysis.

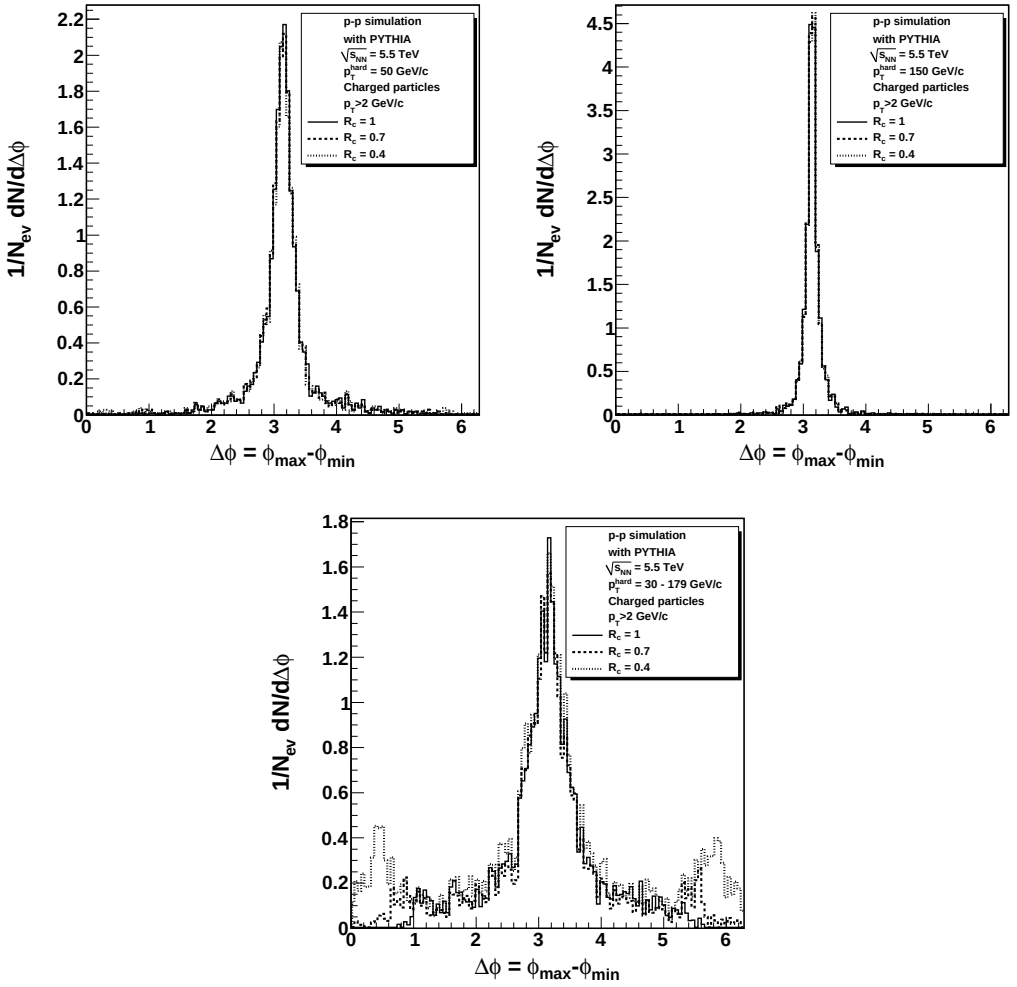

Figure 6.6: Dijet azimuthal correlations for charged particles with $p_T^{cut} > 2$ GeV/c, p_T^{hard} = 50 GeV/c (top left), p_T^{hard} = 150 GeV/c (top right) and p_T^{hard} = 30 - 179 GeV/c (bottom) for three cone radius: R_c = 1 (solid line), R_c = 0.7 (dashed line) and R_c = 0.4 (dotted line).

6.3. Event Shape Analysis (ESA)

The event shape analysis measures the geometrical properties of the energy flow in QCD states, its allows us a method to determine areas where one does encounter special topologies of jets in an event.

Sphericity was used at SLAC to show the evidence for the existence of jets in the annihilation process: e^+e^- at energies up to 7.4 GeV in the center of mass. They calculated in each event that direction which minimizes the sum of square of transverse momentum, calling this quantity the sphericity S. Sphericity approaches 0 for events with correlated transverse momenta and approaches to 1 for events with large multiplicity and isotropic particles distribution [56]. In hadron collisions, the contribution of underlying event and multiple interactions introduce an experimental difficulty not present in lepton colliders.

In this work, three shape variables are used to describe the topology of the events in hadron collisions: thrust (T), recoil (R) and thrust-minor (T_{min}), these variables are defined over particles within the acceptance of the detector [14].

6.3.1. Event shape variables

The thrust variable (T) is defined using only transverse variables:

$$T \equiv \underbrace{max}_{\overrightarrow{n}_t} \frac{\sum_i |\overrightarrow{p}_{t,i} \cdot \overrightarrow{n}_t|}{\sum_i |\overrightarrow{p}_{t,i}|} \tag{6.9}$$

where the sum runs over all particles in the final state within the acceptance, $\overrightarrow{p}_{t,i}$ represent the momentum components transverse to the beam and $\overrightarrow{n}_t$ is the transverse vector that maximizes the ratio. It is common to find the definition:

$$\tau \equiv 1 - T \sim S \tag{6.10}$$

related with the sphericity S of the event. The range of τ is between 0 and 0.35 [15]. For events with narrow back-to-back jets, τ is close to 0 and for events with a uniform distribution of momenta τ is close to 0.35

The recoil variable R is defined as the vector sum of the transverse momentum:

$$R \equiv \frac{1}{\sum_i |\overrightarrow{p}_{t,i}|} |\sum_i \overrightarrow{p}_{t,i}| \tag{6.11}$$

This quantity measures the balance of momenta of the event. For example for mono-jets events, *i.e.,* two jets in a event but only one of them inside detector acceptance, R tends to 1, because there are no vectorial transverse momentum cancellations between particles. Otherwise, in the case of narrow back-to-back jet inside the acceptance, R tends to 0 because the vectorial transverse momentum sum is 0.

T_{min} is a measure of the momentum out of the plane. Given the thrust axis ($\overrightarrow{n}_t$), we can define it as:

$$T_{min} \equiv \frac{\sum_i |\overrightarrow{p}_{t,i} \; x \; \overrightarrow{n}_t|}{\sum_i |\overrightarrow{p}_{t,i}|} \tag{6.12}$$

The event shape analysis starts by plotting a two dimensional distribution ("thrust map"), with τ $(1-T)$ in the horizontal axis and R in the vertical axis. This plot allows to identify different classes of events according with their location in the thrust map.

Figure 6.7 shows the two-dimensional distribution R vs. $1-T$ obtained using PYTHIA with minimum bias $p+p$ collisions at $\sqrt{s_{\mathrm{NN}}} = 200$ GeV in the simulation, we require that all particles be charged primaries and within the pseudorapidity range of $|\eta| \leq 1$. We also require that the events have at least 3 particles with transverse momentum satisfying $|\overrightarrow{p}_{\perp,i}| \geq 0.8$ GeV/c.

Region A is characterized by dijets events, which occur completely inside the ALICE acceptance ($|\eta| \leq 1$), in this case, we have in the transverse plane the thrust axis ($\overrightarrow{n}_t$) almost collinear to the direction of the leading particle. So, the ratio defined in equation 6.9 tends to 1 and the recoil term (equation 6.11) tends to 0.

Region B is populated by monojets. These events have small values of τ and due to the absence of vectorial cancellations in the numerator of the recoil term will have the biggest values R.

Region C have the most isotropic events (with high $1-T$ and small R). This zone of the thrust map is characterized by the presence of three jet events, called "mercedes" events.

The intermediate region between A and B is populated by the combination of mono-jets and "incomplete dijets". Dijets are incomplete due to their high R, many particles are outside of the acceptance.

The intermediate region between B and C is populated by events were 3 or more jets are emitted at small angles with respect to the direction of the leading jet.

The line which appears in the high R part of the map is due to the definition of the variables. For example, suppose that we have one event with a certain thrust axis $\overrightarrow{n}_{t0}$, and in the event there are N particles. If the vectorial transverse momentum of

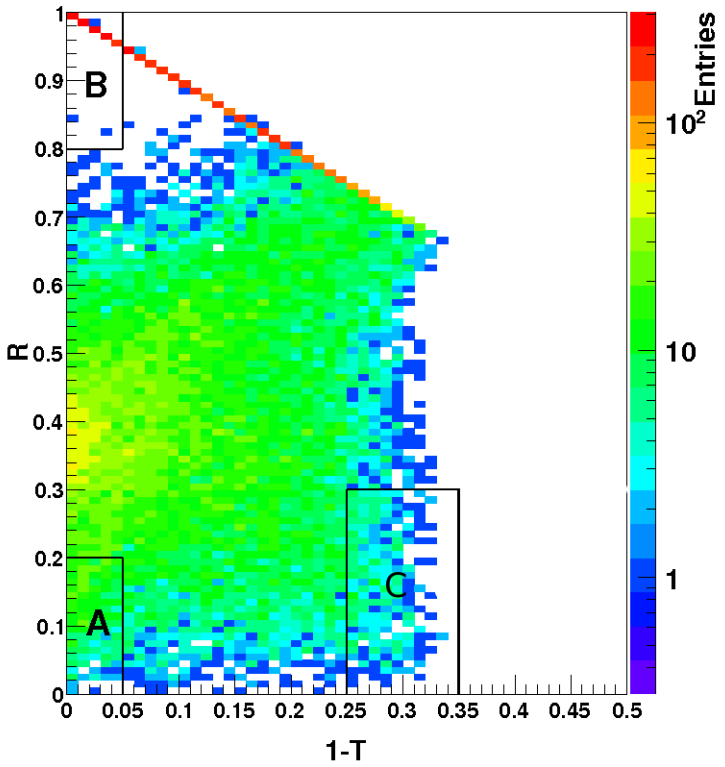

Figure 6.7: R vs $1-T$ for a minimum bias sample of $p+p$ collisions at $\sqrt{s_{\mathrm{NN}}} = 200$ GeV [14]

the particle i is $\overrightarrow{p}_{t,i}$, then from the definitions of R and T:

$$1-T+R = 1-\frac{\sum_i |\overrightarrow{p}_{t,i}\cdot\overrightarrow{n}_{t0}|}{\sum_i |\overrightarrow{p}_{t,i}|}+\frac{|\sum_i \overrightarrow{p}_{ti}|}{\sum_i |\overrightarrow{p}_{t,i}|} \tag{6.13}$$

Now, we use the fact that:

$$|\sum_i \overrightarrow{p}_{ti}| \leq \sum_i |\overrightarrow{p}_{t,i}| \tag{6.14}$$

Then:

$$1-T+R \leq 1-T+1 \tag{6.15}$$

The maximum value which T can reach is 1, so we find the following restriction:

$$1 - T + R \leq 1 \tag{6.16}$$

6.3.2. Azimuthal correlations

For describing the topology of the events we performed an analysis of the azimuthal correlation between particles using PYTHIA with minimum bias $p+p$ collisions at $\sqrt{s_{\mathrm{NN}}} = 200$ GeV. The distribution were obtained from the three regions (see table 6.3) which are generated by choosing the highest momentum particle in the event to be at 0 radians. This is shown in the left panel of figure 6.8, where the near side peaks are well distinguishable for the 3 plots while substantial differences occur in the away-side. For particles in region (A) we find the usual form of the away-side peak. For particles in region (B), as expected, there is no sight of a peak in the away-side. Finally for particles in region (C) we are confronted with a double hump structure [57], discussed in section 9.

Region	Kind of event	Variables
A	Dijets	$R \leq 0.35$, $\tau \leq 0.03$
B	Monojets	$R \geq 0.9$, $\tau \leq 0.03$
C	Mercedes	$R \leq 0.4$, $\tau \geq 0.25$

Table 6.3: 1-T and R parameters used for the present analysis.

Adding the three regions (solid line in the right panel of figure 6.8) we compare the azimuthal distribution with STAR data [8], we obtain a reasonable agreement.

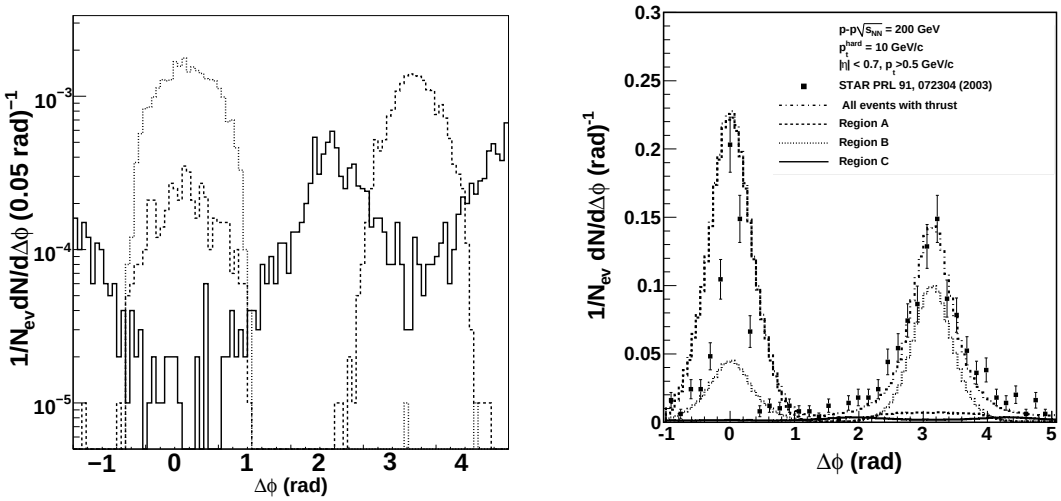

Figure 6.8: Dihadron azimuthal correlations for minimum bias $p+p$ collisions at $\sqrt{s_{\rm NN}} = 200$ GeV events, in the different regions of the plot R vs $1-T$. The highest momentum particle (leading particle) in the event, located at $\Delta\phi$ = 0 radians, is not shown. Shown are: events in region (A) (dashed line), events in region (B) (dotted line), events of region (C) (solid line). In the right panel the three regions were adding (dashed-dotted line) and compared with STAR data [8]

Chapter 7

Energy loss

It has been predicted that a high-p_T parton traversing hot nuclear matter, will experience collisional energy loss, via scattering, and radiative energy loss, via induced gluon bremsstrahlung.

Radiative energy loss is expected to dominate over collisional energy loss. The amount of energy loss, ΔE, is predicted to be proportional to the gluon/energy density of the medium and a function of the path length of the parton through the medium. Thus jets, which have lost energy while traversing the medium, can be used as tools to probe the medium and provide information on its properties and structure at an early stage

The pQCD based calculations predict that the angular energy distribution for jets which have undergone energy-loss in a dense QCD medium is very similar to the energy distribution of jets which fragment in vacuum.

The gluons are radiated at angles close to the jet axis and remain inside the jet cone. Therefore, measuring the total energy within a cone of radius R_{c} around the jet axis will not provide information on jet energy loss since the total energy inside the cone will include both the final jet energy plus the radiated energy.

However, the momentum distribution of the particles within the jet cone is expected to be modified for jets which have lost energy due to medium effects. Jet energy loss is manifested by a shift of the fragmentation function towards low z, as shown by the increase above unity of low momentum (*i.e.,* low-z)[1] particles and the decrease in the number of high-z particles compared to the case with no energy loss *i.e.,* there is a shift of particles from high-p_T to low-p_T. Lower energy jets are more affected than higher energy jets.

Then, analysis of modifications of the structure of jets produced in nucleus-nucleus

[1] $z = p_T/E_{T\mathrm{jet}}$

collisions represent a very sensitive tool to study the interactions of partons with the medium.

In this work, we studied the effects of parton energy loss in a medium under extreme conditions of temperature and density. To achieve that, we simulate high-p_T events in $p+p$ collision with PYTHIA(see section 5), as a baseline, and events passed through two afterburner models of energy loss PYQUEN [11] and Q-PYTHIA [12].

7.1. PYQUEN model

PYQUEN (PYthia QUENched) [11] is a fast Monte-Carlo event generator routine implemented to modify standard jets events in PYTHIA 6.2.14. This model simulate rescattering, radiative and collisional energy loss of hard partons in expanding quark-gluon plasma created in ultra-relativistic heavy ion-ion collisions without considering possible effects of double parton scattering.

The model is based on an accumulating energy loss, the gluon radiation being associated with each parton scattering in the expanding medium and includes the interference effect using the modified radiation spectrum dE/dl as a function of decreasing temperature T. The kinetic integral equation for the energy loss ΔE as a function of initial energy E and path length L has the form

$$\Delta E(L,E) = \int_0^L dl \frac{dP(l)}{dl} \lambda(l) \frac{dE(l,E)}{dl}, \quad \frac{dP(l)}{dl} = \frac{1}{\lambda(l)} \exp\left(-l/\lambda(l)\right), \tag{7.1}$$

where l is the current transverse coordinate of a parton, dP/dl is the scattering probability density, dE/dl is the energy loss per unit length, $\lambda = 1/(\sigma\rho)$ is the in-medium mean free path, $\rho \propto T^3$ is the medium density at the temperature T, σ is the integral cross section for parton interaction in the medium.

The collisional energy loss is due to elastic scattering with high-momentum transfer taking also into account the low-momentum transfer loss resulting mainly from the interactions with plasma collective modes. This process does not contribute much to the total collisional loss in comparison with high-momentum scattering, due to the absence of a large factor $\sim \ln(E/\mu_D)$ where μ_D is the Debye screening mass [3]. Then, the collisional part associated with high-momentum transfer has the form:

$$\frac{dE}{dl}^{col} = \frac{1}{4T\lambda\sigma} \int_{\mu_D^2}^{t_{\max}} dt \frac{d\sigma}{dt} t \,, \tag{7.2}$$

and the dominant contribution to the differential cross section

$$\frac{d\sigma}{dt} \cong C\frac{2\pi\alpha_s^2(t)}{t^2}\frac{E^2}{E^2-m_p^2}\ , \quad \alpha_s = \frac{12\pi}{(33-2N_f)\ln(t/\Lambda_{QCD}^2)} \tag{7.3}$$

for scattering of a hard parton with energy E and mass m_p off the "thermal" parton with energy (or effective mass) $m_0 \sim 3T \ll E$. Here $C = 9/4, 1, 4/9$ for gg, gq and qq respectively, α_s is the QCD running coupling constant for N_f active quark flavors, and Λ_{QCD} is the QCD scale parameter which is of the order of the critical temperature, $\Lambda_{QCD} \simeq T_c \simeq 200$ MeV. The integrated cross section σ is regularized by the Debye screening mass squared $\mu_D^2(T) \simeq 4\pi\alpha_s T^2(1+N_f/6)$. The maximum momentum transfered is $t_{\max} = [s-(m_p+m_0)^2][s-(m_p-m_0)^2]/s$, where $s = 2m_0E + m_0^2 + m_p^2$.

The medium induced gluon radiation is restricted to BDMS formalism [45, 46]. In the BDMS framework, the strength of multiple scattering is characterized by the transport coefficient $\hat{q} = \mu_D^2/\lambda_g$ (λ_g is the gluon mean free path), which is related to the elastic scattering cross section σ. In this simulations, the strength is regulated mainly by the initial QGP temperature, T_0. Then the energy spectrum of coherent medium-induced gluon radiation and the corresponding dominant part of radiative energy loss of mass-less parton have the form:

$$\frac{dE}{dl}^{rad} = \frac{2\alpha_s(\mu_D^2)C_R}{\pi L}\int\limits_{\omega_{\min}}^{E} d\omega\left[1-y+\frac{y^2}{2}\right]\ln\left|\cos(\omega_1\tau_1)\right|, \tag{7.4}$$

$$\omega_1 = \sqrt{i\left(1-y+\frac{C_R}{3}y^2\right)\bar{\kappa}\ln\frac{16}{\bar{\kappa}}} \quad \text{with} \quad \bar{\kappa} = \frac{\mu_D^2\lambda_g}{\omega(1-y)}\ , \tag{7.5}$$

where $\tau_1 = L/(2\lambda_g)$, $y = \omega/E$ is the fraction of the hard parton energy carried away by the radiated gluon, and $C_R = 4/3$ is the quark color factor. A similar expression for the gluon jet can be obtained by changing the factor $C_R = 3$ in the square brackets in equation 7.4.

Another important element of the model is the angular spectrum of in-medium gluon radiation. Since the detailed calculation of the angular spectrum of emitted gluons is rather sophisticated and model-dependent, the simple parametrization of gluon angular distribution over the emission angle θ was used:

$$\frac{dN^g}{d\theta} \propto \sin\theta\exp\left(-\frac{(\theta-\theta_0)^2}{2\theta_0^2}\right), \tag{7.6}$$

where $\theta_0 \sim 5^0$ is the typical angle of the coherent gluon radiation as estimated in [47].

The internal model parameters are the initial conditions for the QGP formation expected for central ion-ion collisions (table 7.1).

Description	Parameter	Value
Medium-induced partonic energy loss	ienglu	0 - radiative and collisional 1 - radiative 2 - collisional
Initial temperature of quark-gluon plasma	T_c	0.2 GeV$< T_c <$ 2 GeV
Proper time of quark-gluon plasma formation	τ_0	0.01 fm/c $< \tau_0 <$ 10 fm/c
Number of active quark flavors in quark-gluon plasma	n_f	0, 1, 2 or 3
Angular distribution of emitted gluons	ianglu	0 - small - angular 1 - wide - angular 2 - collinear

Table 7.1: PYQUEN internal model parameters

The simulation procedure is:

- Generation of the initial parton spectra with PYTHIA (fragmentation *off*).
- Generation of the jet production vertex at the impact parameter b according to the distribution

$$\frac{dN^{\text{jet}}}{d\psi dr}(b) = \frac{T_A(r_1)T_A(r_2)}{T_{AA}(b)}, \quad T_{AA}(b) = \int_0^{2\pi} d\psi \int_0^{r_{max}} r dr T_A(r_1)T_A(r_2)\ , \tag{7.7}$$

  where $r_{1,2}(b,r,\psi)$ are the distances between the nucleus centers and the jet production vertex $V(r\cos\psi, r\sin\psi)$; $r_{max}(b,\psi) \leq R_A$ is the maximum possible transverse distance r from the nuclear collision axis to V; R_A is the radius of the nucleus A; $T_A(\mathbf{r}) = A\int \rho_A(\mathbf{r},z)dz$ is the nuclear thickness function with nucleon density distribution $\rho_A(\mathbf{r},z)$; $T_{AA}(b)$ is the nuclear overlap function (see ref. [48] for detailed nuclear geometry explanations).

- Calculation of scattering cross section
- Generation of the displacement between i-th and $(i+1)$-th scatterings, $l_i = (\tau_{i+1} - \tau_i)$ and calculation of the corresponding transverse distance, $l_i p_T/E$.

- Reducing the parton energy by collisional and radiative loss per each i-th scattering:
- Calculation of the parton transverse momentum kick due to elastic scattering i
- Formation of the additional (in-medium emitted) gluon with the energy ω_i and the emission angle θ_i relative to the parent parton.
- Halting the rescattering if *(1)* the parton escapes the dense zone, or *(2)* QGP cools down to T_c=200 MeV, or *(3)* the parton loses so much energy that its $p_T(\tau)$ drops below $2T(\tau)$.
- At the end of each event, adding new (in-medium emitted) gluons to the PYTHIA parton list and rearrangement of partons to update string formation.
- Formation of the final state particles by PYTHIA (fragmentation *on*).

The complete study for different PYQUEN parameters values and $p_{T\text{hard}}$ was done. Since the results do not change as function of $p_{T\text{hard}}$, only results with $p_{T\text{hard}}$ =50 GeV/c are shown. Similarly, only the important PYQUEN internal parameters used in $p+p$ simulation at $\sqrt{s_{\text{NN}}} = 5.5$ TeV are shown in table 7.2.

Parameter	**Value**
ienglu	0 - radiative and collisional 1 - radiative 2 - collisional
T_c	1 GeV 2 GeV
τ_0	0.01 fm/c
n_f	0
iangle	0 - small - angular

Table 7.2: PYQUEN internal parameters used for $p+p$ collisions at $\sqrt{s_{\text{NN}}} = 5.5$ TeV

Figure 7.1 show the transverse momentum distribution, with two temperature, for charged particles obtained with PYQUEN at $\sqrt{s_{\text{NN}}} = 5.5$ TeV and $p_{T\text{hard}}$ = 50 GeV/c. For the collisional part only a transfer momentum and parton transverse momentum kick due to elastic scattering is calculated. For radiative energy loss, the formation of the additional radiated gluon with energy ω_i and the emission angle θ_i relative to the parent parton is generated. Combination of both, collisional and radiative energy loss, is shown in dashed-dotted line. The result is: more particles with low p_T and less particles with high p_T.

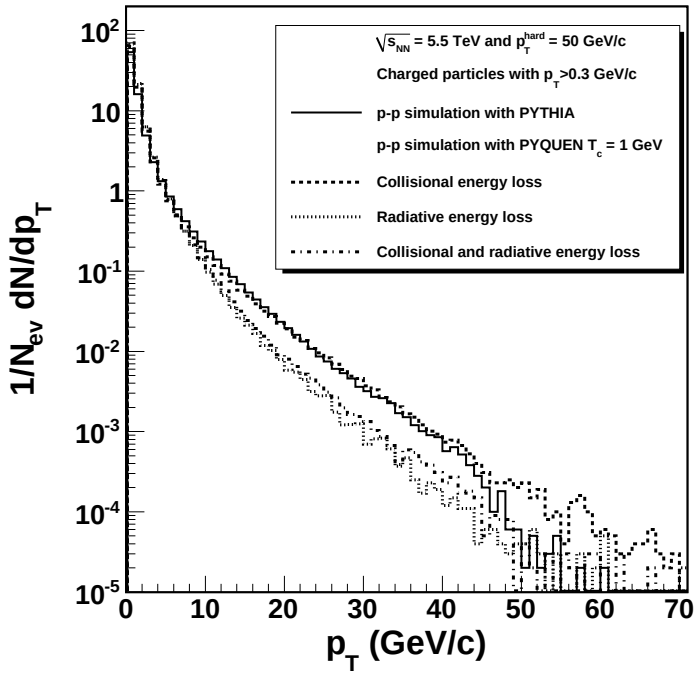

Figure 7.1: p_T distribution for $p+p$ collisions at $\sqrt{s_{\rm NN}} = 5.5$ TeV and p_T^{hard} = 50 GeV/c simulated only with PYTHIA (solid line) and with PYQUEN with collisional (dashed line), radiative (dotted line) and both (dashed-dotted line) energy loss at $T_{\rm c}$ = 1 GeV.

Figure 7.2 shows the azimuthal correlations between particles in the left panel and the ratio of particles yields ($R_{\rm AA}$ PYQUEN to PYTHIA) in the right, at $\sqrt{s_{\rm NN}} = 5.5$ TeV with $p_{T\rm hard}$ = 50 GeV/c for the collisional (top), radiative (middle) and collisional and radiative (bottom) energy loss at two $T_{\rm c}$. Since, in real data it is not possible to separate collisional and radiative energy loss, only the case with both together is studied. In this plots the formation of particles with low-p_T is clear, *i.e.,*a peak at low-p_T in $R_{\rm AA}$ and more particles in the azimuthal distribution, however, there is no significant difference with $T_{\rm c}$. In the next sections only $T_{\rm c}$ = 1 GeV is considred.

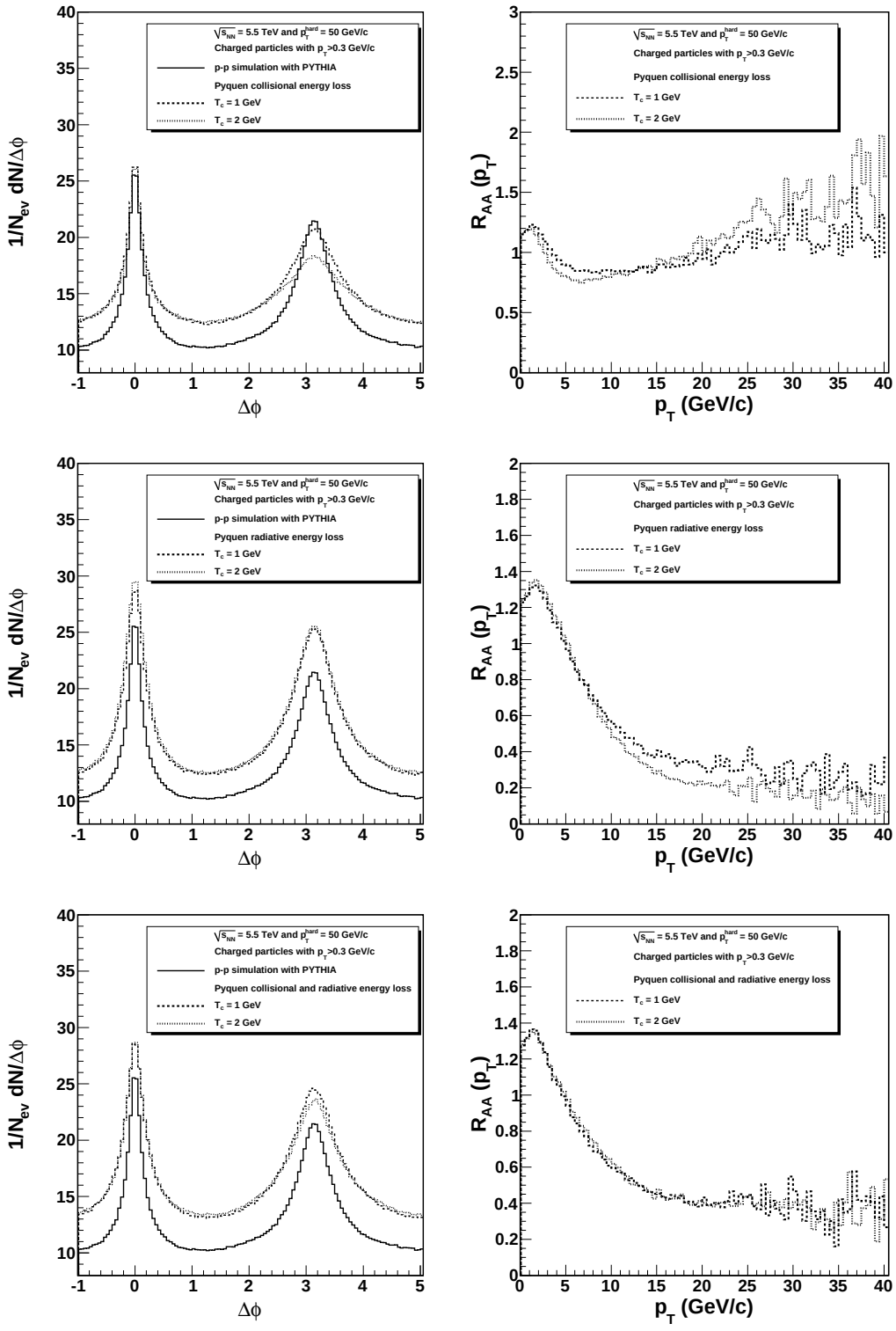

Figure 7.2: Dihadron azimuthal correlation (left) and R_{AA} (PYQUEN to PYTHIA) (right) for $p+p$ collisions at $\sqrt{s_{\mathrm{NN}}} = 5.5$ TeV and p_T^{hard} = 50 GeV/c simulated with PYQUEN with collisional (top) radiative (middle) and collisional and radiative (bottom) energy loss and T_{c} = 1 GeV (dashed line) and T_{c} = 2 GeV (dashed-dotted line).

7.2. Q-PYTHIA model

Q-PYTHIA [12, 49] is a modification of the final state showering routine PYSHOW in PYTHIA 6.4.18 that introduced a medium-induced term in the splitting probability function $P(z)$ and a formation time effect as an effective cut-off of the radiation without consider collisional energy loss.

The spectrum for medium-induced gluon radiation is a sum of a vacuum term plus a medium-induced term

$$\frac{dI^{\text{tot}}}{dz\,d\mathbf{p}_T^2} = \frac{dI^{\text{vac}}}{dz\,d\mathbf{p}_T^2} + \frac{dI^{\text{med}}}{dz\,d\mathbf{p}_T^2}\,. \tag{7.8}$$

The vacuum term can be related with the standard Dokshitzer-Gribov-Lipatov-Altarelli-Parisi (DGLAP) splitting functions $P_{\text{vac}}(z)$ [50],

$$\frac{dI^{\text{vac}}}{dz\,d\mathbf{p}_T^2} = \frac{\alpha_s}{2\pi}\frac{1}{\mathbf{p}_T^2}P_{\text{vac}}(z),\;\; P_{\text{vac}}(z) \simeq \frac{2C_R}{1-z}\,. \tag{7.9}$$

where $1-z$ is the momentum fraction of the parent parton momentum taken by the emitted gluon, $\mathbf{p_T}$ the transverse momentum of the emitted gluon with respect to the direction of its parent, α_s is the QCD running coupling constant and C_R the quadratic Casimir of the color representation of the parent parton.

By matching the medium and the vacuum cases, the corresponding modification to the splitting probability function is:

$$P_{\text{tot}}(z) = P_{\text{vac}}(z) \rightarrow P_{\text{tot}}(z) = P_{\text{vac}}(z) + \Delta P(z,t,\hat{q},L,E),\;\; \Delta P(z,t,\hat{q},L,E) \simeq \frac{2\pi t}{\alpha_s}\frac{dI^{\text{med}}}{dzdt}\,. \tag{7.10}$$

The correction $\Delta P(z,t,\hat{q},L,E)$ depends not only on the energy fraction z but also on the virtuality $t = z(1-z)\mathbf{p}_T^2$ of the radiating parton and its energy E, medium length L and transport coefficient $\hat{q}$. The transport coefficient $\hat{q}$ encodes all possible information about the medium properties as temperature, density, etc. in a single parameter, with the interpretation of the average transverse momentum squared that the gluon gets per mean free path in the medium.

The basic procedure followed by Q-PYTHIA is: given a parton coming from a branching (or production) point with coordinates (t_1,x_1), with t_1 the virtually and x_1 its energy fraction, compute the coordinates (t_2,x_2) for the next branching.

The scale t of the evolution in PYTHIA is chosen to be the invariant mass squared

of the decaying particles. The showering is performed by the creation of pairs of partons, conserving four-momentum at each step. If, in the course of the evolution, a parton a reaches a scale t_a that is smaller than any minimal mass of any allowed branching mode, then its mass and its scale will be set to its current mass m_a^0 and it will leave the parton shower without further branching. The evolution has a scale cut-off $t_0 = Q_0^2$.

The geometry of a dense medium produced in nucleus–nucleus collision can be chosen by the user. The simplest is a brick geometry with L = 4.5 fm and $\hat{q}$ = 5 GeV^2/fm and $\hat{q}$ = 50 GeV^2/fm to exemplify the dependence of energy loss with $\hat{q}$, also a realistic Glauber-like collision geometry is defined, in this geometry the production points and the quenching parameters are defined like in the PQM model [51]. The production points of the hard scatterings are distributed in the nuclear overlapping area according to the probability of central nucleon-nucleon collisions. Then, $\hat{q}$ and in-medium path length L are computed locally through two integrals of the density of binary nucleon-nucleon collisions along parton trajectories isotropically distributed in azimuth. In this model the only free parameter is the scale of the transport coefficient $k = 6 \cdot 10^6$ fm, which corresponds to an average $\langle \hat{q} \rangle = 14$ GeV^2/fm in a 0-10% central collision.

Figure 7.3 shows the p_T distribution and 7.4 the azimuthal correlation between particles in the left panel and the ratio of particles yields (Q-PYTHIA and PYTHIA) as function of p_T in the right panel, at $\sqrt{s_{\mathrm{NN}}} = 5.5$ TeV and p_T^{hard} = 50 GeV. Two geometry are used, brick geometry with 2 values of $\hat{q}$ and the Glauber geometry.

We can see:

- Increase of multiplicity and p_T spectrum is harder for PYTHIA than Q-PYTHIA.
- Re-distribution of particles in azimuthal angle, compared with PYTHIA.

Once particle production simulation was made, with and without energy loss, we proceed to reconstruct jets using a cone jet algorithm (JETAN) and event shape analysis (ESA). This procedure is described in the next section.

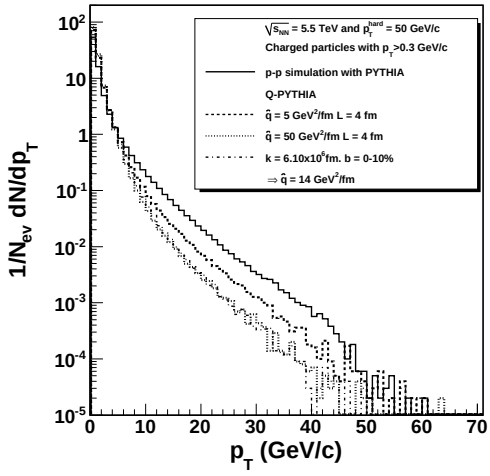

Figure 7.3: p_T distribution for $p+p$ collisions at $\sqrt{s_{\rm NN}} = 5.5$ TeV and p_T^{hard} = 50 GeV/c simulated only with PYTHIA (solid line) and with Q-PYTHIA with L = 4 fm and 2 values of $\hat{q}$ in brick geometry (dashed and dotted line) and Glauber geometry (dashed-dotted line)

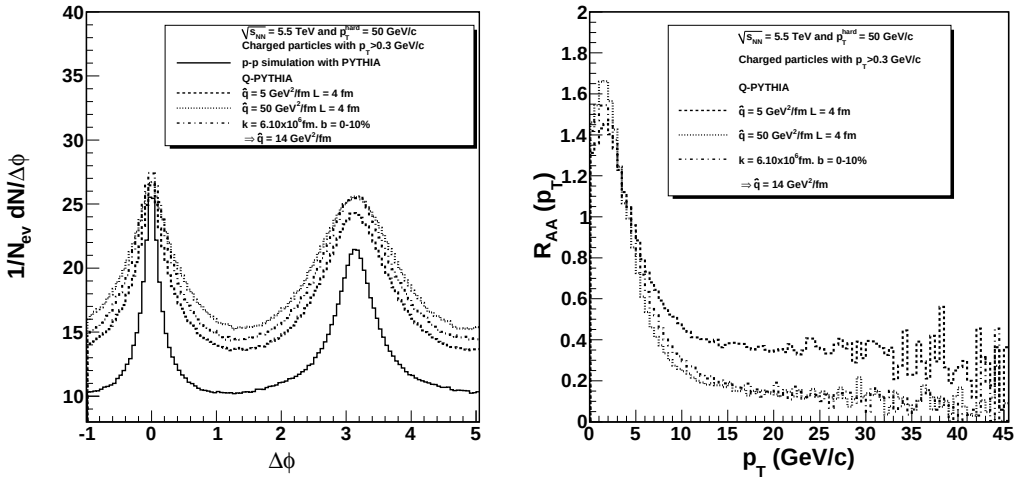

Figure 7.4: Dihadron azimuthal correlation (left) and $R_{\rm AA}$ (right) for $p+p$ collisions at $\sqrt{s_{\rm NN}} = 5.5$ TeV and p_T^{hard} = 50 GeV/c simulated only with PYTHIA (solid line) and with Q-PYTHIA with L = 4 fm and 2 values of $\hat{q}$ in brick geometry (dashed and dotted line) and Glauber geometry (dashed-dotted line)

Chapter 8

Acoplanarity for dijets (k_T) and the transverse momentum of a jet (j_T)

Jet are produced in the hard scattering of two partons. Two partons collides resulting in two outgoing partons with roughly opposite high-p_T. This outgoing partons fragment into jets of hadrons one on toward side (trigger) and one on the away side, in the azimuthal plane (the plane is formed by the two beams and the trigger jet). Others jets have small-p_T and result from the break up of the two partons collides, usually refereed to as soft hadronic background.

Each of the particle carriers a transverse momentum, this transverse momentum can arise from two sources: the transverse momentum of partons inside proton, originally describe as "intrinsic" transverse momentum k_T and the transverse momentum relative to the jet axis j_T, given to a particle during the fragmentation of its parent after scattering.

The two components of the vector k_T, $k_{T\mathrm{x}}$ and $k_{T\mathrm{y}}$, are Gaussian distributed and result in different experimentally measurable effects. $k_{T\mathrm{y}}$ leads to the acoplanarity of the dijet pair while $k_{T\mathrm{x}}$ makes the momentum of the jets unequal. Also, j_T is a two-dimensional vector. The component of j_T projected onto the azimuthal plane, $j_{T\mathrm{y}}$, is perpendicular to the jet transverse axis. The other component, $j_{T\mathrm{x}}$, is perpendicular to the jet transverse axis in the longitudinal plane.

The average transverse momentum component of the away side particles $p_{T\mathrm{a}}$ is label as p_{out} and can be obtained by:

$$\langle |p_{\mathrm{out}}| \rangle^2 = \left\langle |k_{T\mathrm{y}}| \right\rangle x_E^2 + \left\langle |j_{T\mathrm{y}}| \right\rangle (1 + x_E^2) \tag{8.1}$$

where $\left\langle |k_{T\mathrm{y}}| \right\rangle$ and $\left\langle |j_{T\mathrm{y}}| \right\rangle$ are the average values of the components of transverse momentum out of the scattering plane and $x_E = -p_{T\mathrm{a}} p_{T\mathrm{t}} / |p_{T\mathrm{t}}|^2$ represents the fragmentation variable of the away-side jet. The magnitude of p_{out} between dijets and the transverse momentum of particles inside jets can be calculated as well as j_T by:

$$p_{\text{out}} = |p_{T\text{a}}| \sin\Delta\phi \tag{8.2}$$

$$j_T = |p_{T\text{a}}| \sin\phi \tag{8.3}$$

where $\Delta\phi$ is the azimuthal angle between jets and ϕ is the azimuthal angle relative to the jet axis [58, 59, 60].

We show results obtained for the acoplanarity between dijets and the modifications of the fundamental properties of jets due to their interaction with a dense medium.

8.1. Acoplanarity for dijets

In order to understand the behavior of k_T in hadron collisions, we studied its dependence with the energy of the collision and the transverse momentum of the hard-p_T particles. High-p_T particles was produced using the PYTHIA event generator in $p+p$ changing the parameters PARP(91) and PARP(93), that control the magnitude of the intrinsic transverse momentum in the collisions (see table 5.1).

After event generation, jets were reconstructed with cone jet algorithm implemented in the module JETAN of ALIROOT. Table 8.1 show the parameters used in the simulation.

PYTHIA 6.2	CONE ALGORITHM
$\sqrt{s_{\text{NN}}} = 900$ GeV, 5.5 TeV and 14 TeV	R_{c}<0.7
p_T^{hard} = 30,50,70,100,150,200 GeV/c	$\|\eta\|$ <0.9
k_T=0, 5, 7.5, 10 and 15 GeV/c	No p_T^{cut}
IR and FR off/on	E_T > 0 GeV

Table 8.1: Parameters used in k_T the simulation

Figure 8.1 show the acoplanarity between two jets, defined in equation 8.2, as function of center of mass energy, $\sqrt{s_{NN}}$ and p_T^{hard}. As expected, the acoplanarity between two jets increased with the intrinsic k_T (left). p_{out} increase with increasing p_T^{hard} and center of mass energy. At higher center of mass energy p_{out} shows a small dependence on the unknown intrinsic k_T due to the dominance of initial state radiation (rigth).

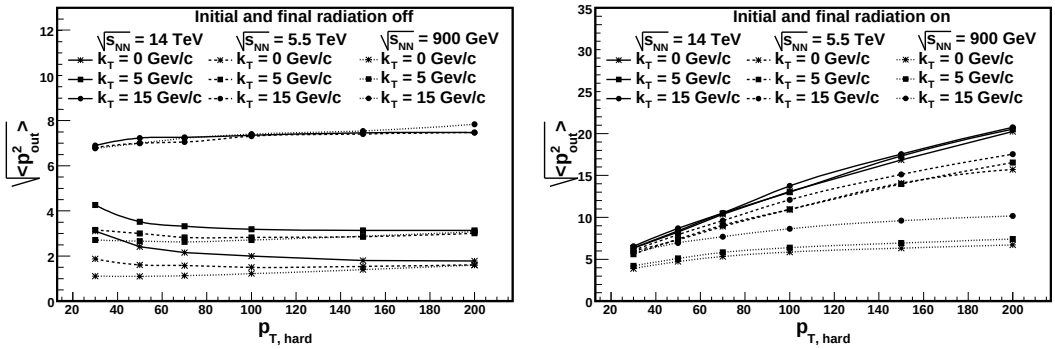

Figure 8.1: $p_{\rm out}$ as a function of transverse momentum of the partons is show for different values of k_T and center of mass energies without (left) and with (right) initial and final radiation

After parton are produced using PYTHIA, they are passed through PYQUEN (section 7.1) and Q-PYTHIA (section 7.2), taking into account initial and final state radiation and k_T = 5 GeV/c. The system created was under the assumption of $T_{\rm c}$ = 1 GeV and with collisional and radiative energy loss, for PYQUEN and $k = 6 \cdot 10^6$ fm, which corresponds to an average $\langle \hat{q} \rangle = 14$ GeV^2/fm in a 0-10% glauber central collision for Q-PYTHIA.

The left panel of figure 8.2 show the transverse momentum imbalance defined as the difference between the trigger jet ($\vec{p}_{T,t}$) and the away-side jet ($\vec{p}_{T,a}$) transverse momentum in the trigger jet-beam plane.

$$p_{max} - p_{proj} = |p_{Tt}| - |p_{Ta} Proj(p_{Tt})| = \sqrt{2} k_{Tx} \tag{8.4}$$

and in the rigth panel is shown the acoplanarity between dijets. Comparing both models to simulate energy loss, Q-PYTHIA (dashed line) and PYQUEN (dotted line) with PYTHIA (solid line) the extra k_T from partonic interactions with the dense medium can be observed on top of the initial state radiation.

8.2. Transverse momentum j_T

High-p_T events were produced using the PYTHIA event generator in $p+p$ and jets are reconstructed with UA1 jet cone algorithm implemented in the module JETAN of ALIROOT. In order to study the ideal case *i.e.,* all the particle inside the jet, jets with a $R_{\rm c}$ =1 were reconstructed .

Figure 8.3 shows the ratio of particles yield (R_{AA}) vs p_T for two energy loss models.

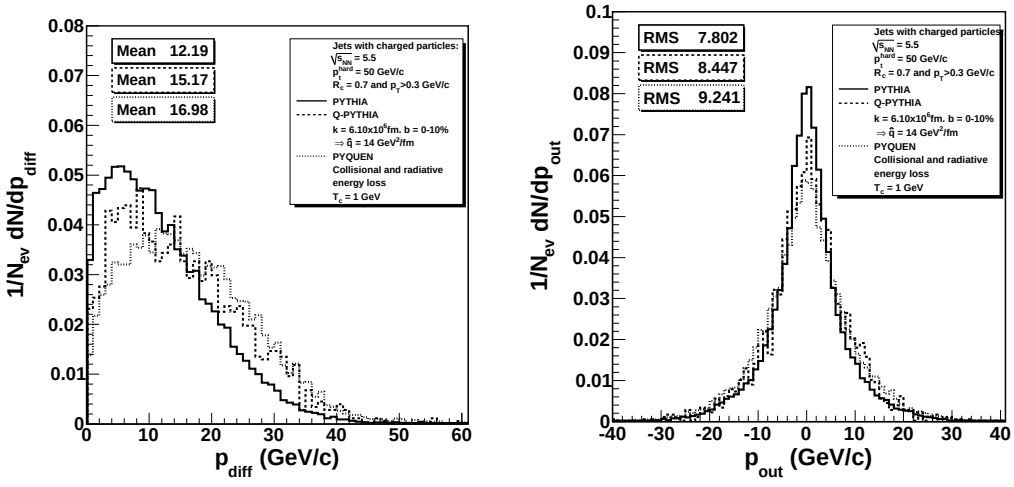

Figure 8.2: $p_{\mathrm{T,diff}}$ (left) and p_{out} (rigth) for charged dijets with R_{c}= 0.7 and p_T^{hard} = 50 GeV/c at $\sqrt{s_{\mathrm{NN}}} = 5.5$ TeV with PYTHIA (solid line), PYQUEN (dashed line) with T_0 = 1 GeV and Q-PYTHIA (dotted line).

As expected, a decrease of the number of particles carrying high-p_T and an increase in the number of low-p_T particles is observed.

Figure 8.4 shows the ratio of particles yield (R_{AA}) (Q-PYTHIA/PYTHIA in the left panel and PYQUEN/PYTHIA in the rigth panel) vs p_T for three r values. Clear differences between the two `Monte-Carlo` in the pattern of increase of low-momentum particles and depletion of high-momentum particles at different r can be observed. In vacuum angular ordering rules the p_T distribution of particles at different distances r to the jet axis. High-p_T particles are predominantly produced close the jet axis whereas low-p_T particles are found at larger distances. High-p_T particles at large distances from the jet axis are due to hard gluons radiated shortly after the initial hard scattering. These gluons see the same medium as the leading parton, but having smaller energies the effect of energy loss should be stronger.

Broadening of the distribution of jet-particle momenta perpendicular to the jet axis, j_T distribution are show in figure 8.5 (left) and the ratio between the two models and PYTHIA (right). Additional broadening is observed and this is directly related to the colour density of the traversed medium.

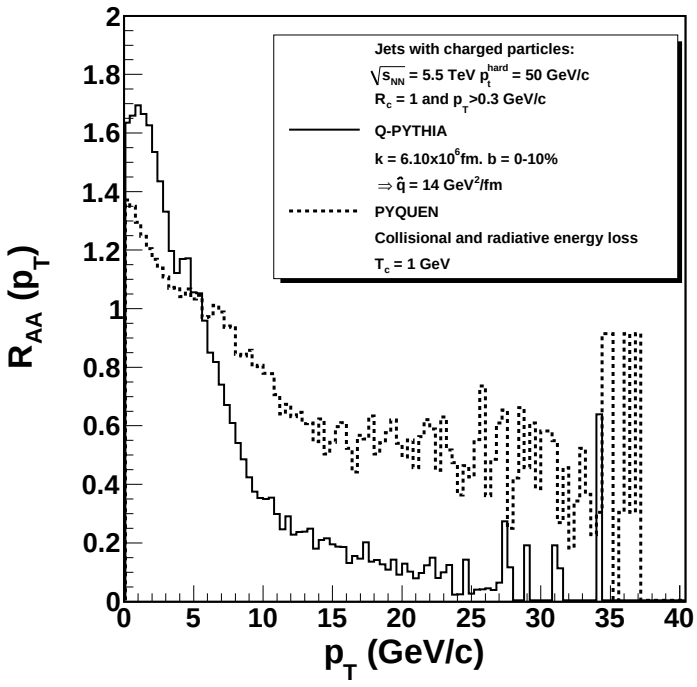

Figure 8.3: Ratio of particles yield (R_{AA}) vs p_T between $p+p$ and $Pb+Pb$ collision with p_T^{hard} = 50 GeV/c at $\sqrt{s_{\rm NN}} = 5.5$ TeV and $|\eta| < 1.9$

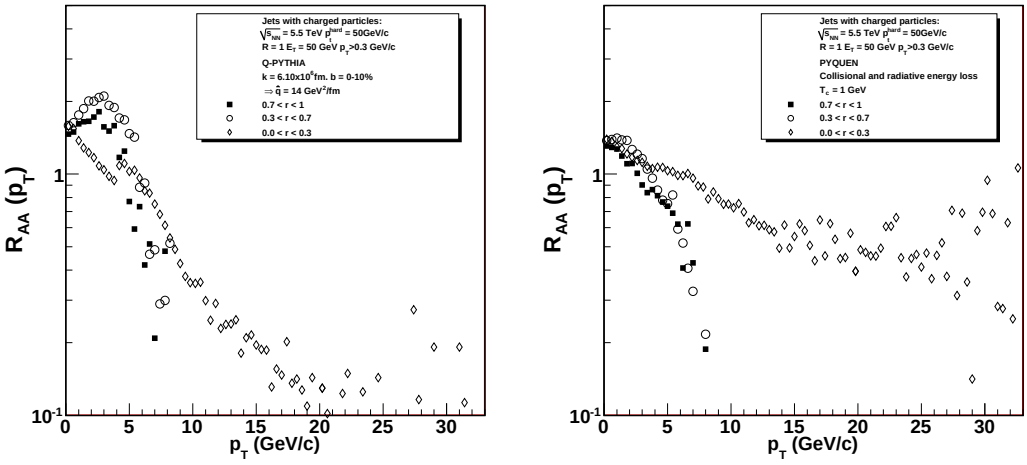

Figure 8.4: Ratio of particles yield (R_{AA}) vs p_T in Q-PYTHIA and PYTHIA (left) and PYQUEN and PYTHIA (rigth) at different distances r to the jet axis for $p+p$ collision with p_T^{hard} = 50 GeV/c at $\sqrt{s_{\rm NN}} = 5.5$ TeV and $|\eta| < 1.9$

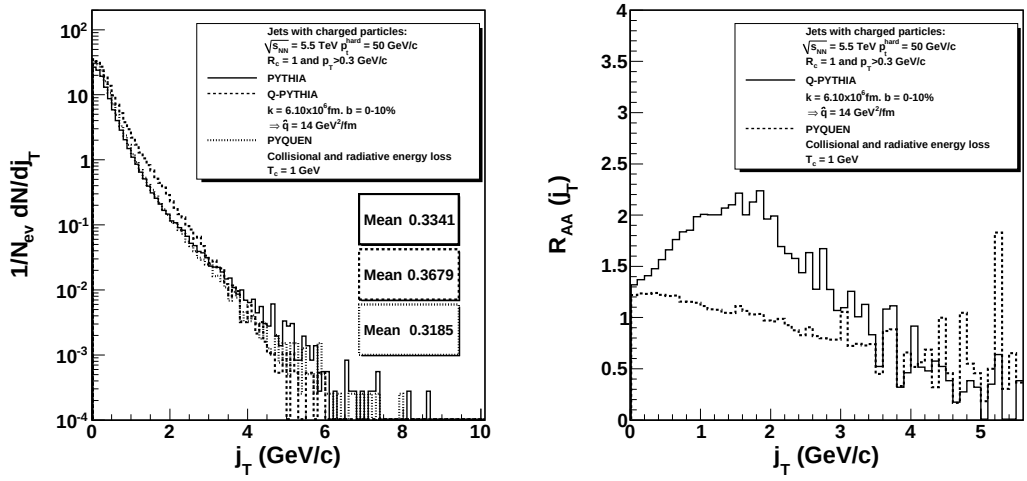

Figure 8.5: j_T distribution (left) and ratio of particles yield (R_{AA}) vs j_T between $p+p$ and $Pb+Pb$ collision (rigth) with p_T^{hard} = 50 GeV/c at $\sqrt{s_{\rm NN}} = 5.5$ TeV and $|\eta| < 1.9$

Chapter 9

Event shape analysis in a dense medium

Confronted with the double hump structure obtained in section 6.3.2 we have tried to see what are the predictions of a generator Q-PYTHIA (section 7.2), that takes into account the effects of parton energy loss in the medium simulating the effects to be observed in heavy ion collisions.

9.1. Azimuthal correlations at RHIC energy

In figure 9.1 we compare the effect of Q-PYTHIA on the event shape using a sample of events generated at $\sqrt{s_{\mathrm{NN}}} = 200$ GeV with a hard cutoff in $p_{T\mathrm{leading}} > 10$ GeV/c and a lower p_T^{cut} on the hadrons of 0.5 GeV/c. The curves obtained correspond to three distinct choices of parameters of Q-PYTHIA: A medium path length of 6 fm with two choices of $\hat{q}$, 1 and 5 GeV^2/fm. The interest of the results lays in the behavior of the dependence of the yields in two different parts of the $1-T$ vs R distribution. While for low values of R and $1-T$ we observe a decrease of the probability with increasing $\hat{q}$, in the case of high values of $1-T$ we observe a frank increase of the yield in the away-side correlation with the double hump. These results remind us very much of the double hump structures encountered in the RHIC experiments in collisions of heavy ions.

9.2. Event Shape Analysis (ESA) at LHC energy

At $\sqrt{s_{\mathrm{NN}}} = 5.5$ TeV, charged particles for hard processes with p_T^{hard} = 50 GeV/c are simulated. Even though hard processes are simulated, isotropic events are present (top of figure 9.2). Increasing the p_T^{cut} (middle and bottom of figure 9.2) events with monojets and dijets are selected and the backgound decreases. This behavior is clearly seen in the azimuthal distribution (rigth panels), obtained from the three regions selected with cuts in described in table 9.1.

To study the effect of PYQUEN and Q-PYTHIA in the event shape variables used to

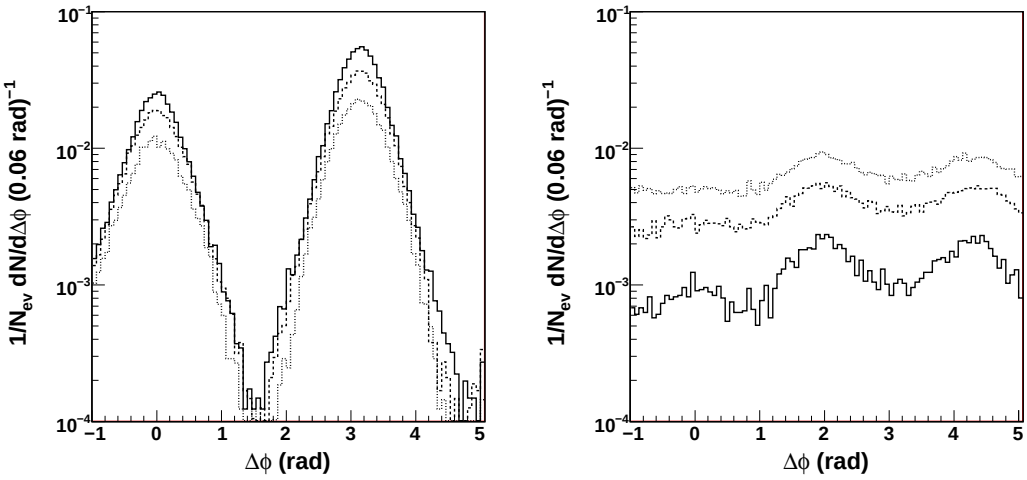

Figure 9.1: Dihadron azimuthal correlations for charged particles in region A (left) and C (right) (see table 6.3) with $p_t^{hard} = 10$ GeV/c (solid line), Q-PYTHIA with $\hat{q} = 1$ GeV^2/fm and $L = 6$ fm (dashed line) and $\hat{q} = 5$ GeV^2/fm and L = 6 fm (dotted line), respectively. The chosen bounds for $1 - T$ and R are $1 - T < 0.05$ and $R < 0.2$.

Region	Kind of event	Variables
A	Dijets	$R \leq 0.35$, $\tau \leq 0.03$
B	Monojets	$R \geq 0.9$, $\tau \leq 0.03$
C	Mercedes	$R \leq 0.4$, $\tau \geq 0.25$

Table 9.1: 1-T and R parameters used for the present analysis.

describe the topology of the events, charged particles for hard processes with p_T^{hard} = 50 GeV/c, $\sqrt{s_{\rm NN}} = 5.5$ TeV and three p_T^{cuts} and $p_{T\rm leading} > 10$ GeV/c, were produced and passed through these models.

Sphericity of the event, $\tau \equiv 1 - T$, the vector sum of the transverse momentum of the event R and the measure of the momentum out of the plane T_{min}, are shown in figure 9.3, 9.4 and 9.5, respectively.

Due to interaction with the dense medium, there is more particle production with low-p_T with PYQUEN and Q-PYTHIA than PYTHIA. The increment in the particle with low-p_T produce events with a uniform distribution. This is shown in the top and middle

panels of figure 9.3. For $\tau_{pp} \gtrsim 0.8$ PYQUEN and Q-PYTHIA particle production is above PYTHIA production and for $\tau_{pp} \lesssim 0.8$, they are below PYTHIA production. This behavior also change recoil and T_{min} distribution at low-p_T (top and middle panels of figure 9.4 and figure 9.5). At high-p_T (bottom panels in the same figures) there are no difference between $p+p$ and $Pb+Pb$.

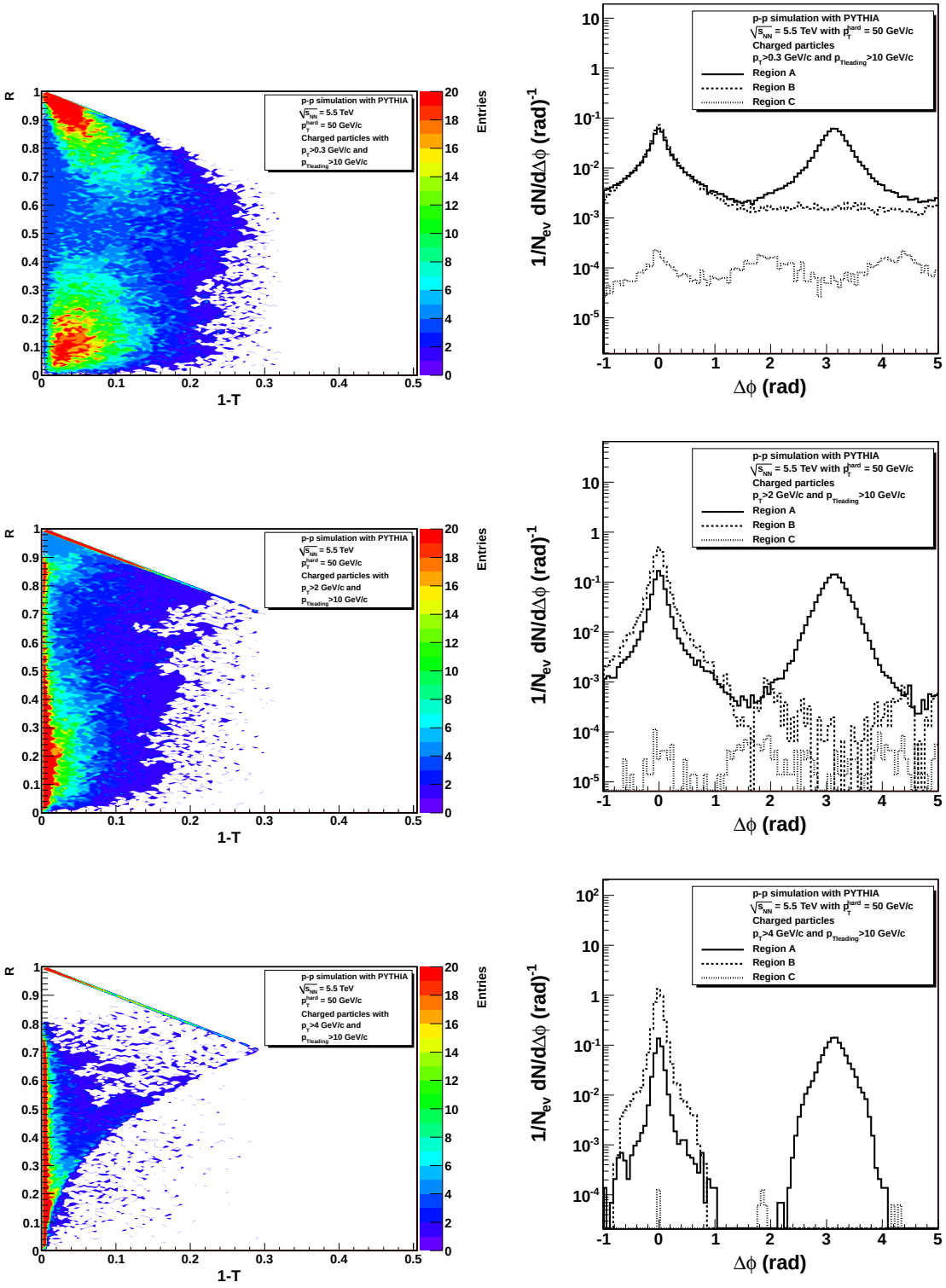

Figure 9.2: $1-T$ vs R (left) and dihadron azimuthal correlations (rigth) for charged particles produced in $p+p$ collisions at $\sqrt{s_{\rm NN}} = 5.5$ TeV with p_T^{hard} = 50 GeV/c. The cuts used in ESA are: $|\eta| < 0.9$, $p_{T\rm leading} > 10$ GeV/c and $p_T^{cut} > 0.3$ GeV/c (top), $p_T^{cut} > 2$ GeV/c (middel) and $p_T^{cut} > 4$ GeV/c (bottom).

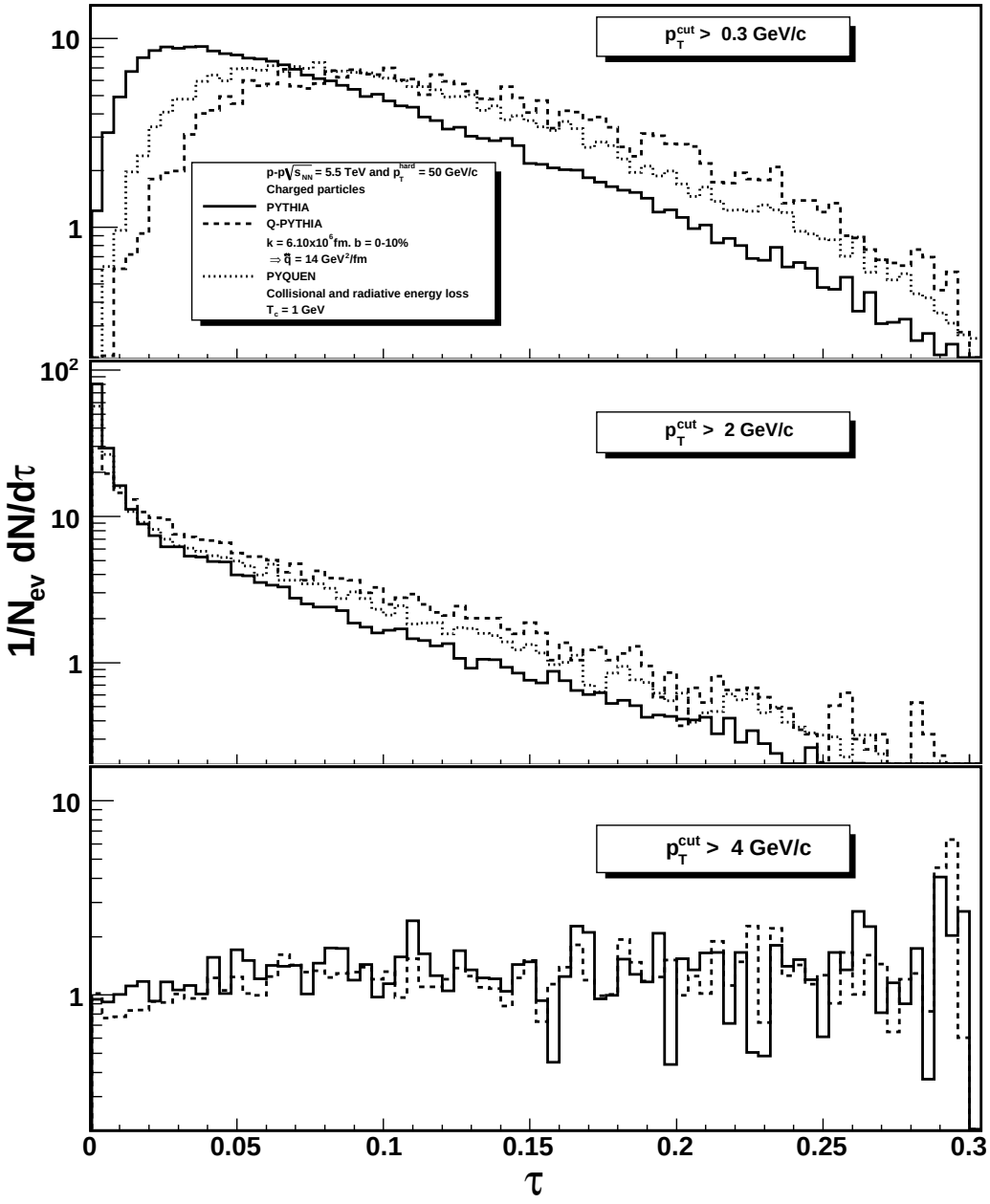

Figure 9.3: Thrust distribution in PYTHIA (solid line), Q-PYTHIA (dashed line) and PYQUEN (dotted line) at $\sqrt{s_{\rm NN}} = 5.5$ TeV and $p_{T\rm hard}$ = 50 GeV/c, $\eta| < 0.9$, $p_{T\rm leading} > 10$ GeV/c and $p_T^{cut} > 0.3$ GeV/c (top), $p_T^{cut} > 2$ GeV/c (middle) and $p_T^{cut} > 4$ GeV/c (bottom).

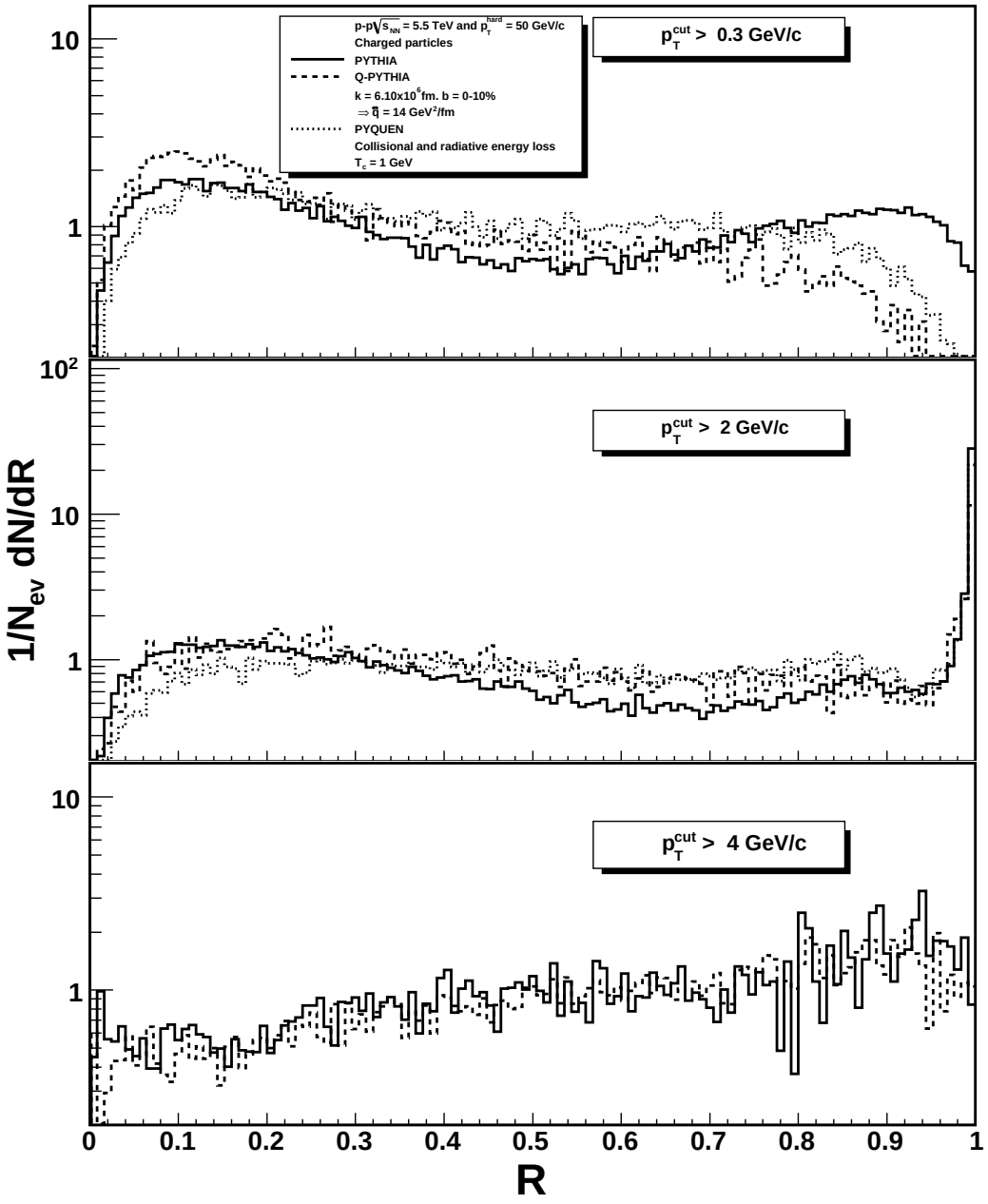

Figure 9.4: Recoil distribution in PYTHIA (solid line), Q-PYTHIA (dashed line) and PYQUEN (dotted line) at $\sqrt{s_{\rm NN}} = 5.5$ TeV and $p_{T\rm hard}$ = 50 GeV/c , $\eta| < 0.9$, $p_{T\rm leading} >$10 GeV/c and $p_T^{cut} > 0.3$ GeV/c (top), $p_T^{cut} > 2$ GeV/c (middle) and $p_T^{cut} >$ 4 GeV/c (bottom).

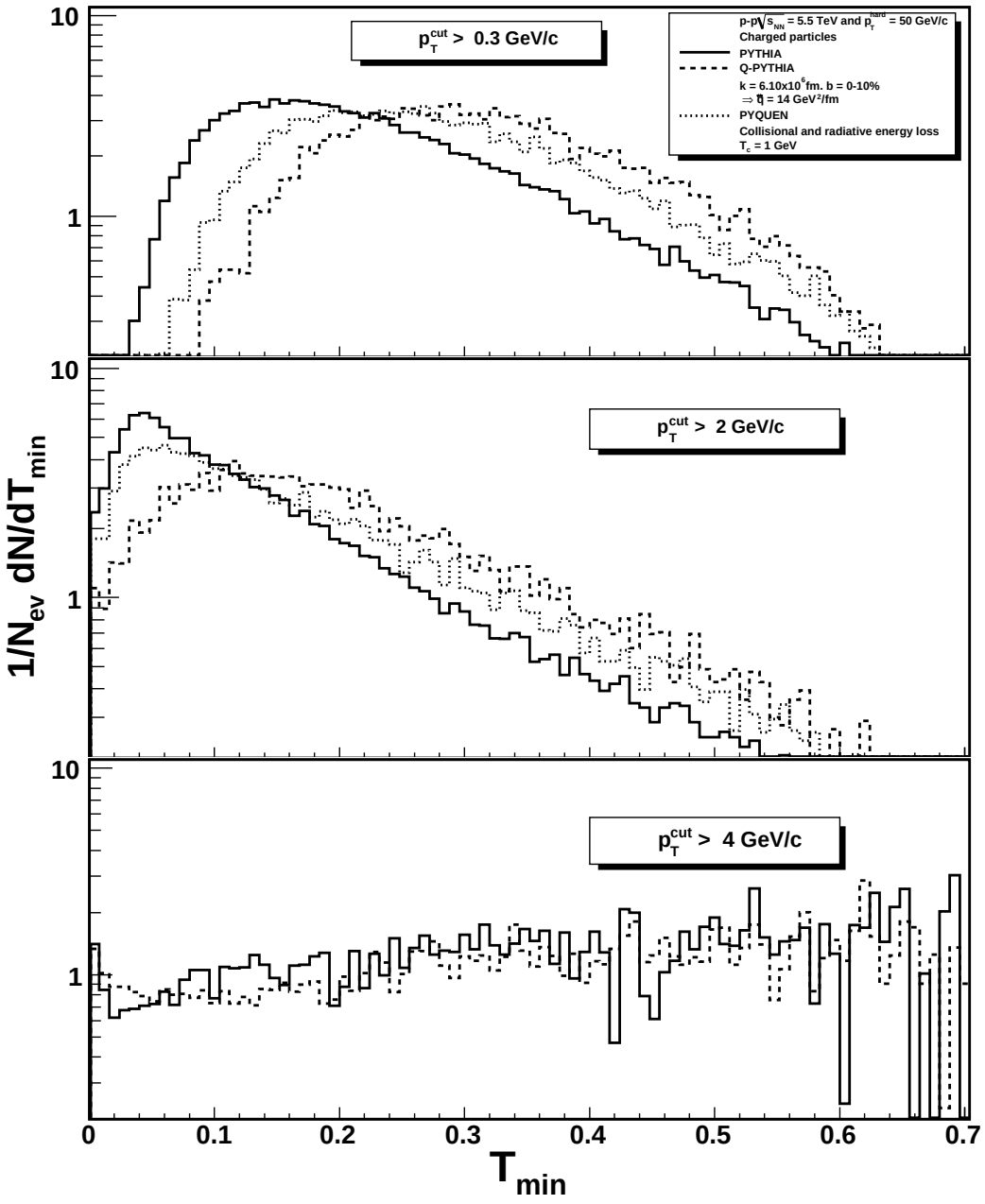

Figure 9.5: Thrust minor in PYTHIA (solid line), Q-PYTHIA (dashed line) and PYQUEN(dotted line) at $\sqrt{s_{\rm NN}} = 5.5$ 'tev and $p_{T\rm hard}$ = 50 GeV/c , $\eta| < 0.9$, $p_{T\rm leading} > 10$ GeV/c and $p_T^{cut} > 0.3$ GeV/c (top), $p_T^{cut} > 2$ GeV/c (middle) and $p_T^{cut} > 4$ GeV/c (bottom).

Chapter 10

Discussion and Conclusion

In this thesis we present simulation and analysis in the framework of the ALICE experiment in CERN. Specifically we have concentrated on the aspect of jets in proton-proton and heavy ion collisions and modifications in jets structure, due to parton energy loss.

We simulated high-p_T events in $p+p$ collision, with PYTHIA, as a baseline, and events passed through two afterburner models of energy loss PYQUEN and Q-PYTHIA. After events simulation, jets were reconstructed in the framework of the ALICE experiment (ALIROOT) with a jet finding algorithm and event shape analysis. Finally modifications in jet structure due to energy loss were studied through the variables k_T, j_T, R_{AA}, sphericity, recoil and thrust minor, were studied.

The particle production was done to improve the jets production selecting hard processes in PYTHIA version 6.2.14 $Tune\ A$. A calibration sample of a fixed interval with p_T^{hard} = 50 GeV/c and, to approach the real spectrum produced in ALICE, an interval with p_T^{hard} = 30 - 179 GeV/c were produced.

Even when the full event simulation performed within the ALIROOT framework mixed event with all particles of the signal, as well as the background, the signal sticks out of the background, so that, it was possible to do the analysis only with jet signal, *i.e.,* only with PYTHIA simulation, without taking into account the background (HIJING simulation).

After event generation, jets were first reconstructed with the internal PYTHIA cone algorithm routine, PYCELL, and subsequently with a cone jet algorithm implemented in the module JETAN of ALIROOT.

Notwithstanding only hard processes were simulated, the production of low-p_T particles is present, these particles caused that the cone jet algorithm reconstructed fake jets. If the particles transverse momentum is greater than 0.3 GeV/c a huge amount of particles with low-p_T are present between the the two-peaks in the par-

ticles azimuthal correlations, this particles are considered like background. With a higher transverse momentum cut this background is reduced. A $p_T^{cut} > 2$ GeV/c was used.

Another source of fakes jets reconstruction is the jet cone size. Looking at the azimuthal correlation between dijets we can see that there exist fake jets reconstructed close to the jet with maximum energy when the cone size is small, due to part of the energy of the jet is not inside the cone. One way to select only real dijets that are opposite in azimuthal angle and with small difference in energy is defining cuts in this variables. The cuts applied were: 2.8 rad $<\Delta\phi<$3.4 rad and $\Delta E_T \ / E_{T,max} < 0.8$. Moreover the cone jet algorithm, combined with the event shape analysis (ESA) making possible to describe the topology of jets in an the event, since ESA measures the geometrical properties of the energy flow in QCD states. In this work, three shape variables were used: thrust T (related with the sphericity S of the event $S \sim \tau \equiv 1 - T$), recoil R and thrust-minor T_{min}.

The thrust map (τ vs R) allows to identify different classes of events according with their location. $R \leq 0.35$ and $\tau \leq 0.03$ is characterized by dijets events, $R \geq 0.9$ and $\tau \leq 0.03$ is populated by monojets and $R \leq 0.4$ and $\tau \geq 0.25$ have the most isotropic events, called "mercedes". An extensive work with ESA was reported in [14] and [15].

Once the jets were selected, with either of the two methods, a study was done in the structure and distribution of jets and how their properties are affected by the presence of a dense medium.

It has been predicted that a high-p_T parton traversing hot nuclear matter, will experience collisional energy loss, via scattering, and radiative energy loss, via induced gluon bremsstrahlung. In this work, we studied the effects of this parton energy loss with two models: PYQUEN and Q-PYTHIA and using $p+p$ simulation with PYTHIA as baseline. There are other models to simulate energy loss, but due to availability in the ALIROOT framework and the observable under study, only these two were used.

PYQUEN and Q-PYTHIA are fast `Monte-Carlo` event generator routines implemented to modify standard events in PYTHIA. PYQUEN is based on an accumulating energy loss where the multiple scattering strength is regulated mainly by the initial QGP temperature T_c and Q-PYTHIA introduced a medium-induced term in the vacuum term splitting probability function $P(z)$ where the transport coefficient $\hat{q}$ encodes all possible information about the medium properties with the interpretation of the average transverse momentum squared that the gluon gets per mean free path length L in the medium. In both models, the main contribution comes from the radiative energy loss, resulting more particles at low p_T and less particles at high p_T compared with PYTHIA, but an important difference between them is that, Q-PYTHIA includes multiple-soft scattering and which is not the case in PYQUEN.

In PYQUEN the collisional energy loss due to elastic scattering takes into account the low-momentum transfer loss resulting from the interactions with plasma, but, this does not contribute much to the total energy loss in comparison with radiative energy loss, for this reason, and due to the fact that in real data, it is not possible to separate collisional and radiative energy loss, only the case with both together was studied. Since the energy loss is regulated by the initial QGP temperature T_{c}, two temperatures were selected but since no significant difference on T_{c} was observed. Only T_{c} = 1 GeV is considered.

In Q-PYTHIA the geometry of a dense medium produced in nucleus–nucleus collision can be chosen by the user .The simplest brick geometry with L = 4.5 fm and $\hat{q}$ = 5 GeV^2/fm and $\hat{q}$ = 50 GeV^2/fm were studied to exemplify the dependence on the energy loss with $\hat{q}$, but in order to compare, either `Monte-Carlo` (PYQUEN uses the same geometry) or real data, a realistic Glauber-like collision geometry defined in the routine, was chosen.

In order to understand the behavior of the intrinsic transverse momentum k_T and it dependence with the energy of the collision and the transverse momentum of the hard-p_T particles, high-p_T events were produced in $p+p$ environment, changing the parameters that control the magnitude of k_T. After event generation, jets were reconstructed with cone jet algorithm implemented in the module JETAN of ALIROOT and the acoplanarity (p_{out}) between two jets were calculated.

As expected, the acoplanarity between two jets increased because they were affected by additional transverse momentum contributions from the intrinsic k_T but, due to the dominance of initial state radiation p_{out} shows only small variations.

With a k_T = 5 GeV/c, both models to simulate energy loss, Q-PYTHIA and PYQUEN, were compared with PYTHIA. The magnitude of the extra k_T from partonic interactions with the dense medium can be observed on top of the initial state radiation but this effect is less than the theoretical prediction [61], where the amount of additional transverse momentum to of the dijet system relative to the $p+p$ or $p+A$ baseline, has been proposed as another possibility to measure the transport parameter $\hat{q}$.

Another variable that was studied was the transverse momentum relative to the jet axis, j_T, given to a particle during the fragmentation of its parent after scattering. Broadening of the distribution of jet-particle momenta perpendicular to the jet axis were observed for the two energy loss models. Since this additional is directly related to the color density of the traversed medium [58, 59, 60].

Additionally, the p_T distributions of particles at different distances r inside the jet were studied. In vacuum angular ordering rules the p_T distribution of particles at different distances r to the jet axis. High-p_T particles are predominantly produced close the jet axis whereas low-p_T particles are found at larger distances. High-p_T particles

at large distances from the jet axis are due to hard gluons radiated shortly after the initial hard scattering. These gluons see the same medium as the leading parton, but having smaller energies the effect of energy loss should be stronger. In the the ratio of particles yield (R_{AA}) (Q-PYTHIA/PYTHIA and PYQUEN/PYTHIA vs p_T for three r cone sizes clear differences between the two Monte-Carlo in the pattern of increase of low-momentum particles and depletion of high-momentum particles at different r can be observed.

Another way to study modifications in jets structure, due to parton energy loss is through the event shape variables.

At $\sqrt{s_{\mathrm{NN}}} = 200\ \mathrm{GeV}/c$ we confronted with the double hump structure obtained in section 6.3.2. To see what are the predictions of the generator Q-PYTHIA , that takes into account the effects of parton energy loss in the medium. The interest of the results lays in the behavior of the dependence of the yields in two different parts of the τ vs R distribution. While for low values of R and τ we observe a decrease of the probability with increasing $\hat{q}$, in the case of high values of τ we observe a frank increase of the yield in the away-side correlation with the double hump. These results remind us very much of the double hump structures encountered in the RHIC experiments in collisions of heavy ions.

It seems that the studies of the topologies of events may offer a detailed insight in the mechanism of hadronisation after collisions.

Due to interaction with the dense medium, there are more particles produced in the low-p_T region with PYQUEN and Q-PYTHIA respect to PYTHIA. This increment produces events with a uniform distribution. This is shown in the top and middle panels of figure 9.3. For $\tau_{pp} \gtrsim 0.8$ PYQUEN and Q-PYTHIA particle production is above PYTHIA production and for $\tau_{pp} \lesssim 0.8$, they are below PYTHIA production. This behavior also change recoil and T_{min} distribution at low-p_T. At high-p_T there are no difference between $p+p$ and $Pb+Pb$.

We conclude that jets studies on $p+p$ and $Pb+Pb$ collisions and their structure can help us to understand the particles energy loss due to a presence of a dense medium. Either with a complete jet reconstruction or with ESA, it is possible to define appropriate variables that showing changes due to parton energy loss and consequently the jet structure. As mentioned above, the Monte-Carlo used in this work are not the only ones, but taking into account their advantages and limitations we consider them as good tools for the parton energy loss simulation, but only comparisons with the real data will determine if the models work correctly and understand a little more the way the energy loss mechanisms occur.

Bibliography

[1] F. Carminati *et al.* [ALICE Collaboration], J. Phys. G **30**, 1517 (2004).

[2] B. Alessandro *et al.* [ALICE Collaboration], J. Phys. G **32**, 1295 (2006).

[3] J.D. Bjorken, FERMILAB-PUB-82/59-THY (1982).

[4] M. Gyulassy and X. n. Wang, Nucl. Phys. B **420**, 583 (1994)

[5] R. Baier et al., Phys. Lett. B 345 (1995) 277;

[6] M. Gyulassy, P. Levai, and I. Vitev, Nucl. Phys. B571 (2000) 197

[7] U.A. Wiedemann, Nucl. Phys. B588 (2000) 303;

[8] J. Adams *et al.* [STAR Collaboration], Phys. Rev. Lett. **91**, 072304 (2003)

[9] T. Sjostrand, S. Mrenna and P. Skands, JHEP **0605** (2006) 026

[10] X. N. Wang and M. Gyulassy, Phys. Rev. D **44**, 3501 (1991).

[11] I. P. Lokhtin and A. M. Snigirev, Eur. Phys. J. C **45**, 211 (2006)

[12] N. Armesto, L. Cunqueiro and C. A. Salgado, Eur. Phys. J. C **63**, 679 (2009)

[13] `http://aliceinfo.cern.ch/Offline/AliRoot/Manual.html`

[14] Antonio Ortiz Velasquez, Guy Paic ALICE-INT-2009-015

[15] Antonio Ortiz Velasquez, Guy Paic ALICE-INT-2010

[16] S. L. Blyth *et al.*, J. Phys. G **34**, 271 (2007)

[17] H. Fritzsch, M. Gell-Mann and H. Leutwyler, Phys. Lett. B **47**, 365 (1973).

[18] J. C. Collins and M. J. Perry, Phys. Rev. Lett. **34**, 1353 (1975).

[19] K. G. Wilson, Phys. Rev. D **10**, 2445 (1974).

[20] F. Karsch, Nucl. Phys. A **698**, 199 (2002)

[21] H. Satz, Rept. Prog. Phys. **63**, 1511 (2000)

[22] J. D. Bjorken, Phys. Rev. D **27**, 140 (1983).

[23] J. Letessier, J. Rafelski. Hadrons and Quark-Gluon Plasma. Cambridge University Press, 2002:

[24] U. W. Heinz and M. Jacob, arXiv:nucl-th/0002042.

[25] `http://www.bnl.gov/RHIC/`

[26] CERN Courier: Early days: Aachen: the case for LHC. October 2008

[27] I. Arsene *et al.* [BRAHMS Collaboration], Phys. Rev. Lett. **91**, 072305 (2003)

[28] S. S. Adler *et al.* [PHENIX Collaboration], Phys. Rev. Lett. **91**, 072303 (2003) [arXiv:nucl-ex/0306021].

[29] B. B. Back *et al.* [PHOBOS Collaboration], Phys. Rev. Lett. **91**, 072302 (2003)

[30] C. Adler *et al.* [STAR Collaboration], Phys. Rev. Lett. **90**, 082302 (2003)

[31] J. Adams *et al.* [STAR Collaboration], Phys. Rev. Lett. **93**, 252301 (2004)

[32] D. Kharzeev, Y. V. Kovchegov and K. Tuchin, Phys. Rev. D **68**, 094013 (2003)

[33] X. N. I. Wang, Phys. Rept. **280**, 287 (1997)

[34] M. Lev and B. Petersson, Z. Phys. C **21**, 155 (1983).

[35] T. Ochiai, S. Date and H. Sumiyoshi, Prog. Theor. Phys. **75**, 288 (1986).

[36] F. Antinori [ALICE Collaboration], Nucl. Phys. Proc. Suppl. **177-178**, 156 (2008).

[37] D. d'Enterria [CMS Collaboration], J. Phys. G **35**, 104039 (2008)

[38] N. Grau [ATLAS Collaboration], J. Phys. G **35**, 104040 (2008)

[39] K. Aamodt *et al.* [ALICE Collaboration], Eur. Phys. J. C **65**, 111 (2010)

[40] K. Aamodt *et al.* [ALICE Collaboration], Eur. Phys. J. C **68**, 89 (2010)

[41] K. Aamodt *et al.* [ALICE Collaboration], Eur. Phys. J. C **68**, 345 (2010)

[42] `http://wwwasd.web.cern.ch/wwwasd/geant/`

[43] http://root.cern.ch/drupal/content/documentation

[44] http://www.phys.ufl.edu/~rfield/cdf/tunes/py_tuneA.html

[45] R. Baier, Y. L. Dokshitzer, A. H. Mueller and D. Schiff, Phys. Rev. C **60**, 064902 (1999)

[46] R. Baier, Y. L. Dokshitzer, A. H. Mueller and D. Schiff, Phys. Rev. C **64**, 057902 (2001)

[47] I. P. Lokhtin and A. M. Snigirev, Phys. Lett. B **440**, 163 (1998)

[48] I. P. Lokhtin and A. M. Snigirev, Eur. Phys. J. C **16**, 527 (2000)

[49] N. Armesto, L. Cunqueiro and C. A. Salgado, Eur. Phys. J. C **61**, 775 (2009)

[50] G. Altarelli and G. Parisi, Nucl. Phys. B **126**, 298 (1977).

[51] A. Dainese, C. Loizides and G. Paic, Eur. Phys. J. C **38**, 461 (2005)

[52] S. D. Ellis and D. E. Soper, Phys. Rev. D **48**, 3160 (1993)

[53] G. C. Blazey *et al.*, FERMILAB-CONF-00-092-E, May 2000. 32pp

[54] G. Arnison *et al.* [UA1 Collaboration], Phys. Lett. B **132**, 214 (1983).

[55] C. A. Loizides, arXiv:nucl-ex/0501017.

[56] G. Hanson *et al.*, Phys. Rev. Lett. **35**, 1609 (1975).

[57] A. Ayala, E. Cuautle, I. Dominguez, A. Ortiz and G. Paic, Eur. Phys. J. C DOI 10.1140/epjc/s10052-009-1058-3 1

[58] R. P. Feynman, R. D. Field and G. C. Fox, Nucl. Phys. B **128**, 1 (1977).

[59] A. L. S. Angelis *et al.* [CERN-Columbia-Oxford-Rockefeller Collaboration], Phys. Lett. B **97**, 163 (1980).

[60] S. S. Adler *et al.* [PHENIX Collaboration], Phys. Rev. D **74**, 072002 (2006)

[61] J. Casalderrey-Solana and X. N. Wang, Phys. Rev. C **77**, 024902 (2008)